UNIVERSITY OF KWAZULU-NATAL

MASTERS DISSERTATION

Rain Attenuation Modeling and Prediction for Optical Wireless Communication Systems in Durban, South Africa

Author:

Sabelo Qiniso Buthelezi

Supervisors:

Prof. Thomas J. O. Afullo

Dr. Modisa Mosalaosi

This dissertation submitted in fulfillment of the requirements

for the degree of Masters of Science (MSc): Electronic Engineering

School of Engineering

College of Agriculture, Engineering and Science

Durban, South Africa

November 2021

UNIVERSITY OF KWAZULU-NATAL

Rain Attenuation Modeling and Prediction for Optical Wireless Communication Systems in Durban, South Africa

Author:

Sabelo Qiniso Buthelezi

Supervisors:

Prof. Thomas J. O. Afullo

Dr. Modisa Mosalaosi

School of Engineering

College of Agriculture, Engineering and Science

Durban, South Africa

November 2021

PREFACE

The research contained in this thesis was completed by the candidate ***Mr. Sabelo Qiniso Buthelezi***, under the supervision of ***Prof. Thomas J. O. Afullo*** and co-supervision of ***Dr. Modisa Mosalaosi*** in the Discipline of Electrical, Electronic, and Computer Engineering, School of Engineering, College of Agriculture, Engineering, and Science, University of KwaZulu-Natal (UKZN), Howard College Campus, Durban, South Africa. This thesis has not been submitted in any form to another university, and the results reported are due to investigations by the candidate. The entire contents of this work, except where the work of other researchers is acknowledged in the text, is the original work of the candidate.

As the candidate's supervisors, we have approved this thesis for submission.

Prof. Thomas J. O. Afullo

Signed

Date 3rd December 2021

Dr. Modisa Mosalaosi

Signed ________________

Date _________________

DEDICATIONS

I sincerely dedicate this thesis to the following people;

My family and friends. A special gratitude to my late grandmother, ***Mrs. Manono A. Buthelezi***, ***MaKhumal****o* who always pushed me to my best; my dearest aunt ***Mrs. Phindile Thobeka Ngubane***, ***MaButhelezi***, and her husband ***Mr. Zipho Ngubane***. I also dedicate this to my late father, ***Mr. Amon Bongani Buthelezi***; my uncle ***Mr. Nkosinathi L. Buthelezi***; my teacher ***Mr. K. Nkomo***; to all my brothers, my family; my adorable son, ***Thandolwethu Zelwande Buthelezi***. And lastly, I dedicate this work to Telkom Centre of Excellence for sponsoring my studies.

DECLARATION 1: PLAGIARISM

I, ***Sabelo Qiniso Buthelezi*** hereby declare:

i. That this thesis is the first work of the writer and where work of other writers has been used, is accordingly recognized in the content.

ii. The thesis has not been submitted in any form to any other Institute of Higher Learning.

iii. This thesis does not include other persons' data, pictures, graphs or other information unless specifically recognized as being sourced from other persons.

iv. Where other written sources have been quoted, then:

   a) Their words have been re-written but the general information attributed to them has been referenced;
   b) Where their exact words have been used, their writing has been placed inside quotation marks and referenced.

v. This thesis does not include text, graphics or tables copied and pasted from the Internet, unless specifically acknowledged, and the source being detailed in the thesis and in the References sections.

***Sabelo Qiniso Buthelezi* ______________**

DECLARATION 2: PUBLICATION

The following research paper has been **ACCEPTED** and **PRESENTED** for publication, and parts of its materials are included in the thesis:

Sabelo Qiniso Buthelezi, Thomas J. O. Afullo, and Modisa Mosalaosi "Preliminary Attenuation Measurement and Prediction for an Optical Wireless Communication Link in South Africa", *The Southern Africa Telecommunication Networks and Applications Conference (SATNAC)*, 21-23 November 2021, Champagne Sports Resort, Drakensberg, South Africa.

ACKNOWLEDGEMENTS

I wish to express my sincere gratitude to my supervisors, ***Professor T.J.O. Afullo*** and ***Dr. Modisa Mosalaosi***; my colleagues ***Mr. Mohamed K. Elmezughi*** and ***Mr. Olabamidele O. Kolawole***, as well as ***Dr. Sumbiri Djuma***; for their invaluable support, encouragement, and guidance all through the course of this work. I really admire their efforts in proofreading this dissertation and for giving me the priceless opportunity to undertake my studies.

I sincerely thank my family for love, support and always having confidence in me; without their support I would be where I am. I am very much grateful to everyone who helped me, and supported me in any way during this course, more especially my aunt ***Mrs. Phindile Ngubane*** and her husband ***Mr. Zipho Ngubane***, for always being there for me whenever I needed them; to my brothers, and everyone who have contributed towards my studies, and made sure that my education has been a success.

I also wish to express my gratitude to all my friends, colleagues, academic mentors, the officials and other staff members of University of KwaZulu-Natal who rendered their help during the period of my studies. I recognize this opportunity as a big milestone in my career development. I will try to use gained skills and knowledge in the best possible way, and I will continue to work very hard to improve them, in order to achieve desired career goals.

ABSTRACT

The continuous demand for more reliable wireless communication systems with extremely high data rates has accelerated various aspects of research topics to be able to meet future needs. One of the most crucial topics in the field of communication is free-space optics (also known as optical wireless communication). It is well-known that the performance of any optical wireless communication system is strongly influenced by the atmospheric conditions in a given environment. In foggy, rainy, and clear weather conditions, optical signals are known to be attenuated due to scattering. The received signal is diminished in the presence of snow, rain, or even haze. Rain and clear weather conditions will be the focus of this research as there is hardly snow or haze in South Africa, especially Durban since it is a subtropical region.

In this research work, rain attenuation modelling and prediction will be done using an empirical method based on the relationship between the observed attenuation distribution and the related observed rain intensity distribution at a 30 second integration period. A disdrometer is used to obtain the rain intensity, and a power meter is used to log the received signal power level every 30 seconds to evaluate the influence of rain on the signal transmitted. The International Telecommunication Union (ITU-R) recommends targeting for 99.99 % system availability; as a result, the rainfall rate (R0.01) in the research region must be estimated for 0.01 percent of the time. The rain intensity and raindrop size distribution (DSD) modelling is then performed from the empirical method, obtaining R0.01 for Durban for all months throughout the experiment period. Using the disdrometer diameter ranges, the spherical droplet assumption is used to estimate the scattering parameters for frequencies between 2 GHz and 1000 GHz.

The relationship between the received signal level and the intensity of rain for a particular weather condition at a specific time is then obtained. Transceivers with a fixed length of 7 meters between them, due to shortage of material such as the fiber cables to link the transceivers to the computer for data monitoring and logging, and for accurate alignment, were used to conduct these experiments. This relationship is compared against the French model at a wavelength of 850 nm. The main results obtained from this work reveal that there are extremely high attenuation values compared to the French model, which thus calls for further investigation to provide the optimum model that can accurately predict these effects for reliable optical wireless communications in Durban, South Africa.

This work also determines the raindrop size (diameter) using the disdrometer. It is to be noted from the findings that the relationship between raindrop diameter and rain intensity is proven to be linear. Rain does have an effect on attenuating the received signal, however the results reveal that it does not have a significant effect. It can be observed from the measured attenuation that the attenuation was constant all over the link. As a result, it is reasonable to assume that the observed attenuation is less affected by rain intensity. This means that there's a high possibility of fog along with the rainfall. Indeed, according to this research, Durban has the lowest visibility of all the cities in South Africa, a factor that is closely linked to fogginess.

Table of Contents

List of Figures

List of Tables

CHAPTER 1

GENERAL INTRODUCTION

1.1 FSO Brief Description

Optical wireless communications (OWC), popularly known as free space optics (FSO), involves the transmission of data via free atmospheric channel using optical carriers within the infrared range of the electromagnetic spectrum [1]. Some of the advantages offered by OWC links over radio frequency (RF) systems include very high bandwidth, immunity to electromagnetic interference, easy installation and deployment, no license tariffs required, and low power consumption [2], [3]. Despite the advantages offered by OWC systems, their performances degrade during severe weather conditions. Aerosol scattering of optical signals and severe attenuation due to scintillation have been well reported in foggy weather and clear sky conditions respectively [1], [4].

During rainy weather, optical signals transmitted between OWC transceivers are not immune from scattering attenuation as the laser beam passes through big sized raindrops. Various DSD models have been developed to estimate the attenuation due to rainfall, but they are majorly proposed for radio wave links [5]. The few rain attenuation prediction models offered for OWC are largely location-dependent and are not entirely suitable for places with different rainfall patterns [3], [6]. This is clearly evident by the models recommended by the ITU-R for OWC which are solely based on France and Japan's rain attenuation measurements [5].

Dense fog is known to have the most unfavorable impact on optical waves as scattering attenuation of up to 300 dB/km is reported for visibilities less than 100 m [7]. However, in certain locations and at specific times where fog is absent, rainfall is usually one of the prevailing atmospheric conditions causing the deterioration of OWC link performance [7]. It is therefore pertinent to properly investigate the impact of rain on OWC links deployed for use in Durban, South Africa. This will significantly aid in developing models for predicting rainfall attenuation specifically for OWC systems based on the rainfall profile in such regions. It will also assist in link budget planning for designing OWC links to be deployed in such places.

1.2 Background of FSO

Various models [5], [7] have been developed to determine rain attenuation parameters for free space optical links in rainy weather. In South-East Asia, a model based on the power-law relationship of specific rain attenuation using heavy rainfall data collected over a one-year period was proposed. The estimated power law parameters of rain attenuation were evaluated using the method of least square mean equation (LSME) with the Levenberg-Marquardt optimization technique [5]. In [7], the proposed model simulates the interaction between FSO links and precipitation maps from which mathematical expressions were developed. The model considers the dependence of scattering attenuation of optical signals on DSD and accepts local rainfall statistics as its input for the location of interest.

This research will focus on the approaches used in [2], [4]-[7] to estimate specific rain attenuation parameters for OWC links deployed in major cities of South Africa. The results will be validated with real-time rain attenuation measurements from an OWC link and suitable models will be proposed.

1.3 Research Approach

The goal of this work is to determine rain attenuation parameters for optical signals, in Durban, South Africa. To accomplish this task, the following steps will be used;

1. Derive rain attenuation models for FSO, based on the measured relationship between specific attenuation and rain intensity. Establish the power law equations, then, compare the obtained results with other models that have been reported, like the ones for France and Japan, to check for any correlation.
2. Derive equations between specific attenuation and the rain intensity.
3. When there is rain, obtain the rain drop size based on the disdrometer readings, the amount of rain, and the attenuation recorded by the power meter.

1.4 Research Aims and Objectives

This work will meet following objectives:

1. Theoretically determine rain attenuation parameters for optical signals based on various rainfall measurements for the city of Durban, in South Africa.

2. Evaluate the analytical performance of the proposed model, which in this case is the power law model, under rainy conditions, alongside other established models.

3. Establish a suitable link budget analysis for OWC links to be deployed in Durban using the results and the equipment available, and then expand to various cities in South Africa, applying a similar approach to that for Durban.

1.5 Resources

This is a mathematical, simulation and experimental based study which requires computing resources and access to measurement equipment. These resources are:

- Optelix Nanowave FSO Link and Accessories.
- Vantage PRO2 Weather Station.
- MIB Browsers.
- RD-80 Vaisalla disdrometer.

All the above resources are available at the Centre for Radio and Rural Access Technologies (CRART) University of KwaZulu-Natal, Howard College Campus, under the leadership of Prof. Thomas J. O. Afullo.

1.6 Contribution of the Dissertation

- Development of R0.01 and distinct rainfall DSD models, for rainfall rates up to 120 mm/h, for the city of Durban. The proposed empirical models are based on the monthly and seasonal analysis of Durban'srainfall conditions. The analyses resulting from these proposed models reveal that most of the rain was drizzle, widespread, with some showers, but no thunderstorms.

- Power-law models for the extinction cross section in microwave and millimeter frequency ranges between 2 GHz and 1000 GHz at 20 degrees ambient temperature were developed in Durban. The relationship between attenuation and specific attenuation due to rain intensity was investigated using the empirical method, with all data collected at an optical wavelength of 850nm. The proposed models are a correlation of DSD with rain rate derived from disdrometers and a rain gauge used to estimate rainfall attenuation for different types of rainfall. The results of the predicted specific attenuation demonstrate that other atmospheric phenomena, such as fog, play a huge role in the monthly and seasonal variation of rainfall attenuation in Durban.

1.7 Methodological Approach

The RD-80 Vaisalla disdrometer and the Thorlab PM100D optical power meter as well as the FSO equipment were used to collect data for this study, for rain intensity and optical signal data respectively. The processing units are contained inside the microwave laboratory, which is located in Durban, South Africa. These equipment are installed on the roof top of the Electrical, Electronic, and Computer Engineering building, Howard College Campus of the University of KwaZulu-Natal. Since the previous study [8] used 1-minute data, this study will concentrate on rainfall data collected at 30-second sampling times during a six-month period between August 2019 and January 2020.

1.8 Organization of the Dissertation

In all, this work is divided into six chapters. The first chapter offers an overview of the study topic, which is organized as follows: Brief overview of the FSO, background of the FSO, research strategy, goals and objectives, resources, methodological approach, dissertation organization, and publications.

The second chapter is an in-depth literature study of OWC systems, which includes an overview, features, application areas, design, and eye safety requirements that are taken into account in OWC. It also provides a background on the topic, with a focus on the physics of rainfall microstructures. The major focus of the talks is on the physics of rainfall intensity. A brief overview of the atmospheric layers in the region of interest is also included.

The methodological technique used to get the results is explained in Chapter 3. To begin, it goes over each component of the FSO equipment, as well as the power meter and the disdrometer. It examines the power meter's overview. Its configurations, setups, hardware and installations, software, graphical user interface, and data logger. It also examines the configuration of the disdrometer measurements and the data logger. After that, the Fade Margin and FSO link losses are calculated. This chapter also discusses the process for extracting and analyzing the data.

The fourth chapter looks at the effects of rain, fog, and scintillation on the optical signal. The chapter is arranged as follows; the introduction, attenuation, which is the section where the attenuation is calculated. The time series plots are used to investigate the obtained results using the approach described in chapter 3, and to analyse the obtained data to see if there is any attenuation in the signal, and if so, what the causes are. The results are categorized as: clear days, drizzle or foggy days, and rainy days. Each day is also divided into different time periods. The relationship between rain intensity and raindrop diameter is also examined in this chapter, before the chapter is summarized in the last part.

The analysis and discussion of the acquired results are presented in Chapter 5. There is an introduction to the chapter and a section that explains how to get the findings. The specific attenuation is then determined in this chapter. The relationship between the attenuation and the specific attenuation due to rain is plotted and described after the specific attenuation is calculated. This chapter also includes a comparison with the existing model, with the attenuation and specific attenuation due to rain compared to the French Model to be specific.

The overall summary obtained from the research is the focus of Chapter 6, and conclusions are drawn from the results. In this chapter, future related works are also discussed.

CHAPTER 2

LITERATURE REVIEW

2.1 Introduction

This section provides a description of OWC technology, popularly known as FSO. The modelling of rain attenuation, and analysis of its impact on FSO link performance are reviewed from related works done in subtropical regions. The study area is Durban, in South Africa, which is a subtropical region, with an average rainfall of about 464 mm annually. The country gets most of its rainfall in summer, except for the Western Cape, which is the winter-rainfall region [9]. Given that, the study will be in Durban, and then can use the same approach in other major cities, with only Western Cape differing with the season the study is done. Applications of the OWC systems and important features are discussed. The section also gives a description and clarification of the blocks that make up the OWC system, modelling rain attenuation and a discussion on eye safety and standards. Towards the end of the section, troposphere's radio waves and microwaves communications are discussed, the chapter concludes with looking at the rainfall microstructure and mechanics, measurements for parameter modelling, a look at different models of rain intensity distribution, as well as rainfall attenuation estimation and prediction and its effects in South African areas.

2.2 Overview of OWC Technology

OWC entails the use of a laser to transmit data between two nodes through unguided media. Unguided media can be one or a combination of water, space, or atmosphere. Because this work is Free Space Optical based, the focus channel is the atmosphere. The data signal to be transmitted may be interrupted on any of the characteristic optical carrier wave properties which consist of its intensity, frequency, and phase. The OWC system may also be called the Line-Of-Sight (LOS) technology, which requires the transceivers to be directly aligned with each other without any sort of obstacles in between.

The traditional OWC system is designed for point-to-point interactions between two cognate transceivers placed at either end of the link. This communication system enables full duplex throughput with high data rate in which data sharing between the two transceivers can be accomplished simultaneously. The following sections discuss the analysis of existing associated work, the characteristics, applications, eye safety and standards, as well as the categorisation of the OWC system blocks.

2.3 Analysis of Existing Associated Work

In [6], Brazda *et al.* reported that FSO Links are becoming the usual means of modern wireless communication, but they suffer from attenuation caused by atmospheric particles. Consideration of this attenuation is important for FSO connection design. In addition, [6] notes that rain is not the most severe atmospheric phenomenon; as compared to fog, but it cannot be ignored as it is the most frequent form of precipitation in moderate climatic conditions. FSO rain attenuation is caused by energy absorption by rain drops and laser beam scattering in all directions. The standard raindrop lies between 0.1 mm to 7 mm in diameter. Spherical drops have a diameter of less than 2 mm while larger drops are flattened, with a diameter of less than 4 mm at the lower base. The real shape is approximated to determine the scattering properties of the electromagnetic wave [6].

The power law given in (1) represents the specific rain attenuation, which is the fundamental quantity in determining attenuation due to rain for terrestrial and earth space links.

$$\gamma_{rain} = k \times R^{\alpha} = A_{atmos} \tag{1}$$

where γ_{rain} is Rain specific attenuation; R is the Rain Intensity; A_{atmos} is atmospheric attenuation that occurs in link between FSO transceivers; $k\ and\ \alpha$ are rain coefficients, which depend on location and rain type.

The coefficients k and α depend on the carrier frequency of FSO systems, and on the characteristics of rain such as DSD and polarization [5], [10]. Both coefficient values can be obtained from ITU-R P.838-3 [11]. Since raindrops are assumed to have a spherical form, estimates of k and α do not depend on vertical or horizontal polarization [10].

The following formula was presented by Charbonneau, for French model [6], [12]:

$$\alpha_{rain} = 1.076 \times R^{0.67}\ [\frac{dB}{km}] \tag{2}$$

The following formula was presented for Japan model is much simpler and is obtained by using the assumption that attenuation is only dependent on rain intensity [6]:

$$\alpha_{rain} = 1.6 \times R^{0.63}\ \ [\frac{dB}{km}] \tag{3}$$

Charbonneau's model (France) is tested based on measurements obtained at a very low rain intensity of 5 mm / h, this is because the experiment was performed in Europe where they experience a very low rainfall rate relative to tropical regions such as South-East Asia [10]. Tropical areas receive enormous rainfall of up to 300 mm / h during rainy seasons. Increasing rain intensity results in an increase in FSO link attenuation. It has been shown in [6] that FSO link rain intensity is not based on wavelength, in optical spectrum. Under normal or common weather conditions, such as when it's raining or there is little fog, rain attenuation is not greater than 25dB / km [13] but during storms, which occurs occasionally, and most unlikely in South Africa, FSO attenuation may be very high.

The single beam FSO system in tropical rainy weather is particularly susceptible to atmospheric rain attenuation [13]. Research shows that due to this situation, in tropical regions, precise power law parameters of rain attenuation are required. FSO is a direct LOS transmission through the atmosphere for broadband communication [5]. The FSO system operates on a concept based on a narrow beam of laser light which transmits through the atmosphere the modulated digital signal from the transmitting station to the receiving station. Therefore, the transmitter and the receiver must be in a direct line of sight. Because of its high bandwidth, FSO device sends data at a very high rate. The system also requires no licensing, affordable rooftop installations, no arrangement of fiber cables, no need for security updates; these are the key advantages.

FSO is suitable for high-bandwidth applications such as high-definition video streaming for various clients, due to its ability to operate at a very high speed of up to 1.25 GB/s. Nevertheless, the FSO system suffers from the degradation of the signal, which is considered a significant setback. This has a huge impact on rain attenuation resulting in laser beam scattering, particularly when the beam passes through large raindrops. As described earlier, rain attenuation is highly dependent on the raindrop size distribution. Before [5], there has been no appropriate model for calculating the optical link rain attenuation in tropical region. The ITU-R on the FSO links, based on France measurements using the Charbonneau model and Japan measurements [10], recommended very few attenuation prediction models, most of which were proposed for the propagation of radio waves.

However, the parameters of the above models are suitable for low rain intensity's, and do not apply to tropical regions, which usually experience heavy rainfalls. Therefore, if you need to have accurate parameters for power law, you need a lot of detailed information about the FSO channel in tropical regions. To obtain rain intensity in these areas, rain intensity must be collected within 1-minute interval to model the rain attenuation based on ITU-R procedures. This is the approach that is based on the relation between the speed of rain in mm/h and the optical power that has been received. Rain attenuation modelling is conducted using two methods, known as the empirical method, which is based on the relationship between the observed attenuation distribution and the corresponding observed rain intensity distribution calculated at a certain integration time, in this study integration time is 30 seconds; and physical method, which attempt to reproduce the physical behavior involved in the attenuation processes. ITU-R created a well-known analytical expression, which they proposed by integrating their data with Laws and Parsons.

The Japan model [10] is evaluated based on measurements obtained from a maximum rain fall rate of up to 90 mm/h, which is considerably small compared to the average maximum rain fall rate of up to 4000 mm/h [14] in tropical areas. These models cannot be considered for cases of higher rain intensity such as tropical regions, but they can be used in sub-tropical regions, such as Durban, which is where this research will be based.

The least square mean equation (LSME) approach with Levenberg-Marquardt (LM) optimization can be used to estimate k and α values during heavy rainfall [5]. The power transmitted and the power received can be obtained when transmitting data through the FSO link and can also be used to measure the atmospheric attenuation given by (4) using the received power formula [5].

$$P_r = P_t - A_{geo} - A_{atmos} - A_{Clear} \tag{4}$$

where P_r is Received power (varying according to weather conditions); P_t is Transmitted power; A_{geo} is Geometric loss ([5] and [15] say that this is negligible at shorter distances of approx. up to 350m); A_{atmos} is Atmospheric attenuation due to rain fall; A_{Clear} is Clear weather loss.

Using curve fitting techniques and LM optimization, the estimated values of coefficients $k \text{ and } \alpha$ were evaluated by the LSME method to be 2.03 and 0.73 respectively. Hence, the France and Japan measurements are sufficient in determining the atmospheric attenuation in subtropical weather, like Durban, South Africa [16].

In [4], Basahel *et al.* reported that when calculating efficiency of FSO, availability is one of the major considerations. In tropical and subtropical climate, rainfall, is a major factor, influences the quality of the FSO link. The effect of haze on the availability of FSO should be considered, as it becomes important for longer distances of FSO connection. [4] Estimates the availability of FSO connections under the influence of rain and haze and the combination of the two; the availability estimation based on predicted attenuation due to rain and haze using projected long-term statistical measurements of rain (mm/h) and visibility (km).

Cumulative distribution function (CDF) was used to analyze the combined effect of both rain and haze. The telecommunications industry uses two types of availability, carrier class availability and enterprise class availability, which is commonly considered to be 99.999% and 99% respectively. Aside from the known phenomena affecting the FSO system such as heat, fog and snow; scintillation may also affect FSO performance. This problem can be solved by applying a spatial diversity technique or by using novel algorithm. The attenuation of optical energy due to scattering is because the size of the rain and haze particles is comparable to that of the wavelength of the transmitted signal. This reduces FSO link's availability for a given link distance.

In tropical climates, the reliability of FSO links is susceptible to two major weather events, rain and haze; with heavy rain being the main factor for tropical regions [2] and being used for long distances. The effect of haze is ignored in shorter distances, but the combination of the effect of rain and haze will limit the availability for distances that are a little longer for the business class [3].

Researchers in [17] investigated FSO performance using data calculated and recorded in the National Meteorological Center of Libya (LNMC). The modification of the Charbonneau empirical model is used to obtain the relationship between the maximum permissible length of the FSO link and the rainfall rate. In the analysis and simulation of the FSO link, given that Libya has a subtropical climate, there is hardly snow or fog, only the rain effect was considered. Scattering and scintillation are caused by the interaction of light and atmosphere due to the composition of the environment, which includes a variety of different types of molecular species and tiny suspended particles called aerosols under normal conditions.

2.4 Features of OWC

***High Modulation Bandwidth* –** Optical carrier waves have an extremely wide frequency bandwidth of up to 200THz. As there is a direct connection between the volume of data transmitted and the carrier's bandwidth, in OWC technology, high data rates of up to 20 percent of carrier frequency are feasible [18].

Unlicensed Spectrum – The optical wireless spectrum is free and requires no license. This provides a significant advantage over the overcrowded RF spectrum faced by legislative obstacles and rigorous policy procedures before a portion of the spectrum is used [18].

Cost Effective – Compared to their RF equivalent, the OWC system is simpler to install with comparable data transmission rate. OWC is an ideal alternative to delivering the same bandwidth by eliminating the excess trenching costs when laying optical fibres [18].

Weather Dependence The efficiency of OWC systems depends heavily on the state of the ambient atmospheric conditions present. Optical signals are known to undergo scattering attenuation in foggy weather and in clear weather conditions while vibration losses of optical signals arise from variations in the refractive index of the atmosphere [18].

Quick Installation and Deployment – The OWC system can be installed and operated in very few hours, with the appropriate installation tools available. The specific guidance to remember is there must be no interference between the transmitter and the receiver in the LOS [18].

2.5 Areas of Application

The above highlighted features of OWC makes it very attractive in many areas of application such as:

Last Mile Access – OWC technology fills the current bandwidth gap between the backbone of the optical fiber and the end users. OWC links are available on the market which transmit data rates of up to 10 Gbps with link lengths of up to a few kilometres [19], [20].

Backup to Fiber Optical Link – OWC systems may be deployed as a replacement to fill the void in cases where the optical fibre communication connection is interrupted or inaccessible [21], [22].

High-Definition Television (HDTV) – The OWC network can be used to distribute live High definition video signals to television stations in remote areas [19], [23].

Difficult Topography **-** Installing OWC network is cost-effective, rather than installing optic fiber cables in challenging terrain [24].

Temporal Links – The OWC system can act as temporary connections in emergency situations, this is because they are easy to install and use [25], [26].

2.6 Eye Safety and Standards

When developing an OWC system, great care must be taken to ensure that the optical radiation field is safe and does not present any risk to human health as well as animals that might deliberately or otherwise come into contact with it. The skin, and particularly the eyes, will suffer serious damage if the optical beams are directly focussed. The retina of the eye can focus on optical wavelengths of about 400-1400 nm, while the cornea portion of the eyes simply absorbs the energy of other wavelengths. Several international regulatory bodies, such as the Center for Devices and Radiological Health (CDRH), the International Electrotechnical Commission (IEC), the European Electrotechnical Standardization Committee (CENELEC), etc., offer safety recommendations on the use of optical beams, some of which are governed by regulation [27].

Class 1 lasers, according to the IEC standard laser classification [28], include low-power radiation emitting devices with wavelengths ranging from 0.3025-4 µm which causes no threat under all completely avoidable conditions of use. Class 1 M lasers are equivalent to class 1 lasers, but when observing optical radiation emitted from them with optical equipment such as microscopes, telescopes, binoculars etc., there is a chance of threat. Some classes of lasers include Class 2, Class 2 M and Class 3B [29], [30]. Since the classification of the laser is determined by the intensity of the beam, it should be remembered that no optical wavelength is permanently harmful or safe for the eyes. Hence, the OWCS can be designed to transmit wavelengths of any choice and still be relatively harmless to the eye [27].

2.7 OWC System

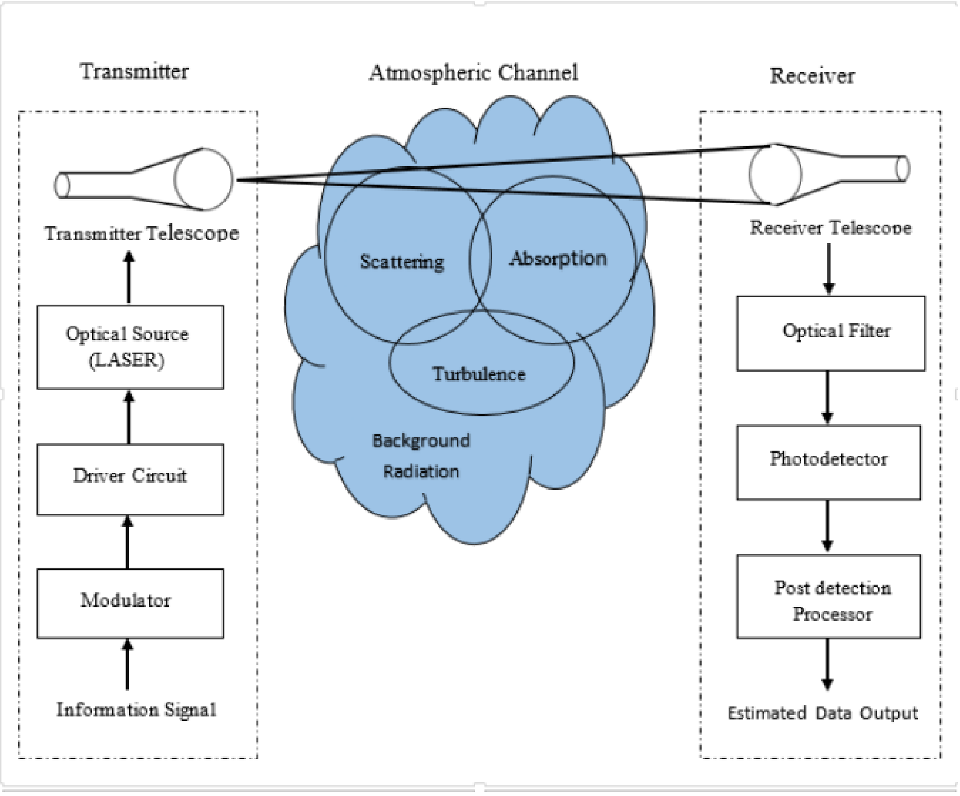

Figure 1: Block diagram of a terrestrial OWCS [27]

The OWC is composed of transmitter, atmospheric channel and receiver, each of which will be discussed below:

2.7.1 The Transmitter

In this section of OWC transmitter, the information signal is modulated onto the optical carrier wave and transmitted to the receiver through the atmospheric channel. Many OWC system typically employ the intensity modulation (IM). This requires the direct variation of the current moving the optical carrier wave in accordance with the signal of the information to be sent. It can also be accomplished by means of an external modulator such as the Mach-Zehnder interferometer. In addition to modulating the optical carrier wave by its intensity, other properties and characteristics such as the carrier wave 's frequency, phase, and state of polarization (SOP) can also be modulated with the information signal Optical sources widely used in OWC systems include laser emitting vertical cavity surfaces (850 nm), laser emitters Fabry-Perot (~1300 nm), dispersed feedback lasers (~1500 nm), LED (near Infrared) etc. These sources are reliable, very inexpensive, readily accessible, and can achieve data rates up to 40 Gbps. The Transmitter telescope collimates and transmits the modulated optical radiation at the opposite end of the channel towards the receiver [18], [27], [31].

2.7.2 The Atmospheric Channel

The atmosphere consists of gases such as nitrogen, oxygen, argon, carbon dioxide, water vapour, etc., and minute particles that are suspended in the air (aerosols). The environment also features rain, haze, fog and other environmental conditions. Such weather conditions are based on season and location. Aerosol concentrations are higher near the surface of the earth (troposphere) and decrease with increased altitude. These atmospheric components cause the optical signals which propagate through the atmosphere to be dispersed and absorbed, resulting in a reduction in the power levels of the signal reaching the receiver [32].

The temperature inhomogeneity of the atmosphere resulting from the turbulent mixture of dry, light air close to the earth’s surface and the colder air mass at higher altitudes during sunny and clear sky conditions causes extreme variations in the refractive index of the atmosphere [33]. This leads to the complete or partial variance of optical beams which traverse the changing refractive prisms of air packets or eddies. Thus, the optical data signal encounters random fading in its irradiance and phase. The effects of atmospheric turbulence on optical signals includes; beam steering, beam spreading, loss of spatial coherence, fluctuation of polarisation, etc. [34].

2.7.3 The Receiver

At the receiver, the transmitted information signal from the optical radiation incident is recovered. The incident optical beam incident is collected and focussed through the optical bandpass filter on the photodetector. The bigger the receiver telescope's aperture, the greater the range of incoming uncorrelated optical beams. However, it should be noted that, the larger the aperture, the more the background noise transmitted to the detector. The optical bandpass filter decreases background noise levels and sends data to the Photodetector. The Photodetector transforms the incoming optical signals into electrical signals. The photodetectors typically used in OWC receivers are the p-i-n diode (PIN) and the Avalanche Photodiode (APD). Examples of widely used photodetectors are Silicon PIN (300-1100 nm), Silicon APD (400-1000 nm), In GaAs APD (1000-1700 nm) etc. These photodetectors have gains UPTO 1 – 150 dB at data rates of up to 1.25 Gbps. In order to retrieve the information signal transmitted from the transmitter, the post-detection processor (also known as the decision circuit) amplifies, filters and processes the photodetector’s electrical signal output [27].

The two primary detection processes for receivers are the direct and coherent methods of detection. The intensity or strength of the incoming optical beam that impinges upon the photodiode is measured in the former [34]. At the other hand, the incident optical field is combined with the signal emitted from a local oscillator on the photodiode surface inside the coherent detection receiver. The benefits of the consistent detection process include simple amplification of the signal at a known intermediate frequency and improved signal-to - noise ratio in comparison with the direct detection system [35].

2.8 Atmosphere Layers

The troposphere is used in a terrestrial wireless communication system to transmit and receive electromagnetic (EM) signals from one location to another. The radio climatological properties of these places are the basic principle in propagating in this medium. The most essential zones for signal transmission in wireless communication, in general, are:

2.8.1 Satellite Orbits

There are regions that are useful for satellite and interplanetary communication beyond 500 kilometers. Currently, the ITU-R specifies four satellite orbits for C-band, Ku-band frequencies and above for satellite communication. The orbits are listed in this order [36]:

- Low Earth Orbit (LEO) situated between 500 and 2000 kilometers above the surface.
- Medium Earth Orbit (MEO) situated between 5,000 and 12,000 kilometers from the surface.
- Geostationary Earth Orbit (GEO) situated roughly about 36,000 kilometers from the surface.
- High Earth Orbit (HEO) is the orbital beyond GEO i.e. over 36,000 kilometers

2.8.2 Ionosphere

This is where the atmosphere's composites are mostly made up of ionized or charged particles called plasma. This region is a conductive layer that can be used to ‘bounce' back signals at low and moderate frequencies such as LHF, MHF, and HF in the 30 KHz to 30 MHz range. This area is vulnerable to cosmic radiation and astronomical events. It has a range of 500 kilometers above the earth's surface, just below the stratosphere [37]. In this area, the average plasma frequency is around 8 MHz [38].

2.8.3 Troposphere

This is the space region where high-frequency signal propagation is most common; it is also known as the free space region. Because of the low electron activity in the belt, some authors refer to it as the non-conducting zone. This region is used for propagation by broadband communication systems that utilise satellite and microwave links. It is 17 kilometers from the earth's equator and 9 kilometers from the earth's poles [37].

The troposphere will be the primary focus of this study. For its close closeness to the ground and the unrestricted influences of the natural environment on wave propagation in its domain, it is an area of significant radio-meteorological turbulence.

2.9 Radio Frequency and Microwave Communication in the Troposphere

The tropospheric layer of the atmosphere has traditionally been used to propagate signals for radio frequency (RF) and microwave communication systems. This layer is preferred above others due to its close closeness to the ground, which makes it appropriate for LOS propagation, especially at high frequencies. The troposphere, on the other hand, is an area of radio meteorological turbulences involving independent natural factors such pressure (P), water vapour pressure (ρ), atmospheric refraction and temperature (T). These factors influence the speed and direction of electromagnetic waves as they move through the atmosphere. The radio refractivity (N), a crucial function linked to these three factors, is calculated as follows [37]:

$$N = \frac{77.6\,P}{T} + \frac{3.73\times 10^{5}\rho}{T^{2}} \qquad (5)$$

Typically, these variables contribute to the tropospheric region's prevalence of instability in one way or another. For example, an occurrence of low pressure that is uniformly distributed throughout an area may suggest the possibility of rain or even strong thunderstorms, both of which are detrimental to propagation. As a result, the fluctuation of these factors adds to the tropospheric layer's unpredictable behaviour.

A clean line-of-sight distance between the receiver and transmitter is required when using the troposphere for RF and microwave propagation, as shown in Figure 2. To minimize multipath fading, it is important to remember that obstructions between the transmitter and receiver do not diffract the propagation path when using the LOS concept (also known as signal ghosting). In order to design an unobstructed microwave link, the Fresnel principle must be used to calculate the minimal clearance [8], [37]. In theory, the LOS is determined by the Fresnel ellipsoidal zone, F_n, given by:

$$F_n = \sqrt{\frac{n\lambda D_1 D_2}{(D_{1+}D_2)}} \qquad (6)$$

where n is the number of ellipsoids needed, D1 and D2 are the distances between the transmitter and the obstacle for both the transmitter and the receiver, and λ is the wavelength of the transmission's centre frequency. A simplified version of the equation, which contains the frequency (MHz) and a velocity constant, C, is usually written as:

$$F_n = 1.73\sqrt{\frac{nCD_1D_2}{F_{MHz}(D_1 + D_2)}} \tag{7}$$

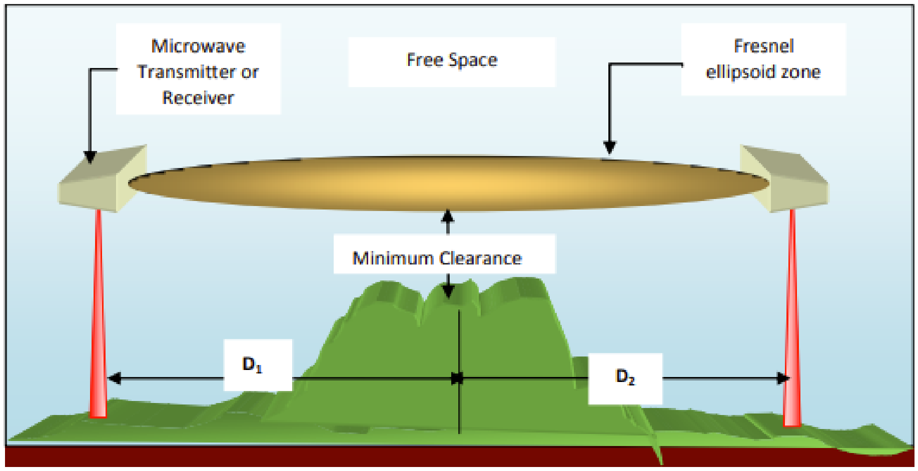

Figure 2: The Line-of-Sight (LoS) link between the receiver and transmitter [37]

The LOS distance for maximum clearance from the nearest barrier may be calculated using the Fresnel equation. Hills, buildings, and any other item that might block the LOS route are examples of obstacles. Most significantly, setting up a link necessitates taking into account the worst-case scenarios for signal losses, which is referred to as link budget. Multipath propagation, diffraction fading, rainy path attenuation, path losses, and antenna deficiencies such as polarization mismatch, pointing problems, and antenna inefficiencies can all lead to these situations. Optical line-of-sight and radio line-of-sight are the two most common kinds of line-of-sight. The furthest point in an optical LOS is generally the one that the eyes can see. Due to the curvature and sphericity of the globe, the radio LOS is believed to be longer than the optical LOS. A correction for earth sphericity is typically performed when calculating the radius of the earth:

$$R' = kR \tag{8}$$

where k = 1.33 represents the average adjustment due to earth curvature in temperate zones, and R = 6370 kilometers represents the radius of the earth. For temperate zones, for example, the modified earth radius for design purposes is always about 8300 kilometers. The frequency of transmission used for the design of RF and microwave links is ranged between 30 MHz to about 300 GHz. Appendix A-1 summarizes typical frequency bands useful for RF and microwave propagation.

2.10 Rainfall Microstructure and Mechanics

2.10.1 Rainfall Types

Based on the spatial distribution of rainfall, rainfall types may be divided into four main classes [39], [40]:

Convective Rain - These are more common in isolated regions with significant rain dispersion and strong wind currents. They have a short fall time (about tens of minutes) and smaller rain cells, and they are common in tropical areas.

Monsoon Rain - This is often a sequence of convective rain cells followed by stratified rainfall bursts. They can stretch hundreds of kilometers and have huge widths. They last longer than other forms of rain, such as convective rain.

Stratified Rain - This type of rainfall occurs at modest rain rates of up to 25 mm/h and has a broad rain cell throughout the length of the rain. It's also called stratiforms [39] because it is associated to the fusion of microscopic ice particles into larger ones during the build-up to rain.

Tropical Storm Rain - Hundreds of kilometers are covered by these strong rainfall patterns. A moderate monsoon or convective rainfall may occur in the areas surrounding the rainfall site.

2.10.2 Rainfall Cells

Rain cells are defined as mapped–out regions that are impacted by rainfall impacts during a single or many rain episodes. Rainfall is thought to be impacted by wind speeds and cloud drift, therefore a rain cell is typically dynamic. [41] A rain cell is defined as a specified region in which the rainfall intensity is considered to be greater than or equal to a threshold. In general, the forms of rainfall have a significant impact on the concept of rain cells. A convective rain cell, for example, is generally represented as a smaller rainfall cell diameter at greater rainfall rates, whereas a stratiform rain cell has a bigger rainfall cell diameter and lower rainfall rates [41]-[43]. Rainfall intensity is considered to be highest in the centre of a rain cell and gradually diminishes towards the borders of the depicted region. [44] The variance in rainfall intensities in the EXCELL model for rain cells is displayed in Figure 3. Therefore, a transmitted signal going across multiple overlapping rain cells will suffer substantially from the effects of rainfall attenuation. The circumstances of rainfall attenuation will thus be dependent on the climatic and geographic pattern of a location due to variations in rain-cell volume distribution.

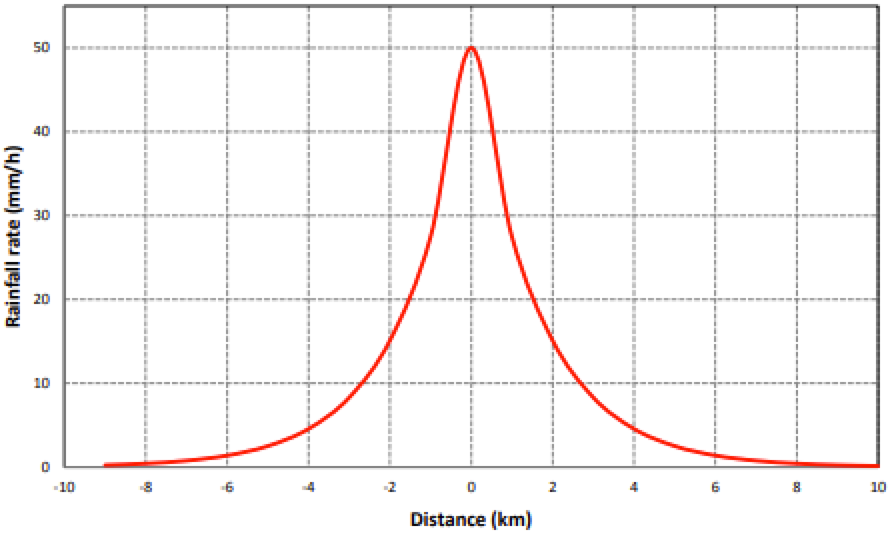

Figure 3: Variation of rainfall in a typical EXCELL rainfall cell [41]

2.10.3 Rainfall Intensity Physics

The diameter integral of the rainfall drop size distribution is used to calculate the rainfall rate, which is connected to the fall velocity and volumetric characteristic of the rain droplets. This is described mathematically in [45], [46]:

$$R(D) = \int_0^\infty v_t(D) N(D) V(D)\, dD \quad \left[\frac{mm}{h}\right] \tag{9}$$

where $v_t(D)$ is the terminal or fall velocity of the rainfall drops in m/s, $N(D)$ is the rainfall drop-size distribution in $m^{-3}mm^{-1}$and $V(D)$ is the volume of rain droplets in mm^{-3}. With a general spherical assumption for the raindrop shape, the volume of an assumed raindrop sphere for a diameter, D, in mm is given as:

$$V(D) = \frac{4\pi}{3}\left(\frac{D}{2}\right)^3 \tag{10}$$

Thus,

$$R(D) = \frac{\pi}{6}\int_0^\infty v_t(D) N(D) D^3\, dD \quad [m/s] \tag{11}$$

Equation (11) becomes a model explaining rainfall rate as a function of the third moment of the rainfall drop-size distribution after converting the rainfall rate unit from m/s to mm/h and balancing the surplus physical units. As a result, the new equation is:

$$R(D) = 6\pi \times 10^{-4} \int_0^\infty v_t(D)N(D)D^3\, dD \quad [mm/h] \tag{12}$$

where D_k is the mid-value of a diameter with an interval such that $\left(D_k - \frac{\Delta D_k}{2}\right) \leq D_k \leq \left(D_k + \frac{\Delta D_k}{2}\right)$. For B_n discrete classes, the rainfall rate equation in (12) may be approximated as follows:

$$R(D) \approx 6\pi \times 10^{-4} \sum_{k=1}^{B_n} v_t(D_k)N(D_k){D_k}^3\, \Delta D_k \quad [mm/h] \tag{13}$$

where all of the parameters have the same meaning as in equation (9).

2.11 Rainfall Measurement for Parameter Modelling

In the planning and construction of radio and microwave connections, rainfall modelling has remained a must. In a typical LOS route, the effect of rain on signal transmission is responsible for a substantial loss of transmitted energy. A compromise transmission power level is typically desired as part of link budgeting to compensate for the impacts of rain fading and rain attenuation [36]. Over-estimation of compensation can result in greater system complexity and expensive installation and maintenance costs; under-estimation, on the other hand, might result in poor overall system performance due to the possibility of rain fading [36].

Rainfall modelling primarily takes into account two microstructural characteristics of rainfall: rain intensity and rain drop size. Rainfall rate and rain drop size distribution are frequently measured as part of the modelling process, which necessitates accuracy and precision. Measurement is a crucial tool for capturing, comparing, verifying, and calibrating valuable data acquired from single devices or a network of sensors. These parameters can be measured using any of the instruments indicated by [39], [37]:

- ***Rain gauge***
- ***Radiometer***
- ***Radar***
- ***Disdrometer***

The radar has been described as the best of the three devices in terms of accurate attenuation estimate and profiling of rain microstructure along a propagation route. The radar works using reflected wave energy, but it's expensive to deploy and calibrate. [39]. For the simulation of slant path attenuation, the radiometer is employed.

The rain gauge, on the other hand, is the most popular and extensively used instrument in rain attenuation research, and it is being employed in huge numbers to create a rain gauge network for collecting rainfall data at many sites simultaneously [39]. The tipping bucket rain gauge and the capacitor rain gauge are the two most common types of rain gauges [37]. The tipping bucket rain gauge, on the other hand, has remained considerably more popular due to its precision and accuracy [47]. The integration time is a quantity obtained from the interval of tips of a tipping bucket rain gauge, which is the number of times the gauge empties water accumulation to begin another measurement. It's also known as the rainfall rate's time resolution. Rainfall rate information is more accurate and precise when the integration time is shorter. As a result, higher integration times must be converted to lower integration times, such as 60 minutes to 30 seconds.

The disdrometer is primarily used to precisely monitor rainfall droplets, intensity, and, in certain cases, shape profile along a propagation path. Impact disdrometers, video disdrometers, and optical disdrometers are the three main forms of disdrometers [39] [48]-[50]. The raindrop impact on the topmost cone of the impact disdrometer is measured using pressure-based transducers. The optical disdrometer makes advantage of the “make-and-break” activity of the laser spectrum by rainfall droplets, while the video disdrometer uses the motion detecting characteristics of video technology to ‘count' the number of rainfall drops [49], [50].

Independent distribution models must be constructed using rain intensity and rain-drop size data in order to compute suitable statistical findings from rain models. Over the duration, a lot of research has been done, notably on the works of [39] [51]-[56] have produced commendable outcomes in a variety of parts of the world. The ITU-R recommendations [15], [57] have also aided in the designation of different regions of the world as fixed climatic zones, each with its own rainfall rates and impacts on raindrop size.

2.12 Rain Intensity Distribution Models

Rainfall intensity is a metric that is measured in millimeters per hour (mm/h) and is expressed as an intensity per time scale. The gathering of relevant data from rain gauges, or better yet, rain gauge networks, is required for rain intensity modelling for communication systems. Because rainfall within a limited location might fluctuate in a typical severe rainstorm situation, causing rain cells to develop, the rain gauge network technique is frequently used to solve numerous distribution points for moving rain cells. The rain gauge is used to determine the intensity of point rainfall, which is rain that falls along a propagation route profile.

It is sometimes essential to convert rainfall integration time received from a tipping bucket rain gauge to an appropriate integration time. Rain data integration times of 30-seconds and one-minute were recommended by [47] and [58] as appropriate conversion values from the usual 60-minute integration period. In addition, [56] recommended the use of a one-minute integration period in microwave link designs as the optimum for determining rainfall attenuation.

Several rain intensity models have evolved throughout the years, and they have shown to be effective in solving both localized and regional problems related to rainfall attenuation. Researchers are interested in investigating rainfall using a statistical application of the CDF and probability distribution function (PDF). The usage of CDFs and PDFs in rainfall rate modelling is based on the fact that they may be used to get values by interpolating or extrapolating at locations within the function. In addition, the CDF may be used to calculate the amount of time rainfall is surpassed for 0.01 percent of the time, also known as $R_{0.01}$. This number is utilized in the design of a microwave link's fade probability. [39].

For microwave and millimetre link design, several rain rate models [36], [39], [58], [59] are employed. The most common models are as follows:

- The ITU-R P.837 rainfall rate model.
- The Global Crane rainfall rate model.
- Moupfouma I and Moupfouma II rain rate models.
- Gamma rainfall rate model.
- Lognormal rainfall rate model.

2.12.1 The ITU-R P.837 Rain Intensity Model

The ITU-R model divides the global rainfall distribution into 15 zones: A, B, C, D, E, F, G, H, J, K, L, M, N, P, and Q. ITU-R Recommendation P. 837-1 to P. 837-4 [59] provides the basis for the ITU-R model.

The projected rainfall rates provided by ITU-R for different zones are shown in Table 1 and Figure 4. In order to calculate rainfall attenuation levels, the model uses equations from ITU-R Recommendation P.838.

Table 1: ITU-R Model values for the 15 different rain zones around the World [59]

Percentage of Time	A	B	C	D	E	F	G	H	J	K	L	M	N	P	Q
1	1	0.5	0.7	2.1	0.6	1.7	3	2	8	1.5	2	4	5	12	24
0.3	0.8	2	2.8	4.5	2.4	4.5	7	4	13	4.2	7	11	15	34	49
0.1	2	3	5	8	6	8	12	10	20	12	15	22	35	65	72
0.03	5	6	9	13	12	15	20	18	28	23	33	40	65	105	96
0.01	8	12	15	19	22	28	30	32	35	42	60	63	95	145	115
0.003	14	21	26	29	41	54	45	55	45	70	105	95	140	200	142
0.001	22	32	42	42	70	78	65	83	55	100	150	120	180	250	170

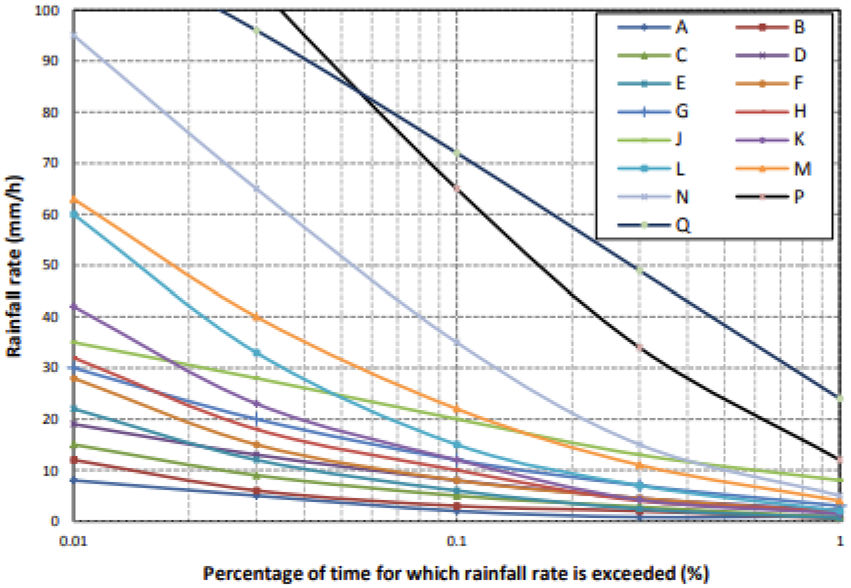

Figure 4: ITU-R rain-rate model for different parts of the world [59]

2.12.2 The Global Crane Rain Intensity Model

Rain fading from various regions of the planet is estimated using the global Crane rain rate model [37], [55]. Crane was able to come up with these Figures by gathering rainfall data from around the world and estimating the rain attenuation. The world's rainfall patterns are divided into 12 zones in this model: A, B, B1, B2, C, D1, D2, D3, E, F, G and H. As a result, the global Crane model is similar to the ITU-R model, with the exception that it uses 12 rainfall areas rather of the ITU-15. R's the zonal rainfall exceedances for various areas of the world are shown in Table 2 and Figure 5.

The Crane model also utilizes equations similar to ITU-R guideline [15] that are derived from [52] to compute the particular attenuation when computing the other parameters for rain intensity attenuation.

Table 2: The Global Crane Rain intensity Model [58]

Global Percent	A	B	B1	B2	C	D1	D2	D3	E	F	G	H
1	0.2	1.2	0.8	1.4	1.8	2.2	3	4.6	7	0.6	8.4	12.4
0.1	2.5	5.7	4.5	6.8	7.7	10.3	15.1	22.4	36.2	5.3	31.3	66.5
0.01	9.9	21.1	16.1	25.8	29.5	36.2	46.8	61.6	91.5	22.2	90.2	209.3
0.005	13.8	29.2	22.3	35.7	41.4	49.2	62.1	78.7	112	31.9	118	283.4
0.001	28.1	52.1	42.6	63.8	71.6	86.6	114.1	133.2	176	70.7	197	542.6

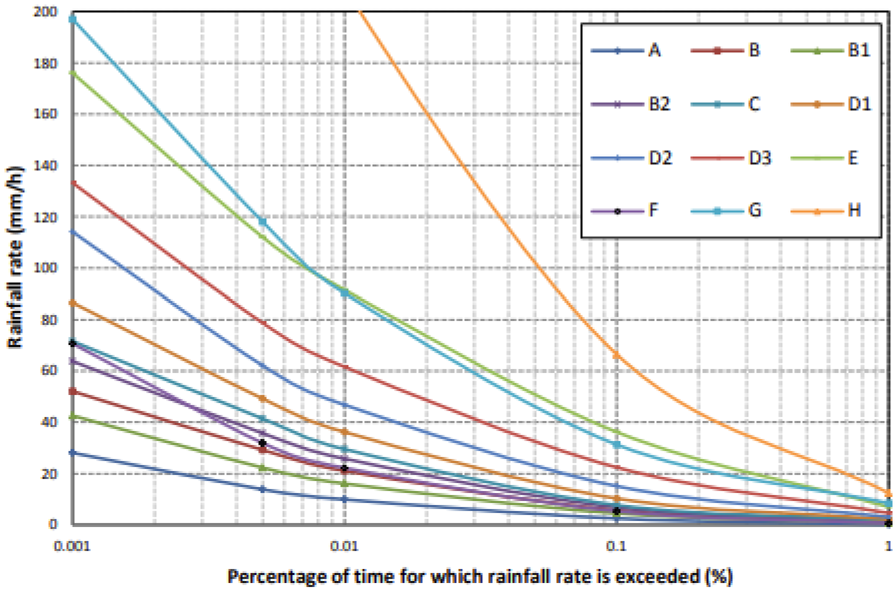

Figure 5: Global crane rain rate model for different parts of the world [58]

2.12.3 Moupfouma I and Moupfouma II rain rate Models

Based on Moupfoumas' radio tests in Congo, a tropical location [53], [60] created a rainfall rate model. The semi-empirical rainfall rate function is considered in the first rainfall rate model (or Moupfouma I):

$$P(R \geq r) = \; ar^{-b} \exp(-ur) \, , r \geq 2m\frac{m}{h} \tag{14}$$

where r is the rainfall rate in mm/h. The parameters a and b both $R_{0.01}$ dependent and are given as:

$$a = \; 10^{-4} {R_{0.01}}^{b} \exp(uR_{0.01}) \tag{15}$$

And,

$$b = \; 8.22{R_{0.01}}^{-0.584} \tag{16}$$

For most regions of the world, the slope of the function, u, is provided as 0.025, as recommended by Moupfouma. [61] created the modified Moupfouma model (or Moupfouma II) as an improved version based on the inadequacies of Moupfouma I [39], [53], [60]. Because of its reaction to low and high rain intensities, the model is suited for tropical climates [61]. When R 0.01 is known, rainfall CDFs may be utilized to forecast rainfall intensities, according to their research [39], [40]. This is expressed as:

$$P(R \geq r) = (\frac{R_{0.01}+1}{r+1})^{b_1} \cdot e^{[u_1 \, (R_{0.01}-r)]-\log_e(10^4)} \tag{17}$$

where r in mm/h represents the exceeded rain rate during time P and b_1 is governed by the shape of the rainfall rate and it is described as:

$$b_1 = (\frac{r-R_{0.01}}{r+1}) \cdot \ln(\frac{r+1}{R_{0.01}}) \tag{18}$$

The numbers for u_1 are the slope of the rain CDF, which varies according on the climate area. For tropical and temperate zones, several values of u_1 exist [39] and are presented as:

$$u_1 = \frac{\ln(10^4)}{R_{0.01}} \exp[-\lambda(\frac{r}{R_{0.01}})^{\alpha}] \tag{19}$$

where this function corresponds to geographical features of a tropical location with $\lambda = 1.066$ and $\alpha = 0.214$. For temperate zones, the function is given as:

$$u_1 = \frac{\ln(10^4)}{R_{0.01}} \times \frac{1}{(1+\eta\left(\frac{r}{R_{0.01}}\right)^{\beta})} \tag{20}$$

where η and β are 4.56 and 1.03 respectively.

2.12.4 Gamma Rainfall Rate Distribution Model

Researchers in [53] and [62] found the gamma probability function for rainfall rate as a suitable function for predicting high rainfall rates. The gamma probability function, as described in [63] and [64], was used in recent rainfall investigations by [46], [65]:

$$f(r) = \frac{r^{\alpha-1}\exp(-r/\beta)}{\beta^{\alpha}\Gamma(\alpha)} \qquad for\ \ 0 \le r \le +\infty, \alpha > 0, \beta > 0 \tag{21}$$

where α and β are the input parameters of 2.26 to be determined by point estimation technique [66].

At high rainfall rates, the gamma function exhibits a fast declining characteristic, which is comparable to the behaviour of probability functions for rainfall rate. As a result, it performs effectively in areas with a lot of rain.

2.12.5 Lognormal Rainfall Rate Distribution Model

As explained in [53] and [62], the lognormal probability function is a distribution used to estimate low precipitation rates. The lognormal function used in recent research [46], [65] is as follows:

$$f(r) = \frac{1}{r\sigma\sqrt{2\pi}}\exp[\frac{-[\ln(r)-\mu]^2}{2\sigma^2}] \quad 0 \le r < +\infty, \tag{22}$$

where μ and σ are the standard mean and standard deviation of the whole population of rainfall samples are and respectively.

At low rainfall rates, the lognormal function, like a usual probability function for rainfall rate, provides extremely excellent predictions. As a result, it is effective in areas when rainfall is minimal.

2.13 Rainfall Attenuation Estimation and Prediction

2.13.1 Specific Attenuation Prediction

As a result, the total attenuation, A_T, experienced by a forward traveling electromagnetic wave interacting in a wet medium is a function of an exponential factor as the distance, d, increases. [45], [67] offer this expression for the attenuated wave component:

$$A_T = e^{-\gamma d} \tag{23}$$

where γ is the propagation constant, and its unit is the inverse of the distance unit, d. The decibel factor is used to obtain an appropriate amplitudinal level for the wave component, resulting in (23) becoming:

$$\log_{10}(A_T) = 10\log_{10}\frac{1}{e^{-\gamma d}} \tag{24}$$

This expression is reduced to:

$$A_T = \gamma d \times 10 \log_{10} e \quad [dB] \tag{25}$$

where e is a Napierian type logarithm constant equal to 2.718281828. The derived attenuation, commonly known as the route attenuation, is calculated from (25):

$$A_P = 4.343\,\gamma d \quad [dB] \tag{26}$$

which can otherwise be written in dB/km as:

$$A_P = 4.343 \times 10^3 \gamma \quad [dB/km] \tag{27}$$

In [45] the propagation constant across an averaged route in a rainy medium is defined as $\gamma = N(D)Q_{ext}(D)$ and $Q_{ext}(D)$ is the extinction cross section of the rainfall droplets at the plane of arrival. γ is defined as for an unlimited number of rain drops of diameter D:

$$\gamma = \int_0^\infty N(D)Q_{ext}(D)\,dD \tag{28}$$

By substituting the function of γ in (27), another expression is derived and this is given by:

$$A_P = 4.343 \times 10^3 \int_0^\infty N(D)Q_{ext}(D)\,dD \quad [dB/km] \tag{29}$$

Equation (29) is the expression representing the specific attenuation due to rainfall droplets and $N(D)$ is the rain drop-size distribution.

2.13.2 Path Attenuation Prediction

In signal transmission, rain attenuation is a critical factor. It differs from area to region since it is strongly influenced by local rainfall patterns. Since then, researchers have developed two rain factors that may be used to calculate attenuation. The following is a definition of rainfall path attenuation:

$$A_P\,[dB] = F\,(rain\ intensity, rain\ DSD, frequency, temperature, distance) \tag{30}$$

As seen above, (30) is a heterogeneous quantity that depends on characteristics like particular attenuation, radio link channel length, volume density of rainfall drops, and the horizontal-vertical cross-section of the rainfall under consideration. Rain attenuation may be modelled in three ways: physically, theoretically, and experimentally [37], [47], [61]. The connection between particular attenuation, propagation or link path length, and reduction factor is defined via a simple modelling process. Rainfall route attenuation in relation to rainfall specific attenuation may be calculated mathematically using the ITU-R standard [57] as follows:

$$A_P\,(dB) = A_s \times r \times d \quad [dB] \tag{31}$$

where A_s denotes the specific attenuation in decibels per kilometer, r denotes the reduction factor, and d is the length of the link line in kilometers. [52] Also proposed that the rain-rate is connected to the specific attenuation (A_s) via a power-law connection:

$$A_s = kR^{\alpha}{}_{0.01} \qquad [dB/km] \tag{32}$$

For a particular model of the rain microstructure, k and α depend on the wave frequency and polarization. They are derived from the following equations:

$$k = [K_H + K_V + [K_H - K_V]\cos^2\theta\cos 2\tau]/2 \tag{33}$$

In ITU-R P.838 [15], K_H and K_V are the corresponding polarization values in horizontal and vertical polarization. Also, τ and θ are the link's tilt angle and elevation angle, respectively, and are linked to α as shown in 34:

$$\alpha = \frac{1}{2k}\{K_H\alpha_H + K_V\alpha_V + [K_H\alpha_H - K_V\alpha_V]\cos^2\theta\cos 2\tau\} \tag{34}$$

where τ is the polarization tilt angle relative to horizontal and θ is the path elevation angle. Circular polarization is usually believed to be 45 degrees. Appendix A-2 shows the various values of k and α in (32) for various frequencies and polarization schemes.

2.13.3 Path Reduction Factor and Rain Cell Effects

Signals traveling through rainfall encounter various degrees of rainfall intensity, according to the preceding discussion on rainfall cells in section 2.5.2. The configuration of the rain cells will determine the strength of the rainfall. The path reduction factor is used to estimate the actual length of the transmission path, d_0, as a result of this [58], [68], [69] Figure 6 illustrates this Authors have argued that rainy convective cells in the tropics may have a bigger cell diameter and so do not require path reduction; as a result, various route length reduction models have been developed [68], [69] .

Some of the route reduction factor models that have been presented are as follows:

- Path reduction model found in [53].
- The path reduction model proposed in [57].
- Path reduction model found in [70].
- The CETUC model proposed in [71].

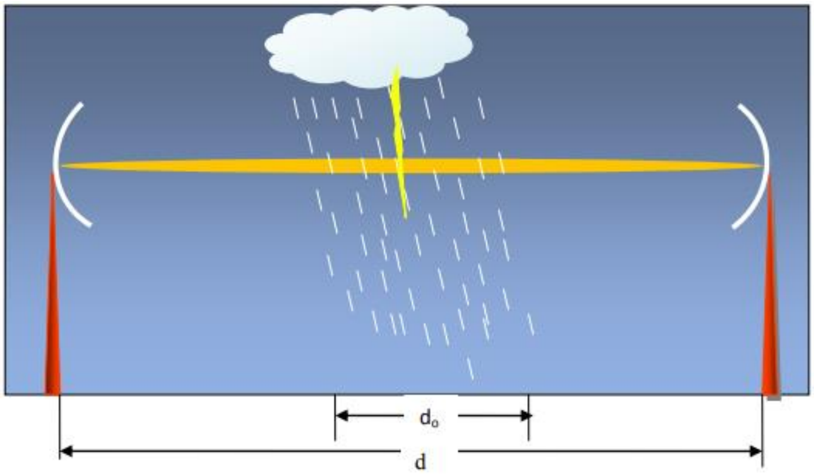

Figure 6: Actual link distance and actual rainfall distance [58]

To calculate the variance in transmission path length, these models use the rain cell theory and the rainfall growth concept.

2.14 Rainfall Effects in South African Areas

The southernmost point of the African continent is South Africa [72]. Namibia, Botswana, Zimbabwe, Swaziland, and Mozambique are its five neighbours. The nation is divided into five rainy zones based on the terminology of the ITU-R recommendation [59], E, F, K, L, and M. Figure 7 depicts a map of South Africa showing some of the country's major cities.

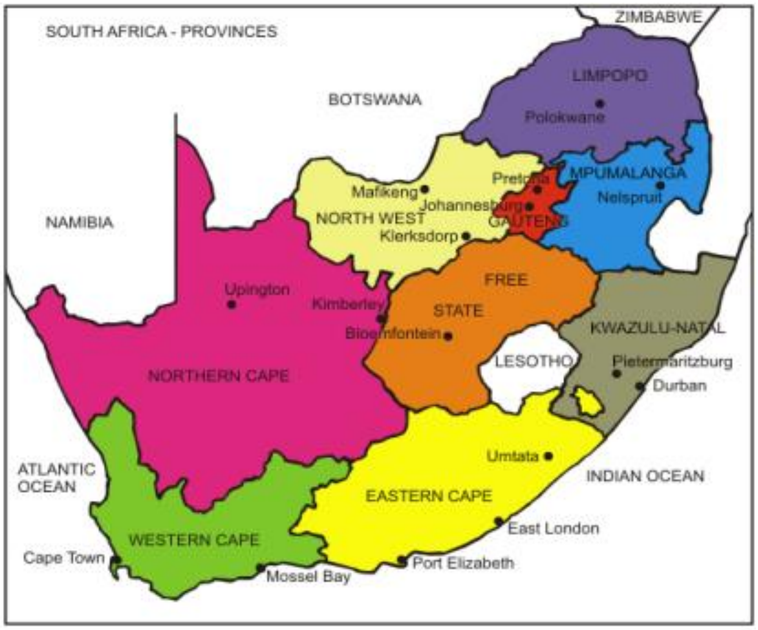

Figure 7: Map showing South Africa region and the surrounding countries [73]

South Africa offers a diverse range of climatic conditions; for example, coastal areas influenced by the Indian and Atlantic seas are primarily wet. The hinterland, on the other hand, is mostly dry throughout the summer and occasionally sees snowfall during the winter. Of addition, the climatic conditions in South Africa are highly influenced by seasonal cycles. According to [74], South Africa has four distinct seasons:

(i) Summer, which lasts from December to February.
(ii) Autumn, which lasts from March to May.
(iii) Winter, which lasts from June to August.
(iv) Spring, which lasts from September until November.

The fluctuation in rainfall and other hydrometeors throughout the year is primarily determined by these four seasons. The maximum rainfall incidence in South Africa, on the other hand, is generally concentrated during the spring and summer [74], [75].

2.15 Chapter Summary

This chapter contains a short overview of OWC as well as a survey of existing relevant work. OWCS features and application areas were also discussed. The transmitter, atmospheric channel, and receiver were all investigated as key components of the OWCS. In addition, the background research regarding the propagation of microwave and millimetric waves for terrestrial communication are the focus of this chapter. Rainfall has been recognized as the most important factor in hydrometeor-induced attenuation in microwave and millimetric communication systems. As a result, the focus of this chapter's discussions has been on the microstructure and mechanics of rainfall events in wave propagation. The use of various analytical, statistical, and empirical functions to characterize rainfall intensity was evaluated in a review of rainfall research. It is demonstrated that any of the models described may forecast rainfall attenuation, but with values particular to regional meteorological circumstances.

The rain attenuation for Durban was easily modelled and predicted thanks to background research on the power-law equation (1) and the Japan and Charbonneau's models. The work in section 2.10 provided more information and a better understanding of how to determine the intensity of rain and derive its equation. A closer analysis of various rain intensity models was conducted, which resulted in a better understanding of those models and made it simpler to select the most appropriate model for this study, as shown in the remainder of the report. Finally, the climatic region of South Africa, as well as its distinct rainfall features, were briefly examined. The materials used in accomplishing the required tasks are described in the next chapter. It also goes through the methodological steps involved in gathering and analyzing the data. In the next chapters, we'll look at the modelling process and the outcomes of rainfall measurements obtained in Durban.

CHAPTER 3

RESEARCH EQUIPMENT AND METHODOLOGY

3.1 Introduction

This chapter will discuss the measurement tools, measurement set-up and well as the data extraction methods, for both Optical Power Meter and the disdrometer. Different models used in this dissertation are presented in this chapter. They include models for the disdrometer and the FSO Link margin. In investigation for rain attenuation modelling for OWC links in the city of Durban, South Africa, the power law model is used. The FSO link losses and fade margins are also discussed/derived, and the process/steps followed in obtaining the results is discussed as the chapter concludes.

3.2 Equipment for Fiber Optic to Electrical and Electrical to Fiber Optics Converters

The measurement setup requires two computers, each displaying the data for each transceiver, as illustrated in Figure 8. The Gigabit Ethernet Media Converter, which is utilized as an electrical-to-fiber optic converter or a fiber optic-to-electrical converter, is shown in Figure 9. The Ethernet cable C85 with an RJ45 connector on the right (R) is used for sending or receiving electrical signals. The fiber cable with LC connection on the left (L) in Fig. 2 is responsible for receiving or sending fiber optic signals. Figure 10 the shows the powering box, that is used to power both transceivers that are shown in Figure 11, as well as the communication interface between the signal sent by the PC and the transceivers. The power box can be simply switched on and off when using the transceivers or not. It also important to remember to close the to avoid water getting inside and possibly damaging the equipment.

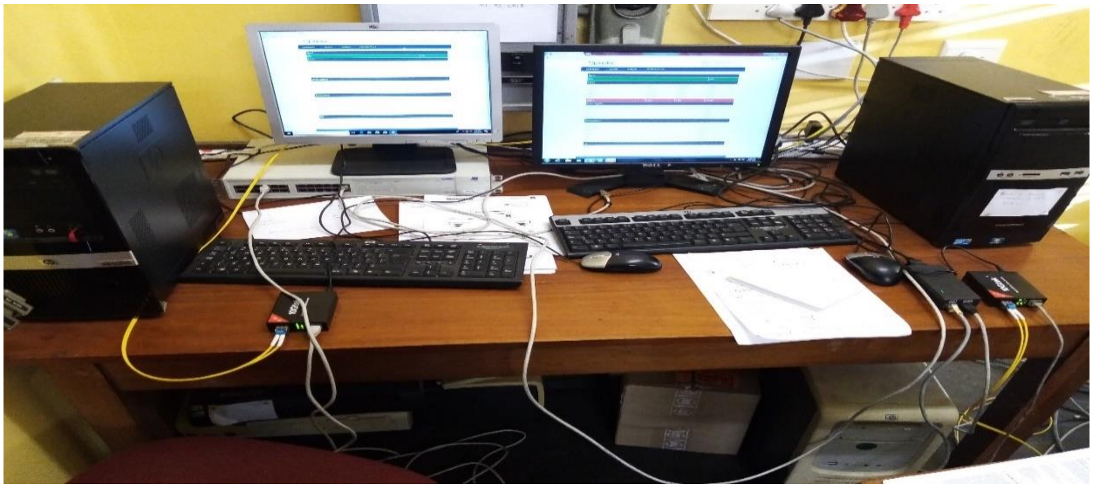

Figure 8: Current set up and equipment used for FSO link infrared signal level measurement Network

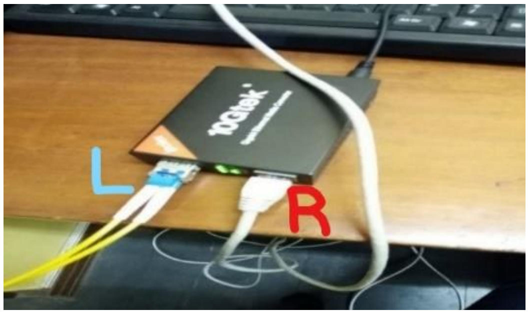

Figure 9: Electric to Fiber Optic Convert OR Fiber Optic to Electrical Converter

Figure 10: Transceiver Powering Box

Figure 11: Transceivers Used and the link distance of 7 meters between them

The two transceivers are 7 meters apart, as shown in Figure 11. The transceiver labelled T is used as the transmitter, while the one labelled R is used as the receiver. Signal transmission is carried out using infrared lasers, which are efficient and reliable. Lasers with an optical wavelength of 850nm are utilized for transmission. The transceiver uses the Avalanche Photodiode Detector (APD), which is a highly sensitive device, to detect the signal.

3.3 Overview of the Optical Power Meter

Basically, the optical power meter, is a graphical user interface (GUI) used to measure the power in an optical signal, or a device for testing average power in fiber optic systems. The basic operation of the OPM is to monitor and save the measurement of the power meter, whether it be power, current, irradiance, temperature, etc. The OPM also provides an analysis and data viewing interface and simple configuration of the measured data. The OPM also has a built-in software that provides continuous data logging. The OPM has a long-term measurement or short-term measurement option, with high resolution short-term measurements recorded by the software. However, it is possible to load the files saved by the OPM into the OPM Data Viewer, which can then be accessed and analysed. The OPM also offers different ways to interpret the collected data and also allows the user to switch between any parameters at any time [76].

3.3.2 OPM Data Logger

Table 3 shows the sample of the values that were logged on the 15th of December 2019. It shows how the values that are used to obtain the relationship between attenuation and the power received for specific time and also the rate of rainfall, are obtained. The most important value is the power (dBm), which is the power value recorded at a certain time, and it is used to get the attenuation for that time.

Table 3: Logged data values sample

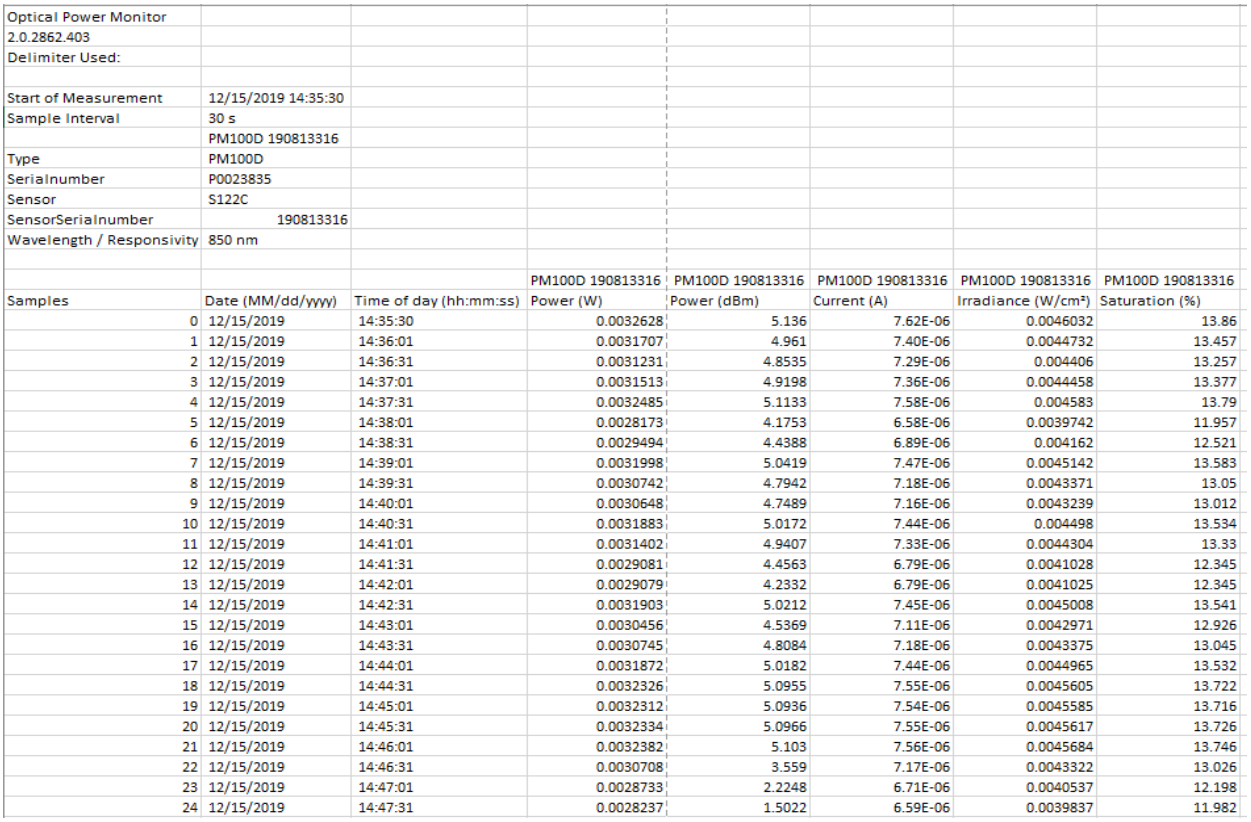

Optical Power Monitor							
2.0.2862.403							
Delimiter Used:							
Start of Measurement	12/15/2019 14:35:30						
Sample Interval	30 s						
	PM100D 190813316						
Type	PM100D						
Serialnumber	P0023835						
Sensor	S122C						
SensorSerialnumber	190813316						
Wavelength / Responsivity	850 nm						
			PM100D 190813316	PM100D 190813316	PM100D 190813316	PM100D 190813316	PM100D 190813316
Samples	Date (MM/dd/yyyy)	Time of day (hh:mm:ss)	Power (W)	Power (dBm)	Current (A)	Irradiance (W/cm²)	Saturation (%)
0	12/15/2019	14:35:30	0.0032628	5.136	7.62E-06	0.0046032	13.86
1	12/15/2019	14:36:01	0.0031707	4.961	7.40E-06	0.0044732	13.457
2	12/15/2019	14:36:31	0.0031231	4.8535	7.29E-06	0.004406	13.257
3	12/15/2019	14:37:01	0.0031513	4.9198	7.36E-06	0.0044458	13.377
4	12/15/2019	14:37:31	0.0032485	5.1133	7.58E-06	0.004583	13.79
5	12/15/2019	14:38:01	0.0028173	4.1753	6.58E-06	0.0039742	11.957
6	12/15/2019	14:38:31	0.0029494	4.4388	6.89E-06	0.004162	12.521
7	12/15/2019	14:39:01	0.0031998	5.0419	7.47E-06	0.0045142	13.583
8	12/15/2019	14:39:31	0.0030742	4.7942	7.18E-06	0.0043371	13.05
9	12/15/2019	14:40:01	0.0030648	4.7489	7.16E-06	0.0043239	13.012
10	12/15/2019	14:40:31	0.0031883	5.0172	7.44E-06	0.004498	13.534
11	12/15/2019	14:41:01	0.0031402	4.9407	7.33E-06	0.0044304	13.33
12	12/15/2019	14:41:31	0.0029081	4.4563	6.79E-06	0.0041028	12.345
13	12/15/2019	14:42:01	0.0029079	4.2332	6.79E-06	0.0041025	12.345
14	12/15/2019	14:42:31	0.0031903	5.0212	7.45E-06	0.0045008	13.541
15	12/15/2019	14:43:01	0.0030456	4.5369	7.11E-06	0.0042971	12.926
16	12/15/2019	14:43:31	0.0030745	4.8084	7.18E-06	0.0043375	13.045
17	12/15/2019	14:44:01	0.0031872	5.0182	7.44E-06	0.0044965	13.532
18	12/15/2019	14:44:31	0.0032326	5.0955	7.55E-06	0.0045605	13.722
19	12/15/2019	14:45:01	0.0032312	5.0936	7.54E-06	0.0045585	13.716
20	12/15/2019	14:45:31	0.0032334	5.0966	7.55E-06	0.0045617	13.726
21	12/15/2019	14:46:01	0.0032382	5.103	7.56E-06	0.0045684	13.746
22	12/15/2019	14:46:31	0.0030708	3.559	7.17E-06	0.0043322	13.026
23	12/15/2019	14:47:01	0.0028733	2.2248	6.71E-06	0.0040537	12.198
24	12/15/2019	14:47:31	0.0028237	1.5022	6.59E-06	0.0039837	11.982

3.4 Disdrometer Measurement Setup

To analyse the fluctuation of signals based on different weather conditions, such as clear weather, fog, and rain, weather data is commonly used. A disdrometer is a device that measures the size of raindrops as well as the rainfall intensity. The velocity and size of each particle in each drop are calculated and recorded. The disdrometer used is the Vaisalla RD-80 which captures drop size measurements using a personal computer. The disdrometer detects the size distribution of raindrops falling on the sensor's sensitive surface. Using this information, it is possible to calculate the actual drop size distribution in a volume of air [77].

The diameters of the raindrops that can be measured range between 0.3 and 5.4 millimetres. Drops smaller than 0.3 mm cannot be measured due to the measuring equipment's practical limits, and are normally of minimal relevance in the applications for which the device is designed. Due to the volatility of big drops, which promotes drop break-up, drops larger than 5.4 mm are extremely rare [77]. 127 drop diameter channels are distinguished by the RD-80. To limit the amount of data and get statistically relevant samples, the 127 drop size channels are re-grouped into 20 drop size groups that are spread more or less exponentially over the available spectrum of drop sizes. The translation into 20 classes is handled by the data logging software. As a result, every 30 seconds, the raindrop diameter and intensity are monitored, allowing them to be stored and presented on the PC screen as seen in table 3 [77].

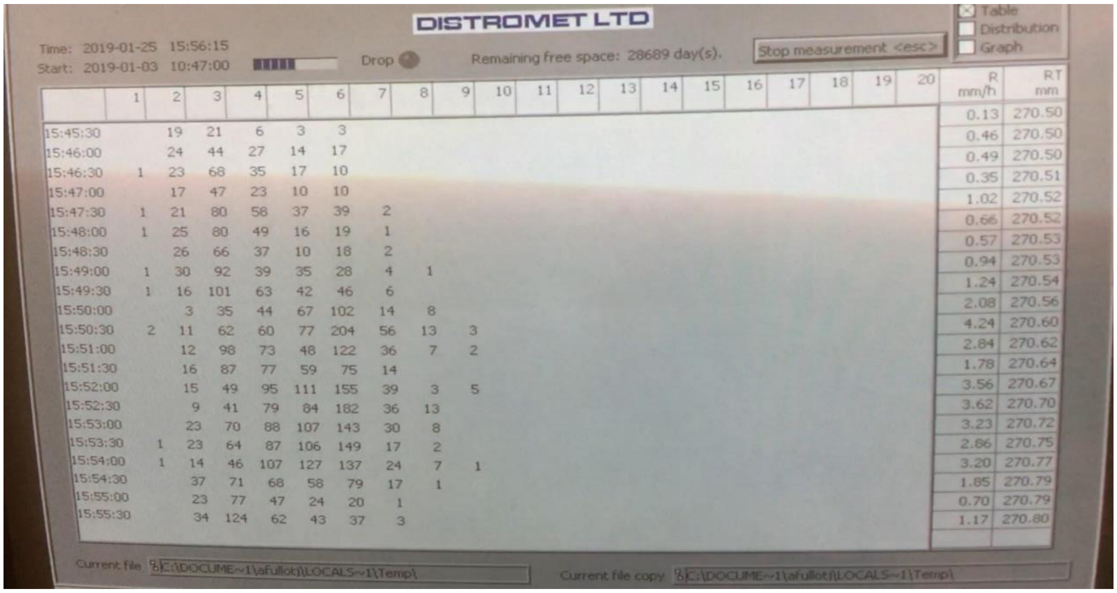

Time: 2019-01-25 15:56:15
Start: 2019-01-03 10:47:00
Remaining free space: 28689 day(s).
☒ Table
☐ Distribution
☐ Graph

	1	2	3	4	5	6	7	8	9	10	11	12	13	14	15	16	17	18	19	20	R mm/h	RT mm
15:45:30		19	21	6	3	3															0.13	270.50
15:46:00		24	44	27	14	17															0.46	270.50
15:46:30	1	23	68	35	17	10															0.49	270.50
15:47:00		17	47	23	10	10															0.35	270.51
15:47:30	1	21	80	58	37	39	2														1.02	270.52
15:48:00	1	25	80	49	16	19	1														0.66	270.52
15:48:30		26	66	37	10	18	2														0.57	270.53
15:49:00	1	30	92	39	35	28	4	1													0.94	270.53
15:49:30	1	16	101	63	42	46	6														1.24	270.54
15:50:00		3	35	44	67	102	14	8													2.08	270.56
15:50:30	2	11	62	60	77	204	56	13	3												4.24	270.60
15:51:00		12	98	73	48	122	36	7	2												2.84	270.62
15:51:30		16	87	77	59	75	14														1.78	270.64
15:52:00		15	49	95	111	155	39	3	5												3.56	270.67
15:52:30		9	41	79	84	182	36	13													3.62	270.70
15:53:00		23	70	88	107	143	30	8													3.23	270.72
15:53:30	1	23	64	87	106	149	17	2													2.86	270.75
15:54:00	1	14	46	107	127	137	24	7	1												3.20	270.77
15:54:30		37	71	68	58	79	17	1													1.85	270.79
15:55:00		23	77	47	24	20	1														0.70	270.79
15:55:30		34	124	62	43	37	3														1.17	270.80

Current file %C:\DOCUME~1\afullot(\LOCALS~1\Temp\
Current file copy %C:\DOCUME~1\afullot(\LOCALS~1\Temp\

Figure 12: Disdrometer Display

The first column in Figure 12 displays the sampling time intervals, which in this case vary by 30 seconds; the second column indicates the number of drops measured in each drop size class (class 1-20) during time interval t, which in this case is 30 seconds. The last two columns show R, which is the intensity at which the drops hit the Styrofoam (in mm/h), and the rainfall accumulated, RT (in mm), the real-time cumulative weight of the drops every 30 seconds.

The results in Fig. 30 are used to calculate the rain intensity by using the following formula [77]:

$$R = \frac{\pi}{6} \cdot \frac{3.6}{10^3} \cdot \frac{1}{F \cdot t} \cdot \sum_{i=1}^{20} \left(n_i \cdot {D_i}^3\right) \left[\frac{mm}{h}\right] \tag{35}$$

where F is size of the sensitive surface of the sensor, which is equal to 0.005 m^2; t is time interval for data logging; n_i is the number of drops measured in drop size class i during time interval t and D_i is the average diameter of drops in class i, see appendix A-2.

Equation (35) is used to calculate the rain intensity [77]. Figure 12 shows measured values in Tab-delimited ASCII format, which can be imported into other programs, like spreadsheet programs, for further analysis.

3.5 FSO Link Losses and Fade Margin

For the FSO link in question, the link parameters are shown in Table 4. For a line-of-sight link, the free space loss is given by:

$$FSL = 10\, log_{10}(\frac{4\pi d}{\lambda})^2 = 20\ log_{10}(\frac{4\pi d}{\lambda}) \tag{36}$$

Substituting d, the distance between the transceivers, which in this case is 7 m, and the free space wavelength of 850 nm, the FSL is determined to be:

$$FSL = 20\ log_{10}\left(\frac{4\pi(7)}{(850\times10^{-9})}\right) = 160.3\ dB \tag{37}$$

Now, the actual received signal level at the FSO receiver is determined from:

$$P_r = P_t + G_T + G_R - FSL - FL - OL - EL \tag{38}$$

where P_r is received signal level P_t is transmit signal level, both in dBm, G_T is transmit lens gain, G_R is receive lens gain, FL is the total feeder (system) loss, OL is optical loss, all in dB, EL is excess loss, which covers scintillation, atmospheric loss, and fog loss.

Table 4: PARAMETERS FOR FSO SYSTEM

Parameter	Value
Wavelength	850, 950, and 1550 nm
Transmit Power	16 dBm (40 mW)
Light Source	Laser
Receiver Sensitivity	-38 dBm
Transmit and Receiver Systems losses	2 dB
Receiver Aperture Diameter	16 cm
Eye Safety	Class 1M
Receiver Field of View	10 mrad
Detector	Avalanche Photodiode (APD)
Transmit Beam Divergence Angle	2.8 mrad
Data Rate	1.25Gbps

Thus, P_t is 16 dBm. And the lowest allowable value for P_r or P_{rmin} is -38 dBm.

$$G_T = 20\ \log_{10}\left(\frac{126.491}{\theta}\right) \tag{39}$$

where θ is the transmit beam divergence angle in radians, which is given as 2.8 mrad is this case, hence:

$$G_T = 20\ \log_{10}\left(\frac{126.491}{2.8\times10^{-3}}\right) = 93.1\ dB \tag{40}$$

For a lense of diameter D, which is 16 cm in this case, the gain of the receive lens is given by:

$$G_R = 20\ \log_{10}\left(\frac{31.623\pi D}{\lambda}\right) \tag{41}$$

Hence:

$$G_R = 20\ \log_{10}\left(\frac{31.623\pi(0.16)}{(850\times10^{-9})}\right) = 145.4\ dB \tag{42}$$

FL is given in Table 4 as 2 dB. The geometric or optical loss, OS, is caused by the optical beam diverging from its path. For this link with d=7 m, this loss is given by:

$$OL = 20\ \log_{10}\left(\frac{D}{d\theta}\right) = 20\ \log_{10}\left(\frac{0.16}{7(2.8\times10^{-3})}\right) = 18.2dB \tag{43}$$

Therefore, after substituting all the above calculated values, P_r is given by:

$$P_r(dBm) = 74.2\ (dBm) - EL\ (dB) \tag{44}$$

Note that EL can then be determined from link measurements.

3.6 Method

The power received in dBm, shown in table 3, will be subtracted from the maximum received power during a clear event, to get the attenuation. That attenuation will then be divided by the distance between the transceivers (in km) to get the specific attenuation. The disdrometer results, as shown in Figure 12, are then saved in a certain folder, after every 24 hours. These results will be accessed to get the rain intensity in mm/h, as well as the diameter of each raindrop in mm. Microsoft Excel will then be used to plot the relationships between specific attenuation vs. rain intensity, raindrop diameter vs. rain intensity, etc. as will be discussed in the following chapters.

3.7 Summary

In summary, this chapter presents, the measurement tools, set-up, OPM hardware, software and or GUI. This was broken down into different sections to give a clear definition of how the OPM is used, the data extraction methods and data loggers. The OPM data logger in table 3 shows the power (dB) that will be used to calculate the attenuation, as will be discussed in chapter 5. Figure 12 shows the disdrometer data logger with the rain intensity values. The equation for determining the Optical Link Margin is also presented. Finally, the procedure that will be used to perform the task, which is get the results and the relationships, is explained.

CHAPTER 4

RAIN INTENSITY AND RAIN DSD MODELING FOR DURBAN

4.1 Introduction

Rainfall is a significant fading factor for several radio propagation paths, particularly millimetric wave and microwave line-of-sight links. Raindrops absorb and scatter radio waves at microwave and millimetric frequencies, resulting in signal attenuation and a degradation in system availability and reliability [78]. In this chapter, the rain intensity and rain drop-size distribution modelling will be discussed. These two are one of the major parameters that are needed for the accurate rain attenuation. The drop size and rain intensity measurement were recorded using a RD-80 disdrometer in Durban. These measurements were done for the period of 6 months (August 2019 – January 2020). During rainy season, which in Durban is spring and summer that occurs between September and February, where most of the results were collected the rainfall intensity (R) is separated into four rainfall types. These types are based on the highest occurring rainfall intensity. The events are drizzle (0 mm/h < R < 5 mm/h); widespread (5 mm/h ≤ R < 10 mm/h); shower (10 mm/h ≤ R < 40 mm/h); and thunderstorm (R ≥ 40 mm/h). This section focuses on the rain intensity and drop-size distribution in Durban.

Rain drop-size measurements were collected with a Joss and Waldvogel disdrometer, RD-80, as mentioned before, and it can be seen in figure 13-14. The disdrometer has a sensor, which is located outdoor and is exposed to rain; it has a processor, around 10 meters long cable that connects the sensor and the processor, and the indoor computer unit. The RD-80 converts the mechanical momentum of falling drops into electrical pulses using the electromechanical sensor. The processor has a circuitry to eliminate the signal that is unwanted, mostly due to an acoustic noise and produces a 7-bit code at the output for every-drop hitting the sensitive surface of the sensor [77]. The disdrometer has $0.005m^2$ of sampling area with an accuracy of +/-5% and a 127 drop-size classes resolution. It collects raindrops sizes with a diameter ranging between 0.359 and 5.373 mm [77].

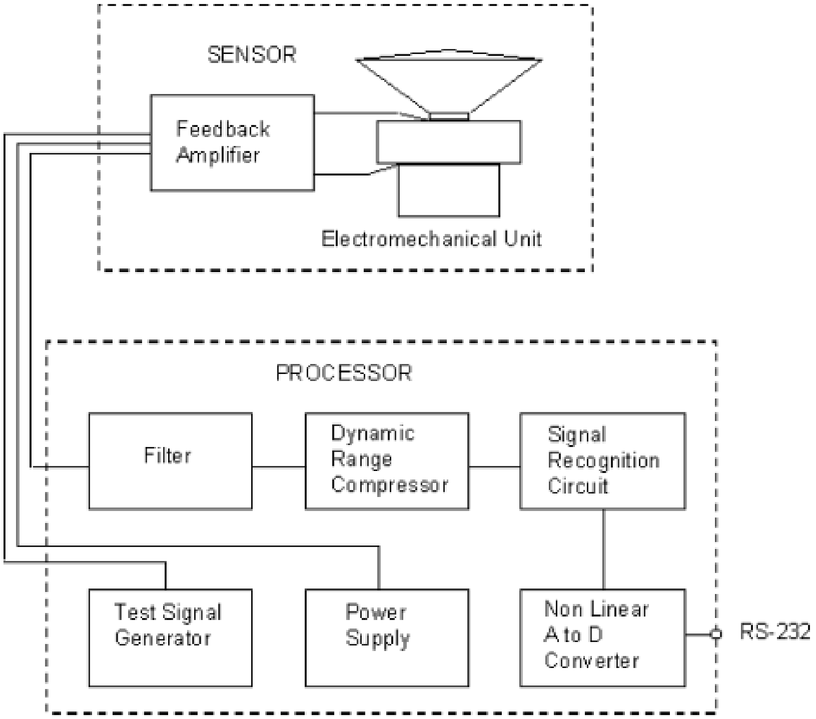

Figure 13: Disdrometer RD-80 block diagram [8]

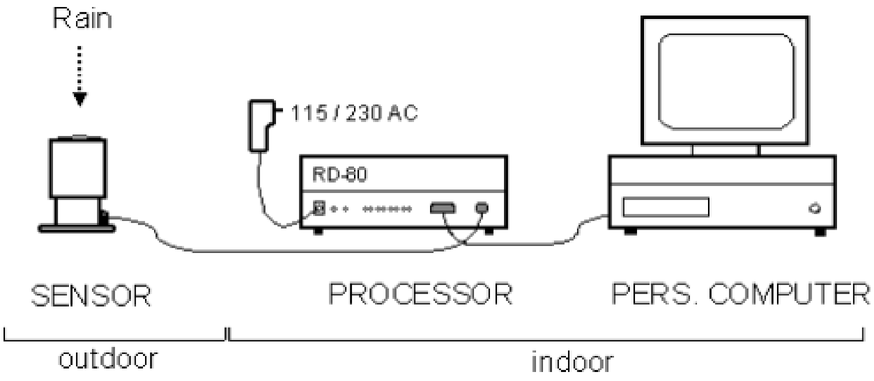

Figure 14: Disdrometer RD-80 Schematic Diagram of configuration [8]

From figure 13-14, the Ethernet link is used to send the signal from the outdoor to the indoor unit, where it undergoes signal processing algorithms to compute the required real-time rainfall parameters. The data that is generated from the indoor unit, is then archived to the microcomputer using the propriety software in a readable format file where it can be accessed for later use. The Joss and Waldvogel RD-80 disdrometer is installed at the rooftop, in Durban, University of KwaZulu-Natal, at the School of Electrical, Electronic and Computer Engineering.

A total of 31 451 rainfall events were recorded. Based on the recommendation of filtering and processing of disdrometer data, the rainfall events with a total sum of drops less than 10 were removed from the samples [78]. A total of 16845 samples were filtered and analysed throughout the measurement period, and they are classified into monthly (August 2019 to January 2020) and seasonal (winter, spring and summer) categories in Table 5.

Table 5: INFORMATION OBTAINED FROM RD-80 DISDROMETER FOR THE PERIOD OF MEASUREMENT

CATEGORY	NUMBER OF SAMPLES FILTERED	MAXIMUM RAINFALL INTENSITY (mm/h)
Research Period	16 845	158.2707
	MONTHLY	
August	647	6.1600
September	1 141	86.2537
October	3 119	101.9721
November	9 492	158.2707
December	2 251	81.8786
January	195	50.6797
	SEASONAL	
Winter	647	6.1600
Spring	13 752	158.2707
Summer	2 446	81.8796

4.2 Rain Intensity Modeling

The ITU-R recommends aiming for 99.99 percent system availability when developing a microwave link; as a result, the rainfall rate (R0.01) in the region of interest must be determined for 0.01 percent of the time. The statistical information obtained is based on the rainfall intensity CDF in Durban, South Africa. The analysis is done based on seasonal and monthly rainfall intensity using the above disdrometer data between August 2019 and January 2020.

4.2.1 Monthly Distribution

Figure 15-20 shows the monthly cumulative rainfall intensity distributions in Durban, South Africa, for each month. Table 6 shows the percentage exceedances of rainfall intensity at 0.01 %, 0.1 %, 1 %, and 10%, as determined from Figure 15-20. November has the highest rainfall intensity, with R0.01 = 120 mm/h, while August has the lowest, with R0.01 = 6 mm/h. In general, as indicated in Table 6, monthly rainfall intensity values R0.01 in Durban are highest from September to November, i.e., during the spring season. Winter has an extremely low rainfall intensity value of R0.01, which is due to the fact that there is almost no rain in Durban during that time of year. According to these findings, the wettest months in Durban are October and November.

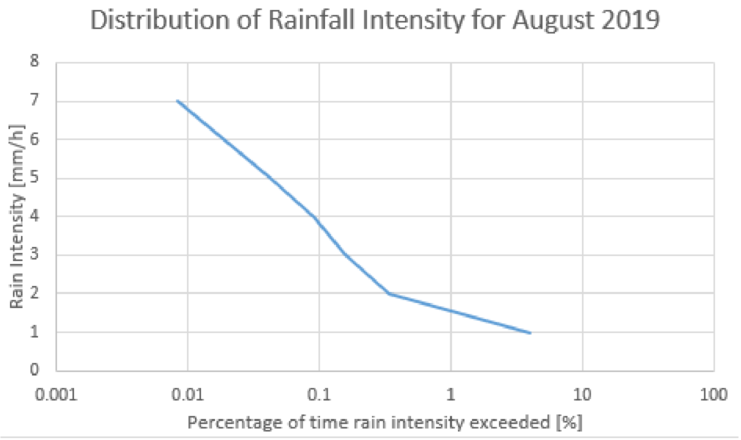

Figure 15: Rain Intensity profile for August 2019

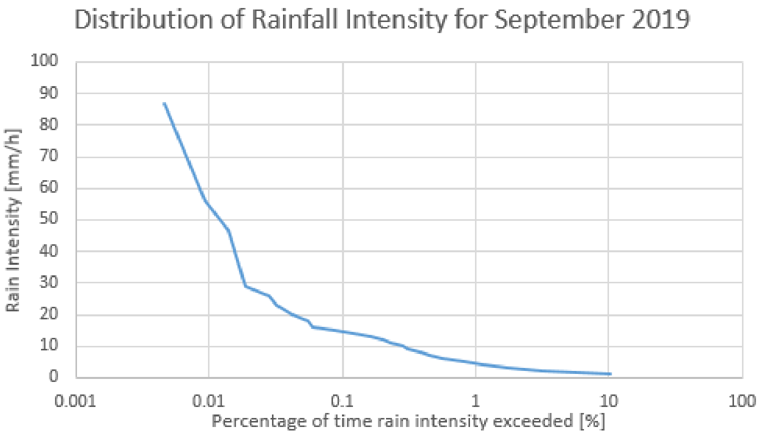

Figure 16: Rain Intensity profile for September 2019

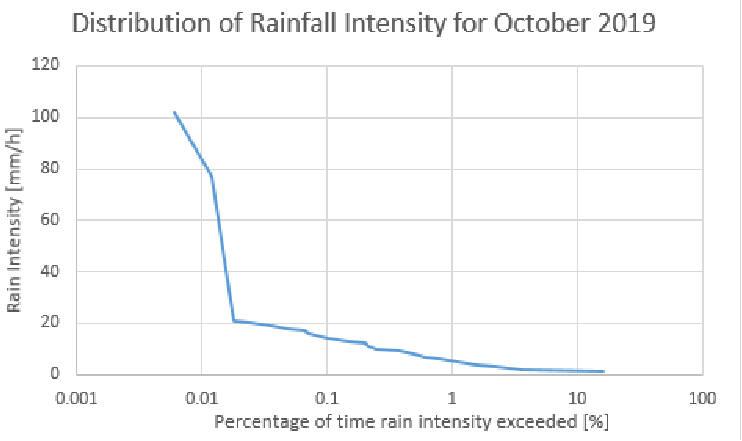

Figure 17: Rain Intensity profile for October 2019

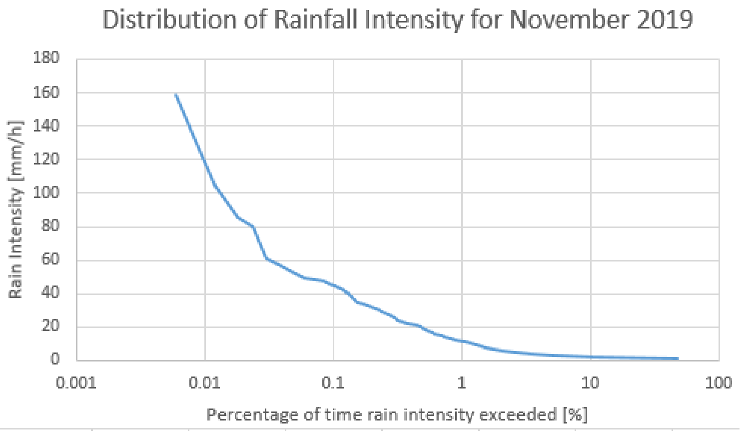

Figure 18: Rain Intensity profile for November 2019

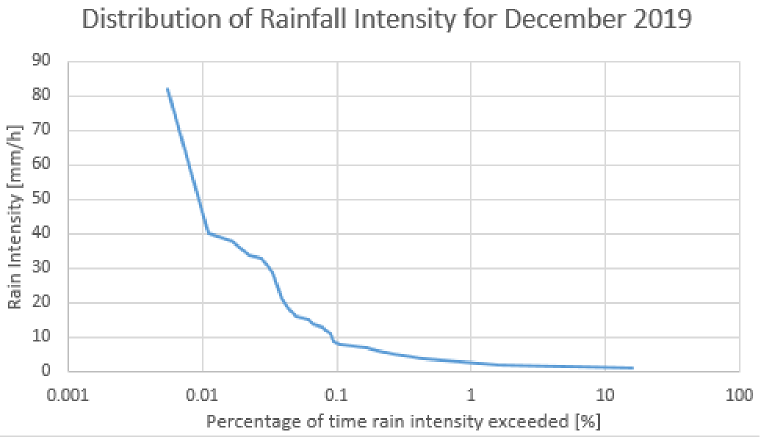

Figure 19: Rain Intensity profile for December 2019

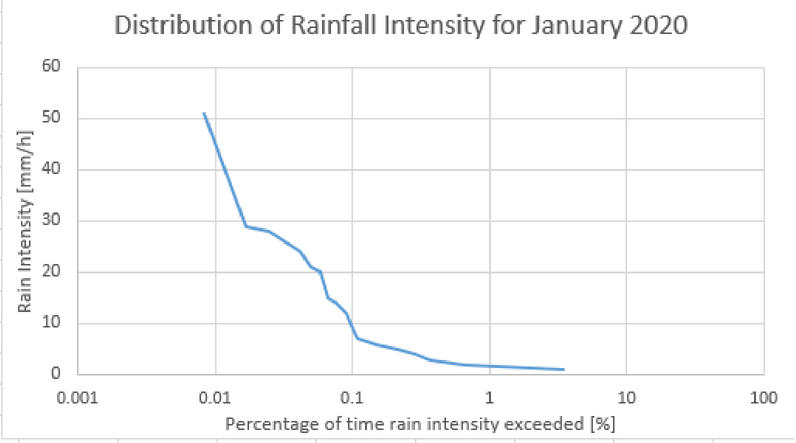

Figure 20: Rain Intensity profile for January 2020

Table 6: Monthly Statistics of Rainfall Intensity exceeded in mm/h

Monthly	Percentage of time rain intensity is exceeded (%)			
	0.01	0.1	1	10
August	6.85 mm/h	3.85 mm/h	1.5 mm/h	-
September	56 mm/h	14.5 mm/h	4.5 mm/h	1.1mm/h
October	82 mm/h	14 mm/h	5 mm/h	1.2 mm/h
November	119 mm/h	46 mm/h	11.5 mm/h	2.2 mm/h
December	46 mm/h	9 mm/h	2.4 mm/h	1.2 mm/h
January	45 mm/h	9 mm/h	1.5 mm/h	-

4.2.2 Seasonal Distribution

Figure 21 shows the seasonal cumulative rainfall intensity distribution throughout the same measurement period. Figure 21 shows that the maximum seasonal rainfall intensity values of R0.01 occur in the spring, followed by the summer and winter seasons, respectively.

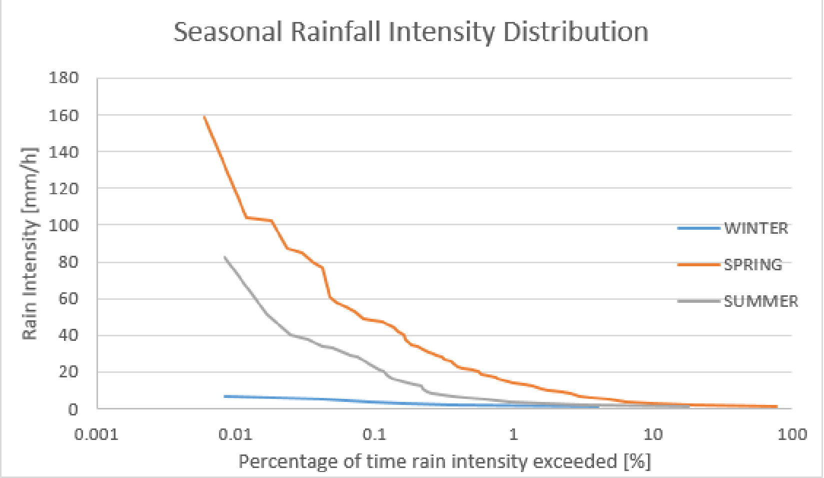

Figure 21: Seasonal Rain Intensity profile for period of experiment

The rainfall intensity exceedance for the spring season at R0.01 is 119 mm/h, according to Figure 21. R0.01 is 68 mm/h in the summer and 6.85 mm/h in winter, respectively. Table 7 summarizes the seasonal rainfall intensities for 0.01 %, 0.1 %, 1 %, and 10% of time, respectively.

Table 7: Seasonal Monthly Statistics of Rainfall Intensity exceeded in mm/h

Seasonal	Percentage of time rain intensity is exceeded (%)			
	0.01	0.1	1	10
Winter	6.85 mm/h	3.85 mm/h	1.5 mm/h	-
Spring	119 mm/h	47.5 mm/h	14 mm/h	2.5 mm/h
Summer	68 mm/h	24 mm/h	4 mm/h	1.2 mm/h

4.3 Rain DSD Modeling

In this section the relationship between DSD and rain intensity is discused. From the disdrometer data, the rainfall drop-size distribution, can be determined using the equation given as:

$$N(D_i) = \frac{C_i}{A \times T \times v(D_i) \times \Delta D_i} \; [m^{-3} mm^{-1}] \tag{45}$$

where A is Sampling area = 0.005 m^2, Sampling Time (30 seconds), C_i is a number of raindrops available at the ith diameter bin, D_i is average diameter of the ith bin, $v(D_i)$ is fall velocity, and ΔD_i is diameter interval of the raindrops.

The following figures 22-30 shows the relationship between the rain drop-size distribution and the rain intensity for different seasons, and also the months during the experimental period:

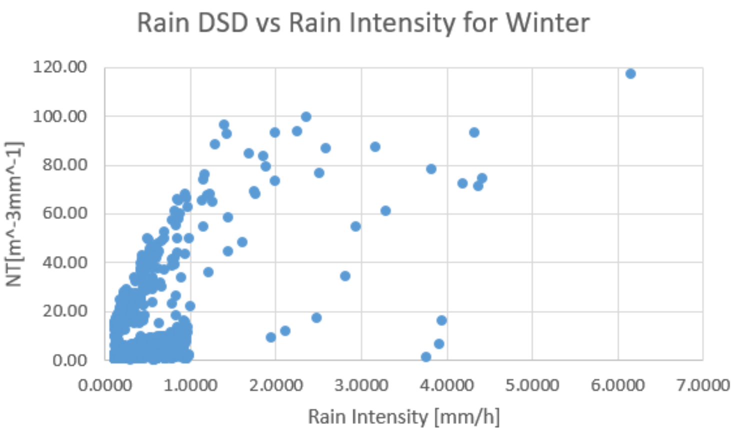

Figure 22: Rain DSD profile for winter season

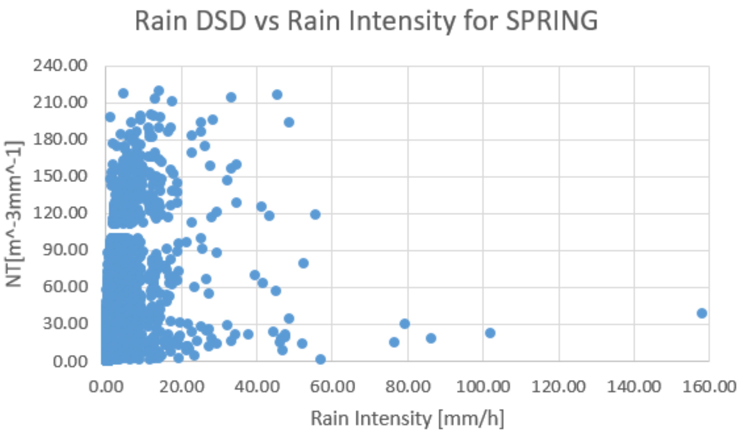

Figure 23: Rain DSD profile for spring season

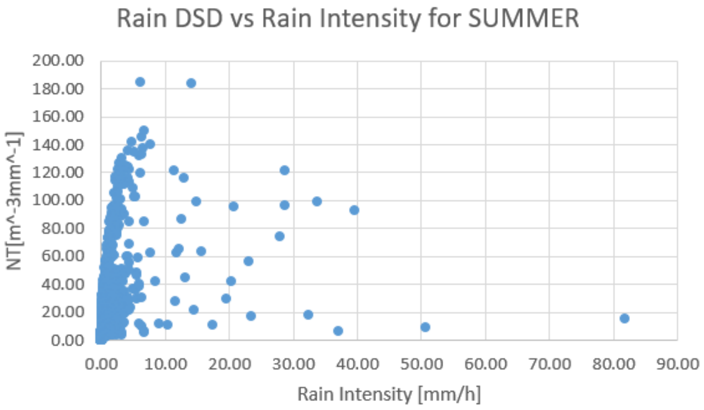

Figure 24: Rain DSD profile for summer season

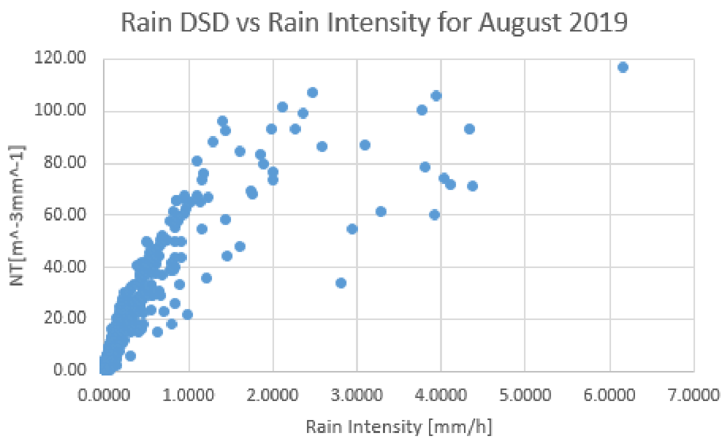

Figure 25: Rain DSD profile for August 2019

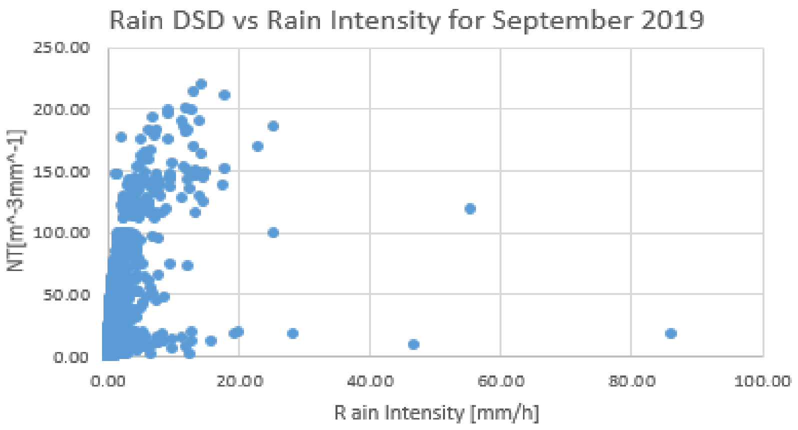

Figure 26: Rain DSD profile for September 2019

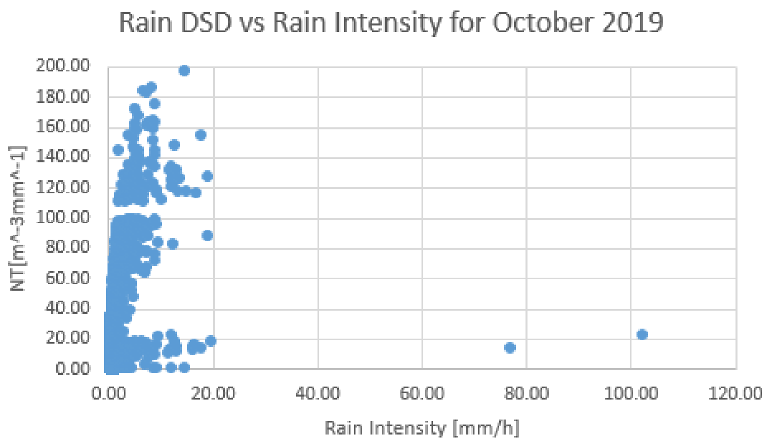

Figure 27: Rain DSD profile for October 2019

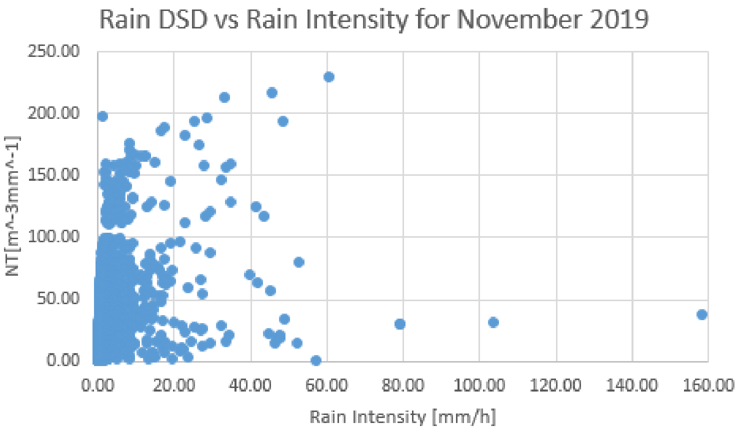

Figure 28: Rain DSD profile for November 2019

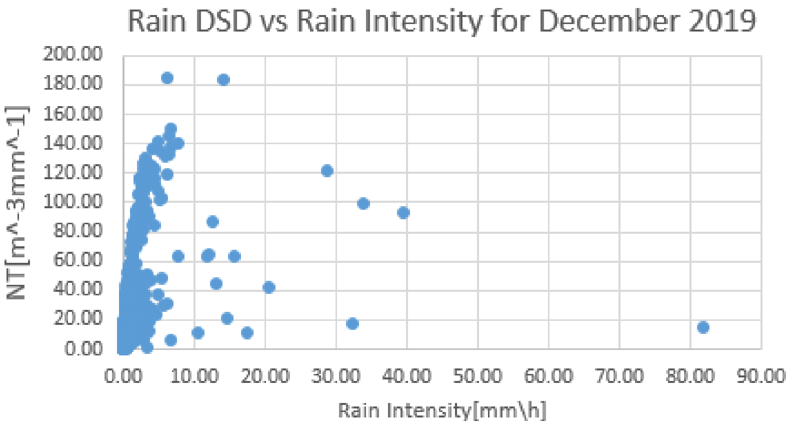

Figure 29: Rain DSD profile for December 2019

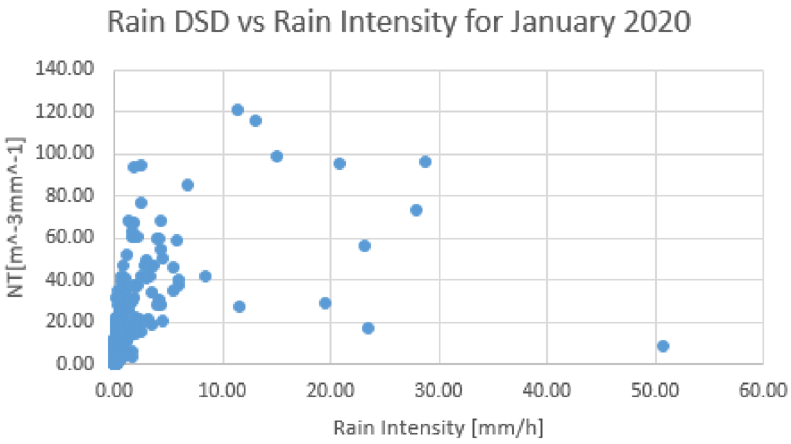

Figure 30: Rain DSD profile for January 2020

4.4 Chapter Summary

In this chapter, disdrometer data collected in Durban, South Africa between August 2019 and January 2020 have been used to model the rain intensity, and DSD. From the rain intensity modelling, R0.01 for different months and seasons was determined, as shown in figures. During this period, there was a presence of different rainfall events, which are drizzle, widespread, shower and thunderstorm rainfall event. The results for DSD profile shows that most rain was drizzle, widespread and some shower, there was not much thunderstorm. The next chapter focuses on the results and analysis of the effect of rain in the optical signal received.

CHAPTER 5

RESULTS AND ANALYSIS

5.1 Introduction

In this chapter, rain attenuation will be determined and OWC link performance predicted for Durban, South Africa. Between August 2019 and February 2020, the power meter recorded the power signal level from the transceiver. Durban receives regular rain between October and March, according to the South African Weather Service (SAWS), with 100 mm or more of precipitation, as seen in Figure 31 [78]. The wettest month is January; however, the results for January were not fully obtained because the equipment was off for most of the early January days. Heavy rainfall was recorded during the months of October and November, according to the data. The majority of the measurements used in this study were performed during rainy days to establish the relationship between the amount of power received and the rain intensity. As a result, the atmospheric attenuation of the FSO link is measured in terms of rain intensity, which is obtained using the disdrometer and expressed in mm/hr. The received power was measured using a Thorlab PM100 optical power meter, which was used to connect the FSO receiver to the computer. While transmitting signal over the FSO link, the rain intensity and power received at the receiving transceiver were recorded daily at a 30 second interval.

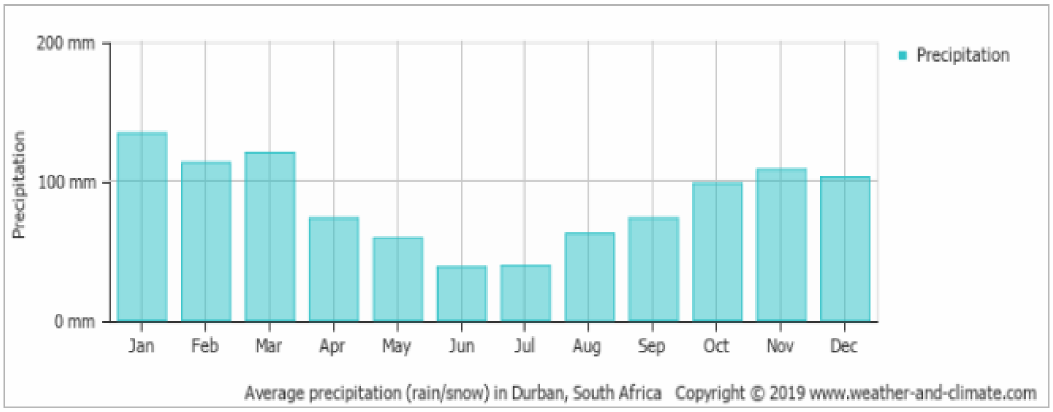

Figure 31: Average rainfall accumulation for Durban over the year 2019 [38]

As mentioned at the start of this section, the data was gathered over a six-month period that encompassed three distinct seasons. The rain does, in fact, affect the attenuation of the optical signal, as seen in the time series in Figures 33-42. It is further demonstrated that this attenuation is not just caused by rain, but also by other factors such as scintillation and fog. In comparison to rain, these variables appear to be producing higher attenuation. In the following sections, the connection between rain intensity and attenuation is plotted and reported.

5.2 Time Series of Rain Intensity and Received Optical Power

During the research period, the rain intensity time series and the corresponding optical received signal time series of various rain events. The synchronized rain intensity time series (in black) and received optical signal time series (in blue) for days where the highest received optical signal was recorded, light drizzle, and rainy days are shown in the plots.

5.2.1 Maximum received optical signal on a clear day

On the 1st of September 2019, Figure 32 shows the received optical signal time series. The rain intensity was quite low, approximately 0 mm/h for the majority of the day, because it was a clear day. The early morning optical received signal time series is plotted to check for any attenuation in the received optical signal and to determine what may be causing it, if there is any.

The received signal was weakened during the early hours of that specific day, as can be observed. There was attenuation of about 0.76 dB in the early hours of the day (4:00AM to 5:00AM), and attenuation of around 0.6 dB as the day progressed (8:00AM to 9:00AM). This is accomplished by subtracting the greatest received signal of 5.7603 dBm, which was recorded at 08:52AM, from the received signal of 5.0 dBm and 5.15 dBm, respectively, within that time period (one hour). Since there was no rain at this time, it may be argued that the signal attenuation during these times, as seen in Figure 32, is produced by fog and scintillation. Fog is more common in the early morning and late evening, therefore it's reasonable to assume that the attenuation between 4:00AM and 5:00AM is due to fog.

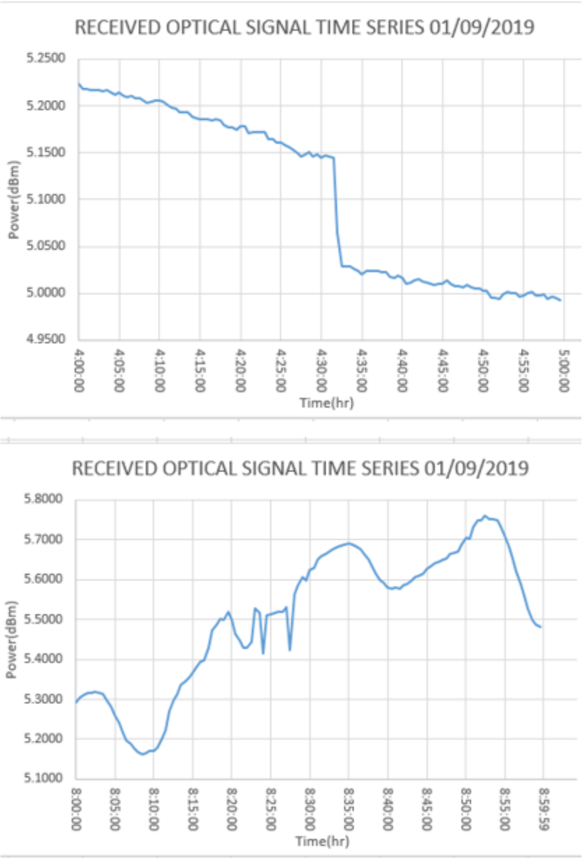

Figure 32: Received Optical signal time series on the 1st of September 2019

Figure 32 illustrates what has been discussed thus far. Because there was no rain on this day, there is no rain intensity time series. Some days, such as the 22nd of September 2019, in Figure 33, had a very low rain intensity, and they can also be classified as clear days. Figure 33 shows that the rain intensity at this time period, which is the evening and early afternoon, was less than 0.02 mm/h, which is a very low rain intensity. Even though the rain intensity was modest, the signal was nevertheless muted by 0.13 dB and 0.3 dB, respectively. As there is almost no fog in the early evening, the attenuation is most likely due to scintillation. This happened in the spring, when South Africa has a lengthy afternoon, which starts at 19:00.

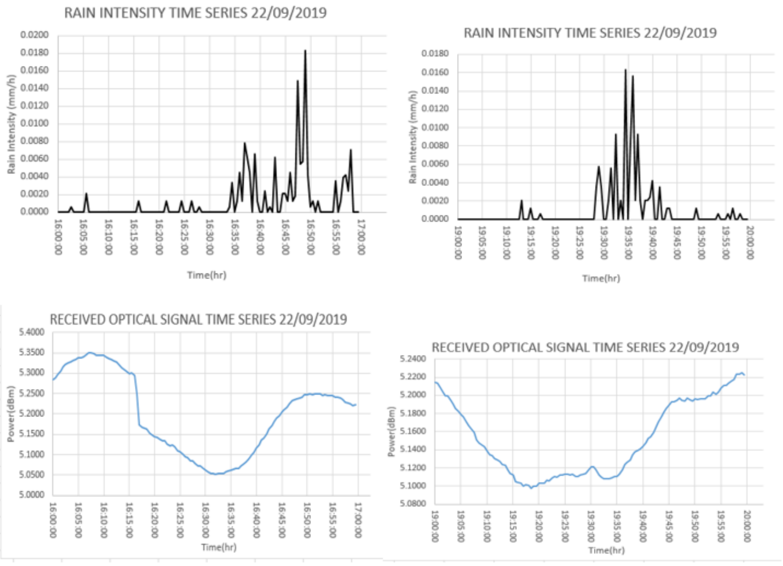

Figure 33: Rain Intensity and Received Optical signal time series for rain event on the 22nd of September 2019

5.2.2 Time Series of Light Drizzle Days

For the days when there was light drizzle, the rain intensity time series and the received optical signal time series are shown in the Figures below. The graphs are labelled, and each graph's title includes the date the findings were collected. The findings were obtained on several days and at various times. It's important noting that the rain intensity was quite low on several of these days, but there was still attenuation. This implies that, in addition to the rain intensity, there are other factors affecting the attenuation, such as fog and scintillation, as seen above.

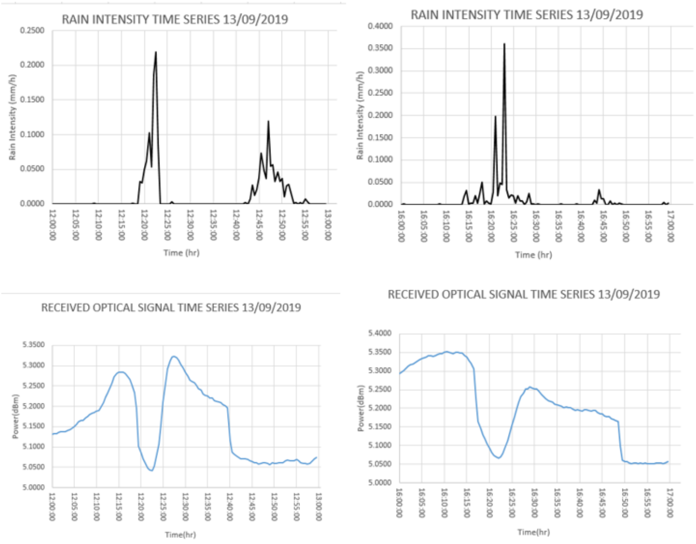

Figure 34: Rain Intensity and Received Optical signal time series for rain event on the 13th of September 2019

The greatest rain intensity for the period 12:00 to 13:00 on the 13th of September 2019, was 0.25 mm/h, and for the period 16:00 to 17:00 was 0.4 mm/h, as shown in Figure 34. The attenuations were almost 0.275 dB and 0.3 dB.

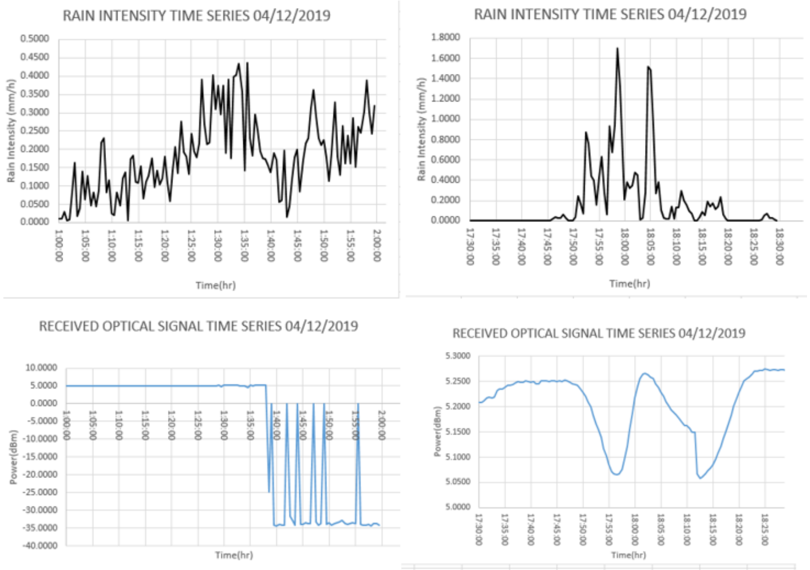

Figure 35: Rain Intensity and Received Optical signal time series for rain event on the 4th of December 2019

On the 4th of December 2019, the greatest rain intensity was 0.44 mm/h between 01:00 and 02:00, and 1.7 mm/h between 17:30PM and 18:30, as shown in Figure 35. It appears that the power meter malfunctioned in the early hours of the morning, recording negative findings. It was later repaired, and the signal received with attenuation of about 0.22 dB was recorded.

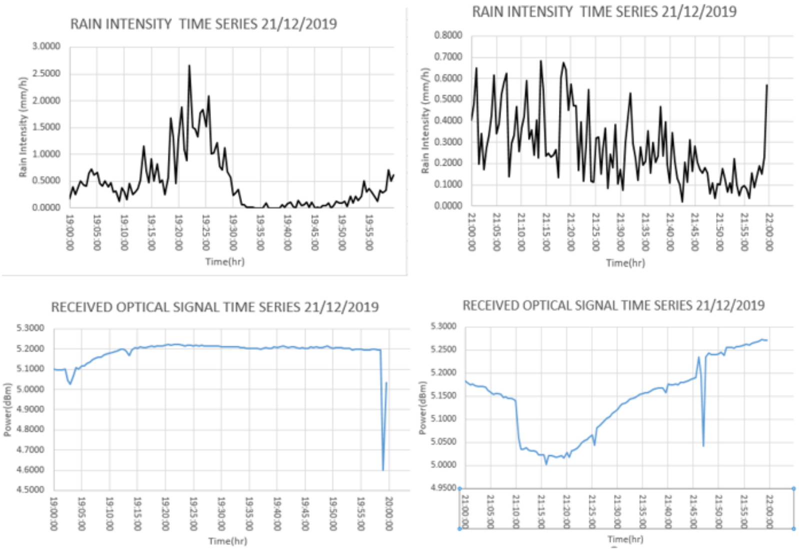

Figure 36: Rain Intensity and Received Optical signal time series for rain event on the 21st of December 2019

On the 21st of December 2019, the highest rain intensity for the interval 19:00 to 20:00 was 3 mm/h, and for the interval 21:00 to 22:00 was 0.7 mm/h, as shown in Figure 36. Attenuations were almost 0.6 and 0.3 decibels, respectively. Figure 36 shows that the signal received was not weakened for some time between 19:00 and 20:00, despite the fact that it was raining. Just before 20:00, the signal is heavily distorted. Even though the latter had less drizzle rain intensity than the former, it can be seen that the received optical signal time series was more consistent between 21:00 and 22:00. This proves that rain isn't the only thing that reduces signal strength. It's also possible that fog was beginning at those times, causing the attenuation of the received optical signal.

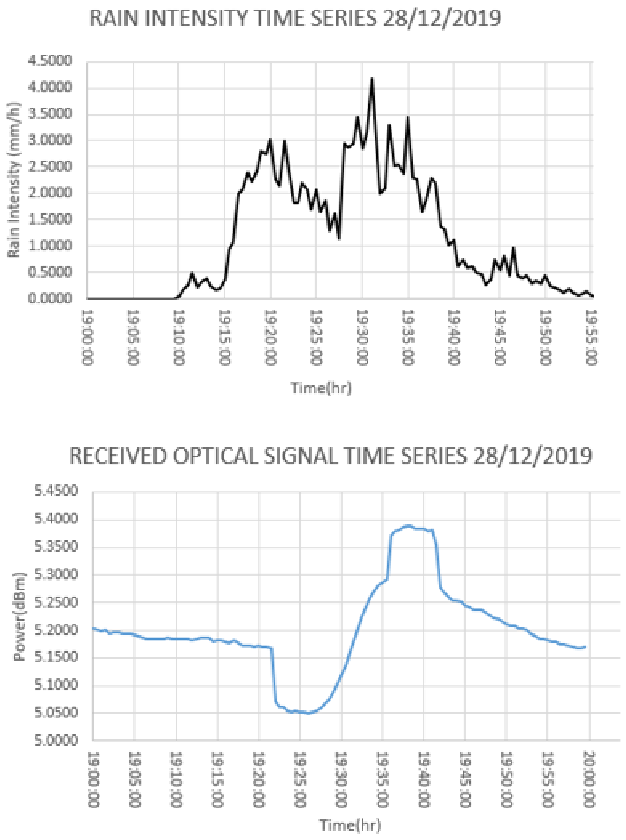

Figure 37: Rain Intensity and Received Optical signal time series for rain event on the 28th of December 2019

On the 28th of December 2019, the greatest rain intensity for the interval 19:00 to 20:00 was 4.5 mm/h, with attenuations of about 0.35 dB, as shown in Figure 37. The intensity of the rain is one of the variables affecting the attenuation of the received optical signal in this situation. Not to say that other factors aren't there, but the severity of the rain is one of them.

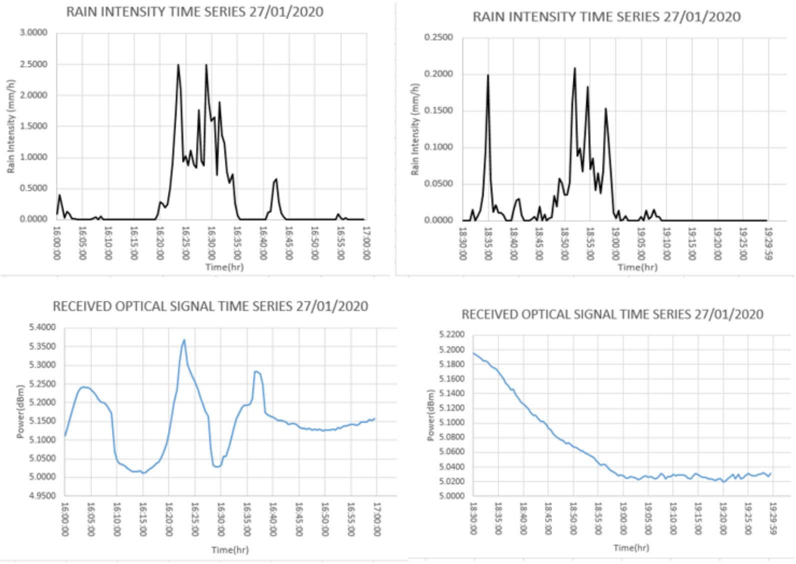

Figure 38: Rain Intensity and Received Optical signal time series for rain event on the 27th of January 2020

The received optical signal is attenuated due to rain and scintillation, as seen in Figure 38. Given that it was mid-summer and there was very little rain, especially between the hours of 18:30 and 19:30, it's reasonable to assume there was no fog at that time of day.

5.2.3 Time Series of Rainy Days

For rainy days, the rain intensity time series and the received optical signal time series are shown in the Figures below. The graphs are labelled, and each graph's title includes the date the findings were collected. All of the different forms of rainfall may be observed in some of the graphs, such as the ones from the 10th of November 2019 and the other from the 12th of November 2019 (Figures 39-42). Drizzle (0-5 mm/h), widespread (5-10 mm/h), shower (10-40 mm/h), and thunderstorm (40-120 mm/h) are all present. Rainfall events go through a shift from lower to higher rainfall kinds, which is known as the transition of events. It can be observed that as the rainfall intensity increases or decreases, the received power changes, and this difference is what causes rain attenuation.

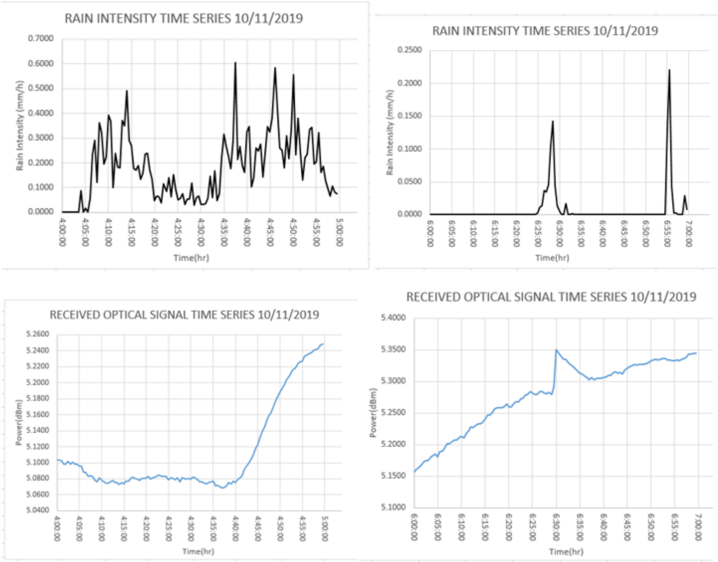

Figure 39: Rain Intensity and Received Optical signal time series for rain event on the 10th November 2019

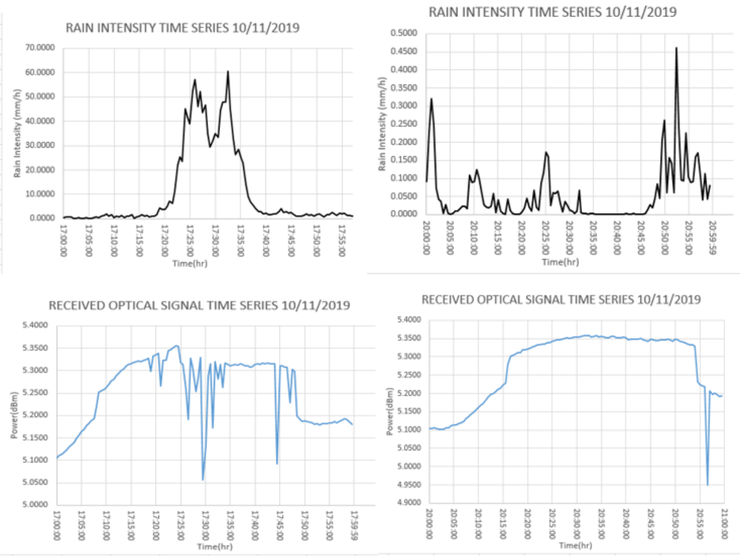

Figure 40: Rain Intensity and Received Optical signal time series for rain event on the 10th of November 2020

Rain intensity and received optical signal time series for the 10th of November 2019 are depicted in Figures 39-40, which are divided into various time periods. The received signal is attenuated between 17:20:00 and 17:40:00 as the rain intensity rises or transits from drizzle rain type to widespread rain type, to shower type, and finally to thunderstorm rainfall type of 60.5968 mm/h at 17:32:30 hours. This implies that there was some rain throughout that time period, causing some attenuation. Other variables producing the attenuation were also present on this day, as can be shown.

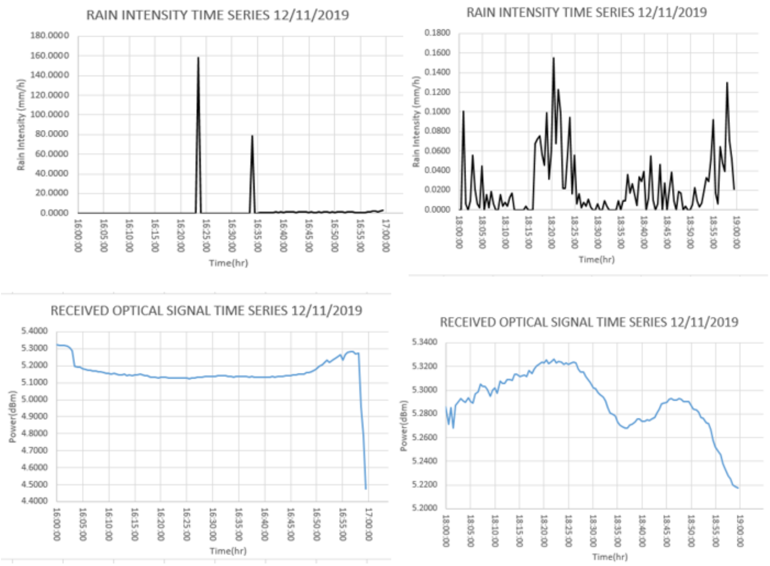

Figure 41: Rain Intensity and Received Optical signal time series for rain event on the 12th November 2019

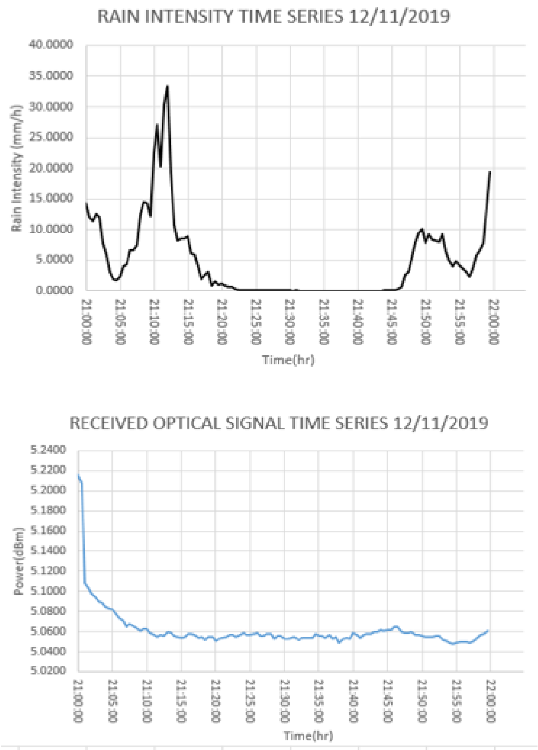

Figure 42: Rain Intensity and Received Optical signal time series for rain event on the 12th of November 2020

The attenuation is virtually constant between 16:00 and 17:00, which is the time period where the greatest rain intensity of 158.2702 mm/h was recorded, as seen in Figures 41-42 from the Optical received signal time series. This is owing to the fact that, in addition to the strength of the rain, there are additional elements that influence attenuation. These factors have been discussed above.

5.3 Attenuation

The maximum power recorded (dBm) at the transceiver, during the period of the experiment, which is mid-August 2019 to mid-February 2020, was 5.7603 dBm - which value was recorded on 1st September 2019 at 08:52 am. However, this value is not fixed for a given rain event. At any time, the “unfaded” received signal level varies, depending on whether there is fog, scintillation, or rain. Therefore, the signal power recorded at a certain time should be subtracted from the maximum value recorded during that particular period of measurement (or measurement event) to determine the rain attenuation in dB as shown in equation (46):

$$Loss\ [dB] = P_{max}\ [dBm] - P_{received}\ [dBm] \tag{46}$$

5.4 Measurements Attenuation Results and Analysis

This section will focus on the analysis of the results obtained from the measurements taken between August 2019 and January 2020. These results will be used to analyse the relationship between Specific attenuation in dB/km and rain intensity in mm/h, as well as the relationship between Attenuation in dB and rain intensity, and the raindrop diameter vs rain intensity.

South Africa has a variety of climatic changes that are reliant on seasonal cycles. These are: Summer (December to February); autumn (March to May); winter (June to August); and spring (September to November) [79]. The data for this study was obtained during three seasons, namely, winter, spring, and summer. However most of the data was collected during spring, which, together with summer, is South Africa's rainiest season. This section focuses on the analysis of the results obtained from measurements taken between August 2019 and January 2020. These findings will be used to study the relationship between rain intensity and attenuation due to rain, as well as the specific attenuation.

5.4.1 Plots of Rain Intensity vs Raindrop Diameter

The raindrop measurements were taken with a disdrometer. The disdrometer recorded both the raindrop diameter and the rain intensity. The raindrop diameter and rain intensity for the 13th of September 2019, the 22nd of September 2019, and the 10th of November 2019, as well as the times this was measured, are shown in the following tables, from table 8-10. In this section, a relationship between the raindrop diameter and rain intensity.

Table 8: RESULTS TAKEN FROM THE 13TH OF SEPTEMBER 2019

Time (Hours)	Raindrop Diameter (mm)	Rain Intensity (mm/h)
12:42:30	0.4550	0.0024
12:43:00	0.0000	0.0077
12:43:30	0.6560	0.0271
12:44:00	0.7710	0.0127
12:44:30	0.7710	0.0207
12:45:00	0.7710	0.0376
12:45:30	0.7710	0.0737
12:46:00	0.7710	0.0485
12:46:30	0.7710	0.0367
12:47:00	0.9130	0.1193
12:47:30	0.7710	0.0541
12:48:00	0.7710	0.0568
12:48:30	0.6560	0.0325
12:49:00	0.6560	0.0460
12:49:30	0.7710	0.0326
12:50:00	0.7710	0.0368
12:50:30	0.7710	0.0108
12:51:00	0.5510	0.0256
12:51:30	0.6560	0.0277
12:52:00	0.6560	0.0129
12:52:30	0.5510	0.0012
12:53:00	0.4550	0.0021
12:53:30	0.5510	0.0021
12:54:00	0.0000	0.0071
12:54:30	0.5510	0.0033

Table 9: RESULTS TAKEN FROM THE 22ND OF SEPTEMBER 2019

Time (Hours)	Raindrop Diameter (mm)	Rain Intensity (mm/h)
16:35:30	0.4550	0.0012
16:36:00	0.5510	0.0045
16:36:30	0.4550	0.0012
16:37:00	0.5510	0.0078
16:37:30	0.6560	0.0062
16:38:00	0.5510	0.0045
16:38:30	0.0000	0.0000
16:39:00	0.5510	0.0066
16:39:30	0.4550	0.0012
16:40:00	0.0000	0.0000
16:40:30	0.0000	0.0000
16:41:00	0.4550	0.0024
16:41:30	0.0000	0.0000
16:42:00	0.3590	0.0006
16:42:30	0.0000	0.0000
16:43:00	0.6560	0.0062
16:43:30	0.0000	0.0000
16:44:00	0.0000	0.0000
16:44:30	0.5510	0.0021
16:45:00	0.5510	0.0021
16:45:30	0.4550	0.0012
16:46:00	0.5510	0.0045
16:46:30	0.4550	0.0012
16:47:00	0.4550	0.0018

Table 10: RESULTS TAKEN ON THE 10TH OF NOVEMBER 2019

Time (Hours)	Raindrop Diameter (mm)	Rain Intensity (mm/h)
17:21:00	3.9160	7.1413
17:21:30	3.9160	6.3173
17:22:00	4.8590	11.2736
17:22:30	4.8590	21.9103
17:23:00	4.8590	25.4695
17:23:30	4.8590	23.6925
17:24:00	4.3500	45.0291
17:24:30	4.8590	41.6429
17:25:00	4.3500	39.0680
17:25:30	4.8590	52.4915
17:26:00	4.8590	57.1462
17:26:30	4.3500	46.2185
17:27:00	3.9160	52.2519
17:27:30	4.3500	43.5771
17:28:00	4.3500	46.6759
17:28:30	3.9160	34.8337
17:29:00	3.5440	29.5744
17:29:30	3.9160	32.2178
17:30:00	3.5440	34.8827
17:30:30	4.3500	33.3613
17:31:00	3.9160	44.6199
17:31:30	4.3500	47.7912
17:32:00	3.9160	48.0561
17:32:30	3.9160	60.5968
17:33:00	3.9160	45.0398
17:33:30	2.8690	33.0178

The results in the tables above were collected on days chosen at random to demonstrate the relationship between raindrop diameter and rainfall intensity. The relationship between rain intensity in mm/h and raindrop size (diameter) in mm is shown in the graphs below in Figures 43-45. The measurements that were analyzed were obtained on three distinct days, as mentioned above; Figures 43-45 show the data from

September 13th, September 22nd, and November 10th 2019, respectively. Figures 43-45 correspond to table 8-10 results, respectively.

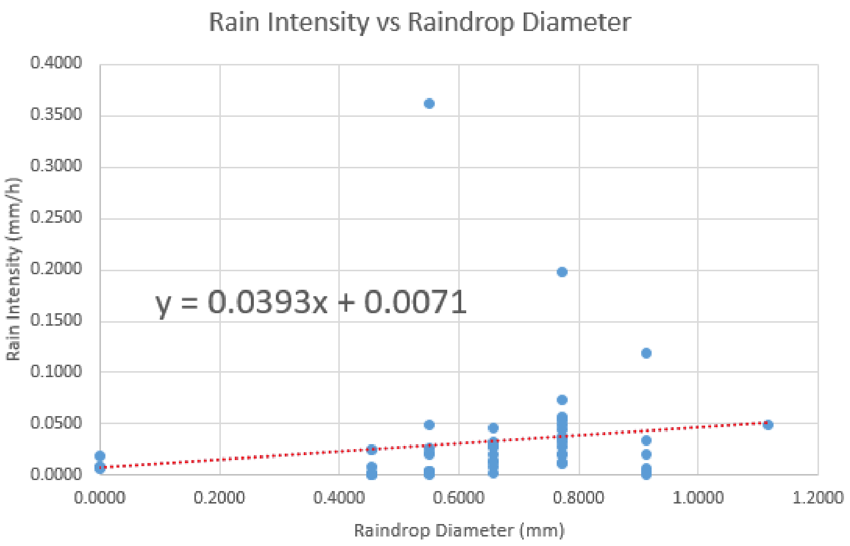

Figure 43: Rain Intensity vs Raindrop Diameter for measurements taken on the 13th of September 2019

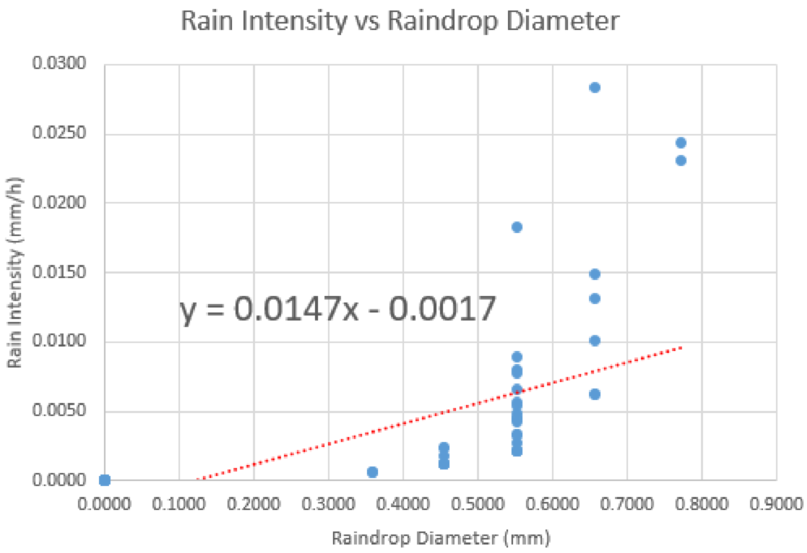

Figure 44: Rain Intensity vs Raindrop Diameter for measurements taken on the 22nd of September 2019

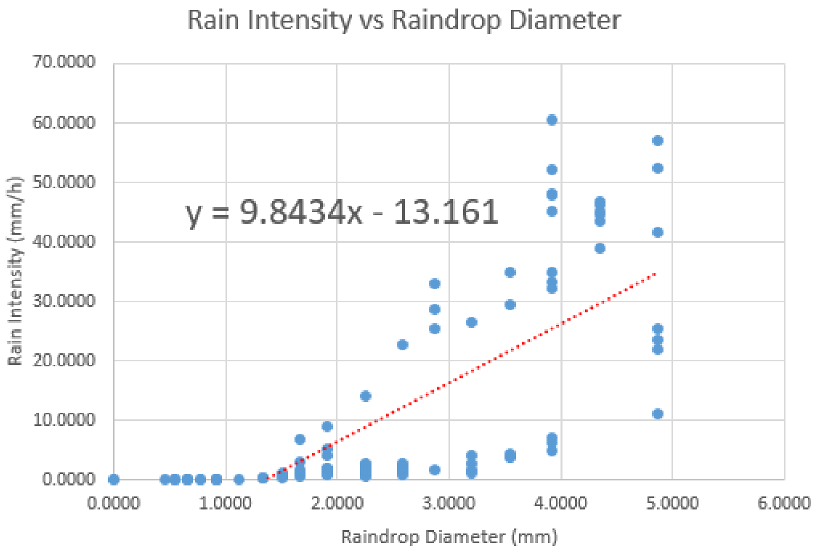

Figure 45: Rain Intensity vs Raindrop Diameter for measurements taken on the 10th of November 2019

The relationship between rain intensity and raindrop diameter is shown in Figures 43-45 above. The graphs in these Figures are represented by a linear trend-line, which shows nearly perfect linear behaviour of average raindrop diameter and rain intensity. The Figures also indicate a steeper slope, indicating that as the average raindrop diameter increases, so does the rain intensity. These graphs also illustrate that a smaller raindrop diameter results in less rain intensity, or that the smaller the raindrop diameter, the less rain intensity.

As it can be seen that the results in Figure 44 have small raindrop diameters, which results in the small rain intensity. The raindrop diameters in Figure 43 are bigger than those in Figure 44 but less than those in Figure 45, which results in Figure 43 showing the rain intensity bigger than that of Figure 44 and less than that of Figure 45. It then can be concluded that there was a heavy rain on the 10th of November 2019 as compared to the 13th and 22nd of September 2019, and in the later days it can be said that it was drizzling, or there was light rain.

Raindrops with a diameter less than 0.5 mm are considered drizzle, those with a diameter greater than 0.5 mm but less than 2 mm are considered light rain, those with a diameter greater than 2 mm but less than 6 mm are considered light rain, and those with a diameter greater than 6 mm are considered heavy rain [80]. However, there is little variation in rain attenuation on these days, leading to the conclusion that signal attenuation is dependent not only on rain intensity, but also on other parameters such as raindrop size, transceiver alignment, and the amount of wind on that particular day. Even though the weather station is not available to validate the assumption that wind can be a factor, [81] the alignments of the transceivers play a vital role because OWCS requires a direct LOS path between the transmitter and the receiver, so the wind does play a role in shifting the alignment.

5.5 Rain Attenuation Modelling

In chapter four, the results obtained were shown, and briefly discussed. It also shows that rain does indeed attenuate the optical signal, and that not only rain, but other factors too such as scintillation and fog. In this chapter, the analysis on the attenuation and specific attenuation due to rain will be done. Also how the empirical method was used for the modelling and prediction of rain attenuation will be shown. What can also be observed in chapter four is that the obtained rain results do agree with the information from SAWS that Durban experiences rain between October and March [78].

5.5.1 Obtaining Results

Chapter three explains in the details the methods and equipment used to obtain or record the results used for the analysis. In section 4.2 it can be seen that the maximum power (P_{max}) recorded (dBm) at the receiving transceiver was (5,7603dBm), and this value was recorded at 08:52 am on 1 September 2019, using the Optical Power Meter, as detailed in section 3.3.

5.5.2 Calculating Specific Attenuation

The measured attenuation is calculated between the two transceivers with respect to a fixed distance (L) in kilometers, and the specific attenuation is then determined as attenuation with respect to distance in (dB/km). It is calculated as follows:

$$Specific\ Attenuation\ [dB/Km] = \frac{Loss\ [dB]}{L\ [km]} \tag{47}$$

In this particular case, the link length of 7 meters or 0.007 kilometers is used. Thus, in (47), L is equal to 0.007 for all the calculations.

5.5.3 Analysis of Monthly Rain Attenuation Prediction Models

5.5.3.1 Plots of Attenuation and Specific Attenuation due to Rain

The relationship between Attenuation in dB and Specific Attenuation in dB/km due to Rain Intensity in mm/h is shown in Figure 46-51 below. As previously noted, the measurements were taken over a 6-month period. The Figures show the outcomes obtained between August 2019 and January 2020.

As previously stated, rain attenuation modelling and prediction can be performed using either an empirical or physical method. Since the empirical technique is based on the relationship between the observed attenuation distribution and the related observed rain intensity distribution estimated at 30 seconds integration time, it was chosen in this case. As a result, the specific attenuation is a fundamental variable in estimating rain attenuation statistics for both the earth and terrestrial space paths [82]-[89]. The rain specific attenuation is shown by the power law equation (1).

Since raindrops are assumed to have a spherical form, estimates of $k \text{ and } \alpha$ do not depend on vertical and horizontal polarization, as mentioned is section 2.3 above. That means k and α coefficients will depend only on the carrier frequency of the OWCS, temperature, and DSD [7]. All the below measurements were taken at an optical wavelength of 850 nm as mentioned above.

The relationship between Specific attenuation in dB/km and rain intensity in mm/h, as well as the relationship between Attenuation in dB and rain intensity, are shown in the plots in Figures 46-51. The trend-lines in Figures 46-51 show a rise in specific rain attenuation as the rain intensity increases.

Figure 46 shows the plots for the month of August. The rain rate for this month ranges from 0 to 5 mm/h with a maximum rain attenuation of almost 1 dB. The power model is used to determine the experimental data points for this month, and the equation obtained was $y = 82.702x^{0.0105}$, where y is the specific rain attenuation and x is the rain intensity. The $k \text{ and } \alpha$ coefficients are 82.702 and 0.0105, respectively. All Figures, from Figure 46-51 also shows the similar trend. The $k \text{ and } \alpha$ coefficients for either graph can easily be seen in the Figures above. It can also be observed that the rain intensity was high during the months of October, November, and December which shows that it was in a rainy season, as [78] states that these months falls under rainy season in Durban.

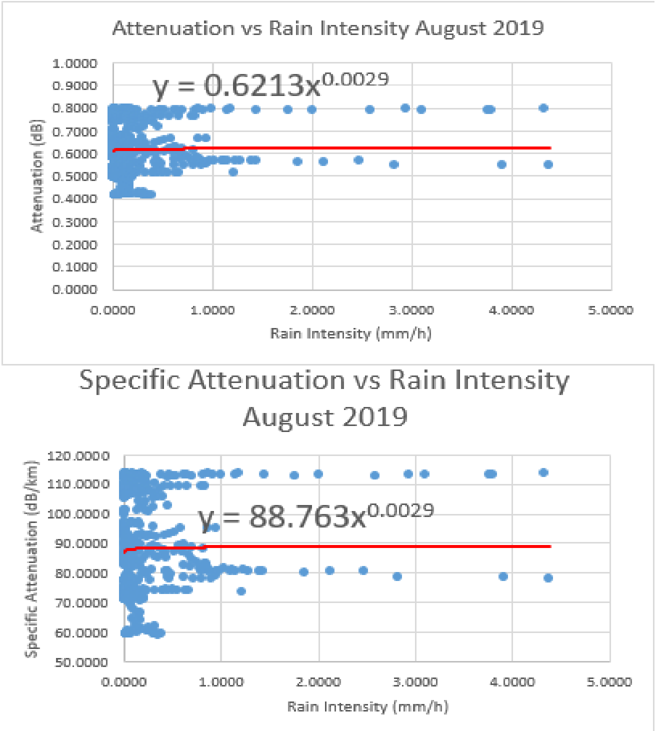

Figure 46: Specific Attenuation & Attenuation vs. Rain Intensity plot for August 2019

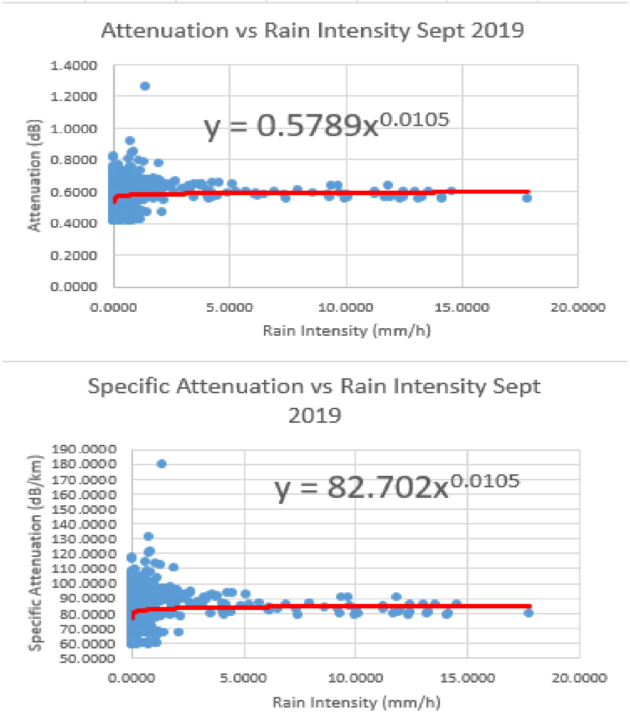

Figure 47: Specific Attenuation & Attenuation vs. Rain Intensity plot for September 2019

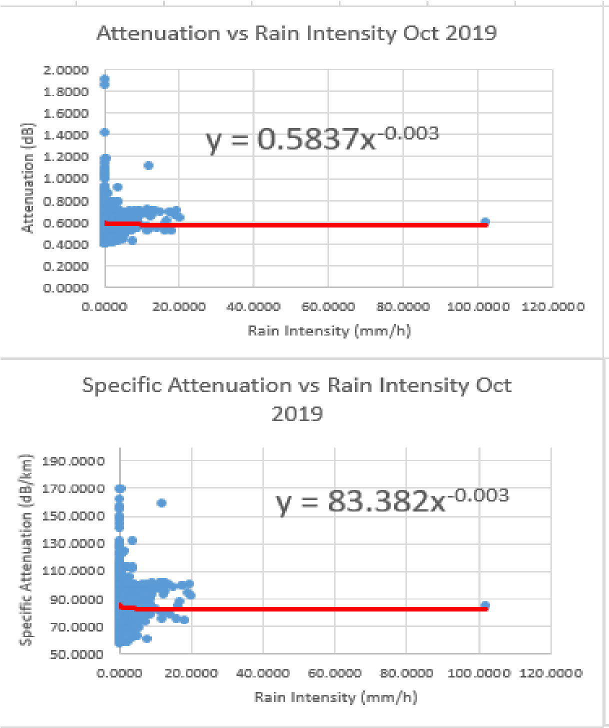

Figure 48: Specific Attenuation & Attenuation vs. Rain Intensity plot for October 2019

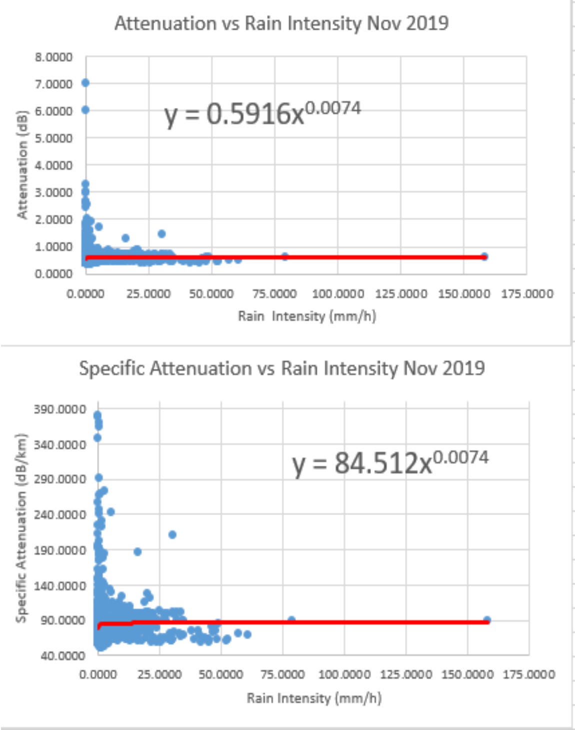

Figure 49: Specific Attenuation & Attenuation vs. Rain Intensity plot for November 2019

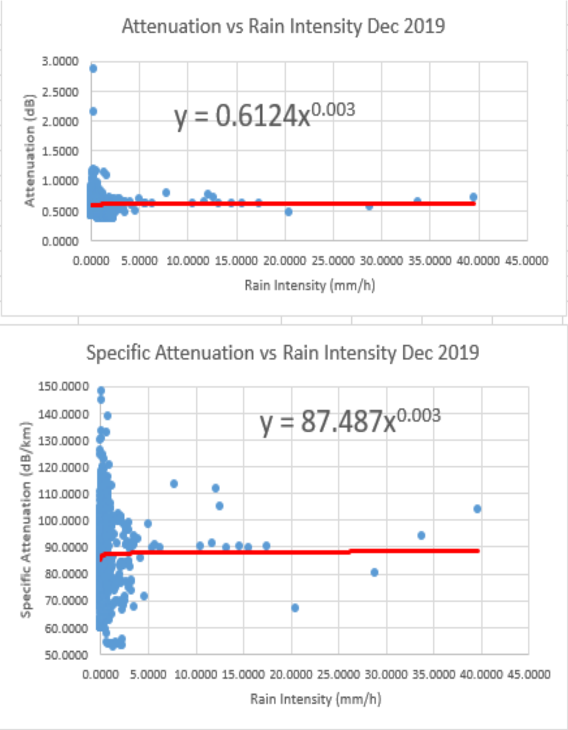

Figure 50: Specific Attenuation & Attenuation vs. Rain Intensity plot for December 2019

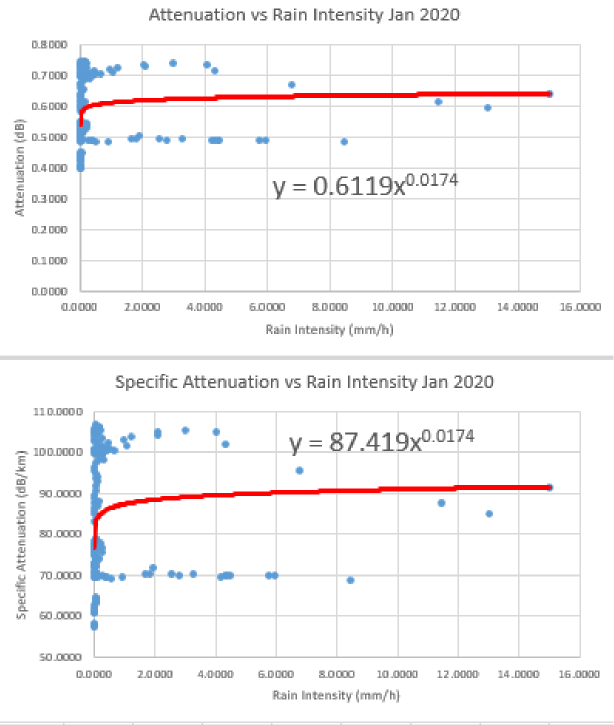

Figure 51: Specific Attenuation & Attenuation vs. Rain Intensity plot for January 2020

The power model is used to determine the experimental data points for this month, and the equation obtained. The other figures (Figure 52-55) shows the specific attenuation vs rain intensity during certain days from when the results were taken. This shows that as much as in some of these months it was raining, but some days it was clear, they can be referred to clear days, as much as it was drizzling, but the rain intensity was as low as less than 0.1 mm/h in some of them.

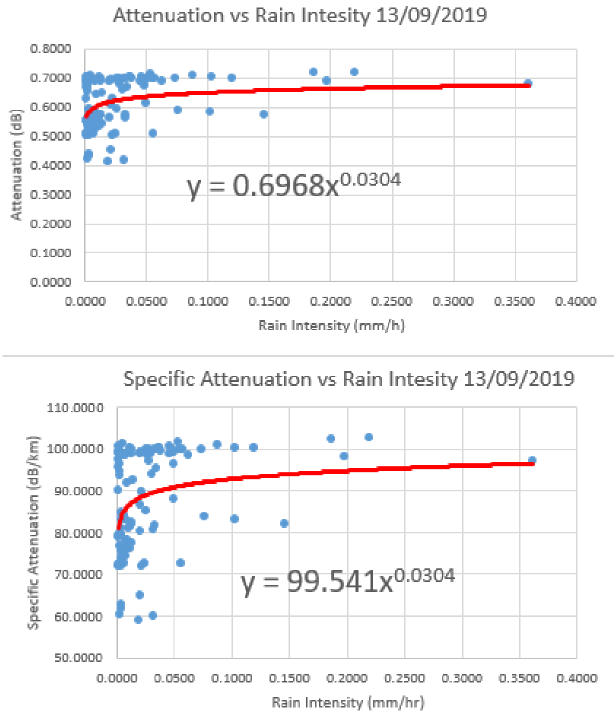

Figure 52: Specific Attenuation & Attenuation vs. Rain Intensity plot for 13th of September 2019

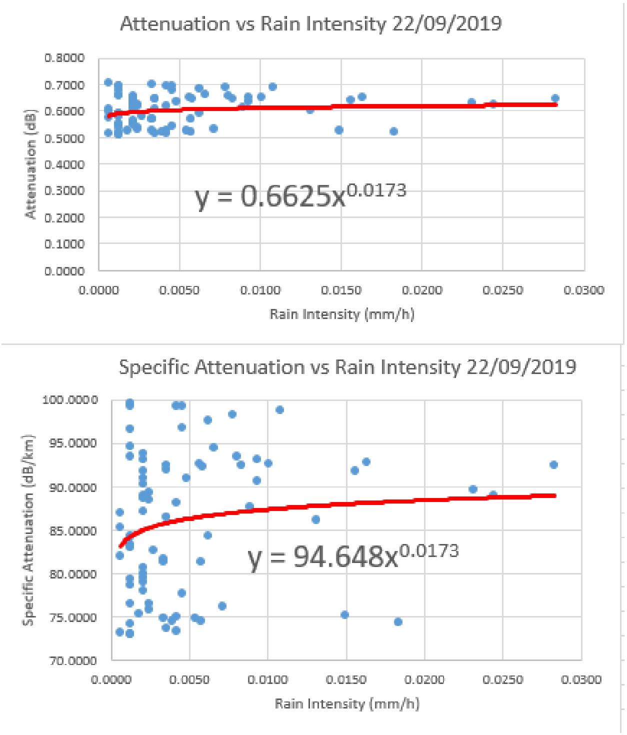

Figure 53: Specific Attenuation & Attenuation vs. Rain Intensity plot for 22nd of September 2019

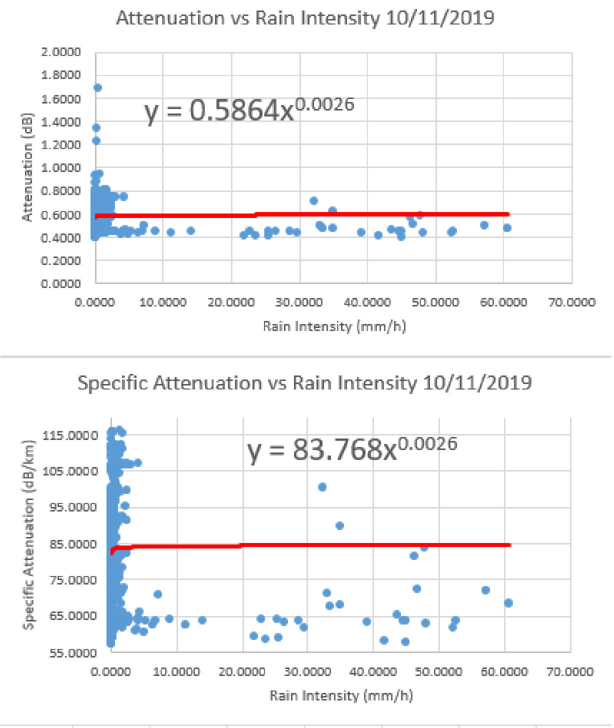

Figure 54: Specific Attenuation & Attenuation vs. Rain Intensity plot for 10th of November 2019

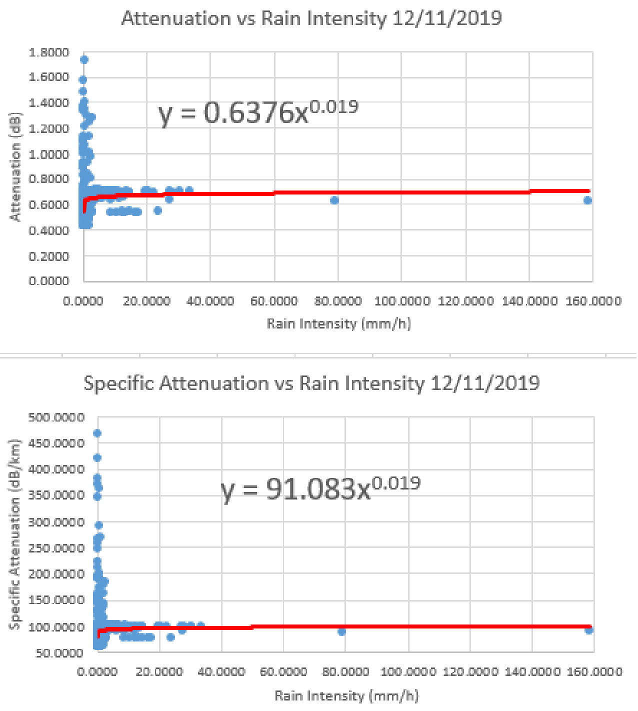

Figure 55: Specific Attenuation & Attenuation vs. Rain Intensity plot for 12th of November 2019

It is crucial to note that the days listed above were chosen at random with the goal of displaying various data categories such as clear days and rainy days. Starting with Figures 52-53, which show the results obtained on September 13th and 22nd, 2019, respectively. These are some of the clearest days of the year, especially on September 22nd, 2019, with the maximum rain intensity of 0.0283 mm/h. The maximum rain intensity recorded on September 13th, 2019 was 0.3615 mm/h. The results collected on rainy days, the 10th and 12th of November 2019, which in this case was the rainiest month of the season, are shown in the Figures 54-55, respectively. On the 10th of November the maximum rain intensity recorded was 60.5968 mm/h, and on the 12th of November the maximum rain intensity was 158.2707 mm/h, which was also the highest rain Intensity value recorded during the period of data collection.

5.6 Comparison with Existing Models

The results obtained had to be compared with the results from other countries to check if they were in correlation with other existing models. For this comparison, the French rain attenuation prediction model for FSO rain attenuation is also plotted alongside the scatterplots for the measurements, to give the predicted attenuation due to rain in Durban. The ITU-R rain attenuation prediction model for FSO system provided the k and α coefficients for the French model [5]. It is also important to note that the French model for

FSO attenuation is for drizzle rain that is rain intensity of 0.1-5 mm/h. Therefore, for this comparison the results for the period of this research, only the drizzle rainfall event will be used.

5.6.1 Plots of Attenuation and Specific Attenuation due to Rain with Comparison to French Model

The relationship between Specific attenuation in dB/km and rain intensity in mm/h, as well as the relationship between Attenuation in dB and rain intensity, are shown in the plots in Figures 56-61. As shown in the Figures, the rain regime considered for this reporting is the drizzle type, with rain intensities ranging from 0.2 to 5 mm/h. The trend-lines in Figures 56-61 show a rise in specific rain attenuation as the rain intensity increases, with a maximum rain intensity of slightly less than 5 mm/h. For example, the modelled attenuation due to rain equation in Durban in August 2019, which is the last month of winter and the start of spring, is $y = 88.763x^{0.0029}$, where y is the specific rain attenuation and x is the rain intensity, as seen in Figure 56. The $k\ and\ \alpha$ coefficients are 88.763 and 0.0029, respectively. On the right plots of the Figures, the predicted attenuation obtained using the French model can also be seen. The equations for specific attenuation and attenuation for the other months are shown in the other Figures.

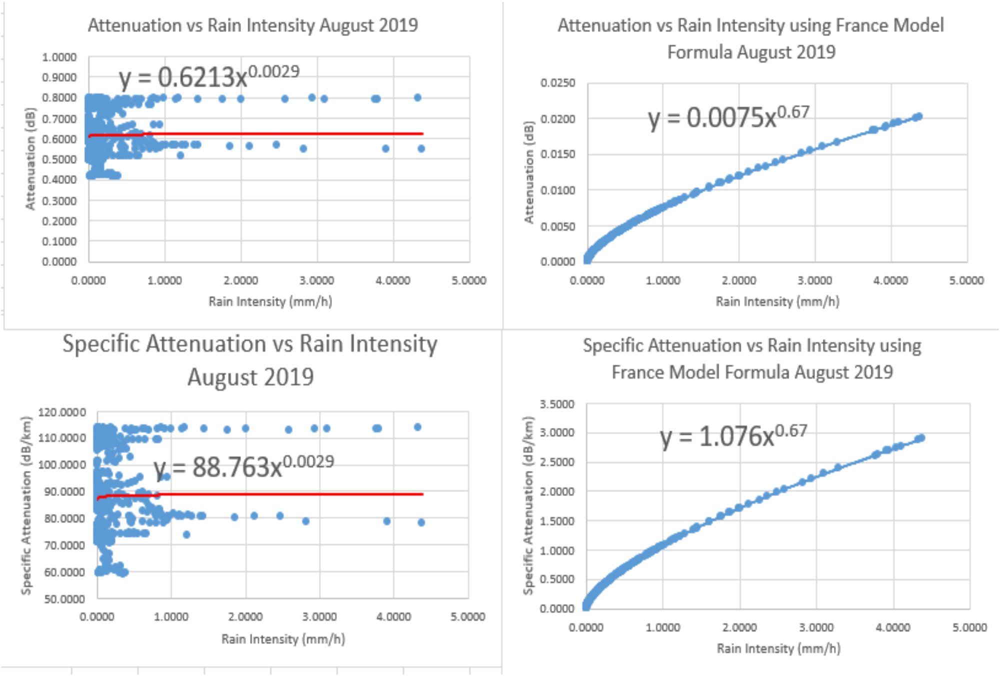

Figure 56: Specific Attenuation & Attenuation vs. Rain Intensity plots with French Model for August 2019

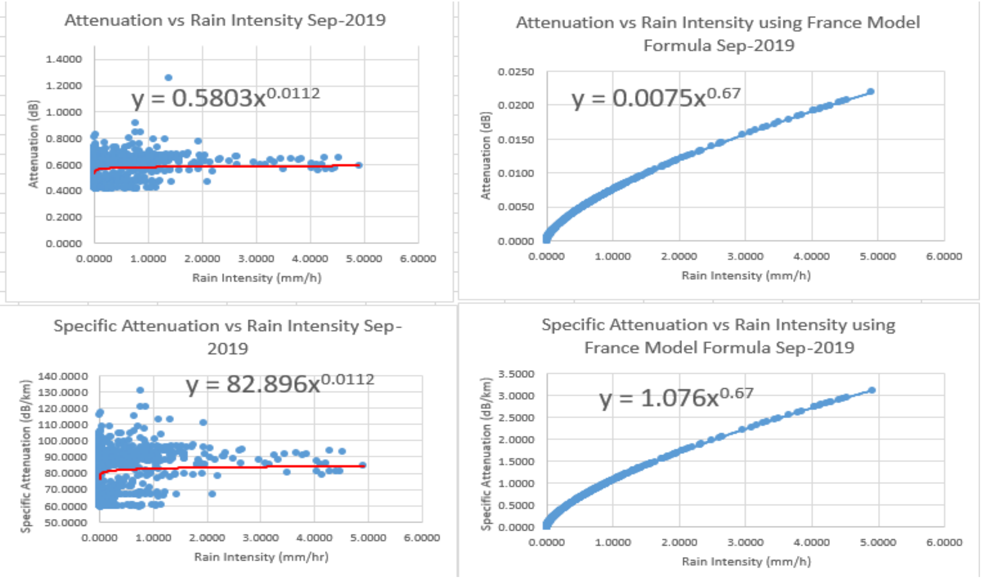

Figure 57: Specific Attenuation & Attenuation vs. Rain Intensity plots with French Model for September 2019

In Figure 57, the modelled attenuation due to rain equation in Durban for September 2019, is $y = 82.896x^{0.0112}$, where y is the specific rain attenuation and x is the rain intensity. The k and α coefficients are 82.896 and 0.0112, respectively. As previously stated, September is the first month of spring. September saw more clear days and less rainy days, as seen in section 4. As a result, it's reasonable to conclude that other variables, such as fog and scintillation, were responsible for the majority of the attenuation in September. On the right plots in the image for September, you can also see the anticipated attenuation derived using the French model.

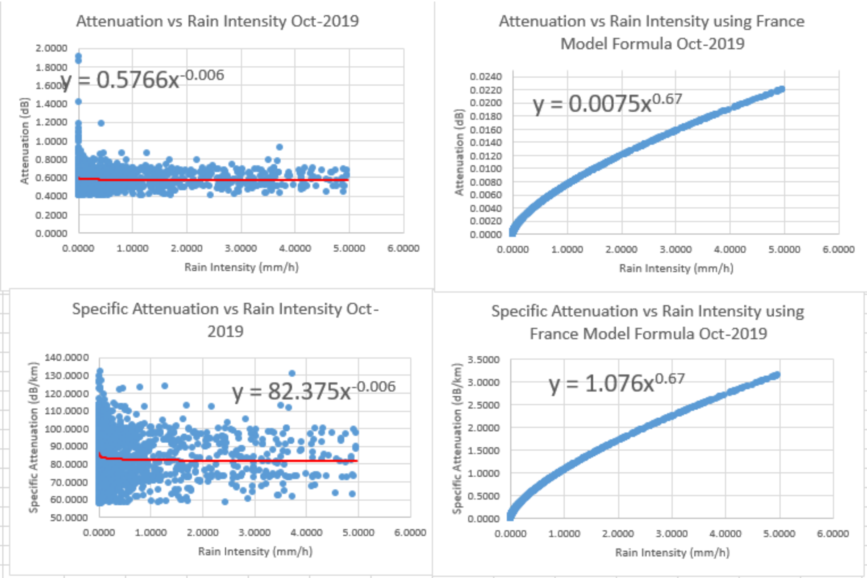

Figure 58: Specific Attenuation & Attenuation vs. Rain Intensity plots with French Model for October 2019

In October and November, it’s spring in South Africa, and it is one of the rainiest months of the year. Figures 58-59 show that there were more rain occurrences during these months than during the preceding ones. It was also noted before that the rainiest months of the year occurred during this time. For October the modelled rain attenuation equation in Durban, is $y = 82.375x^{-0.006}$, where y is the specific rain attenuation and x is the rain intensity. The $k\ and\ \alpha$ coefficients are 82.375 and -0.006, respectively. The modelled rain attenuation equation in Durban, for November, is $y = 84.479x^{0.0074}$, where y is the specific rain attenuation and x is the rain intensity. The $k\ and\ \alpha$ coefficients are 84.479 and 0.0074, respectively, as seen in Figure 59 below. During these month, most of the attenuation was due to rain, as they were the rainiest month in Durban during that time. Also the predicted attenuation obtained by using the French model can be seen on the right plots on the Figures.

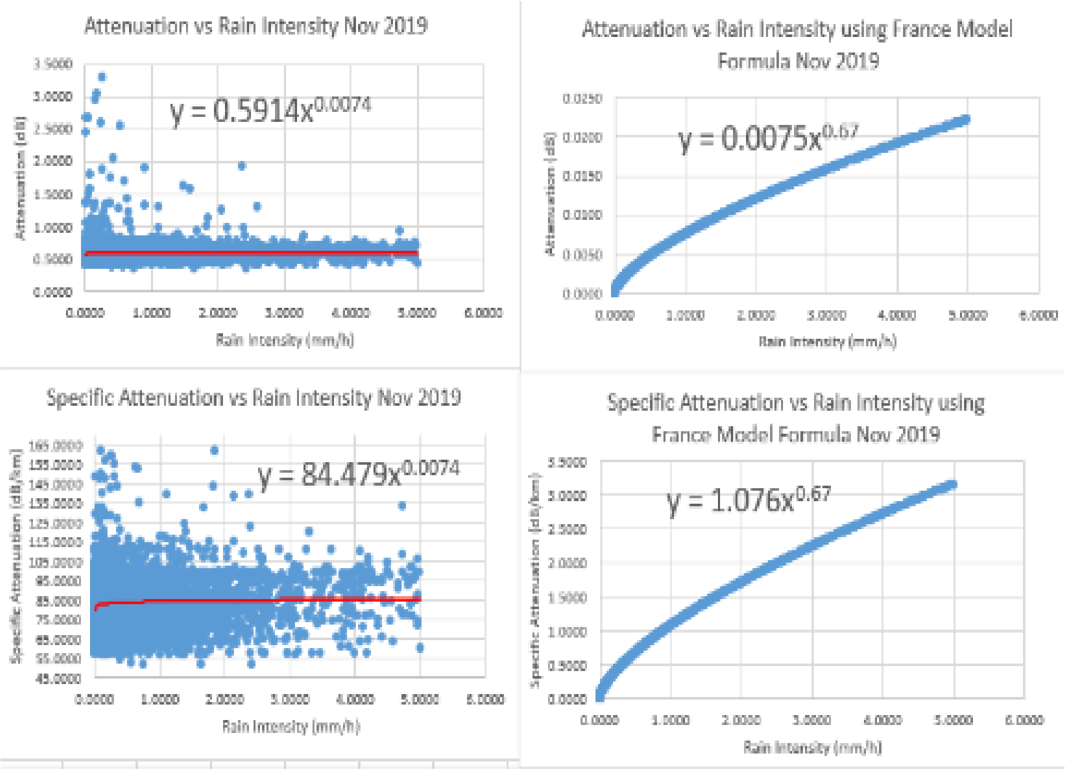

Figure 59: Specific Attenuation & Attenuation vs. Rain Intensity plots with French Model for November 2019

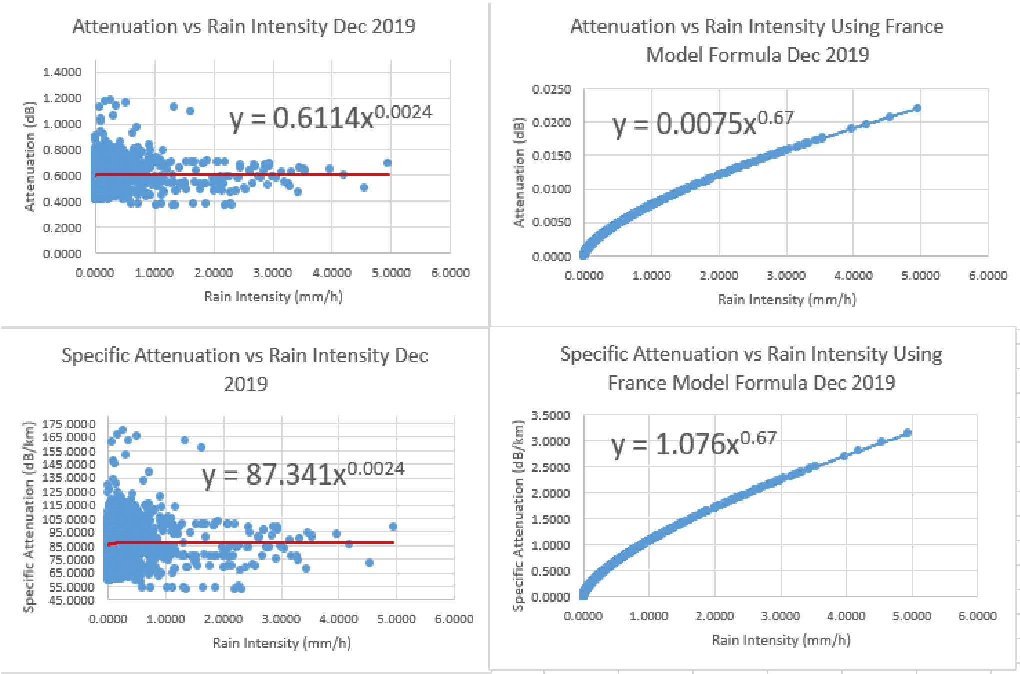

Figure 60: Specific Attenuation & Attenuation vs. Rain Intensity plots with French Model for December 2019

December and January are the last two months of the study period, which is spring in South Africa and one of the rainiest seasons. Summer is one of the rainiest seasons in South Africa, but it is also the sunniest season in Durban, with the majority of days being sunny rather than rainy. This is evident in Figures 60-61, particularly Figure 61, which reveals that there was very little rain in January. In addition, the modelled attenuation due to rain equation in Durban for December is $y = 87.341x^{0.0024}$, where y is the specific rain attenuation and x is the rain intensity. The k and α coefficients are 87.341 and -0.0024, respectively. For January, the modelled attenuation due to rain equation in Durban, is $y = 89.285x^{0.0224}$, where y is the specific rain attenuation and x is the rain intensity. The k and α coefficients are 89.285and 0.0224, respectively, as seen in Figure 61 below. It's fair to assume that all of the above-mentioned variables, such as rain, fog, and scintillation, contributed to the attenuation throughout these months. Scintillation might be the major culprit because there are more clear (sunny) days during this season. On the right plots in the images, you can observe the expected attenuation achieved using the French model.

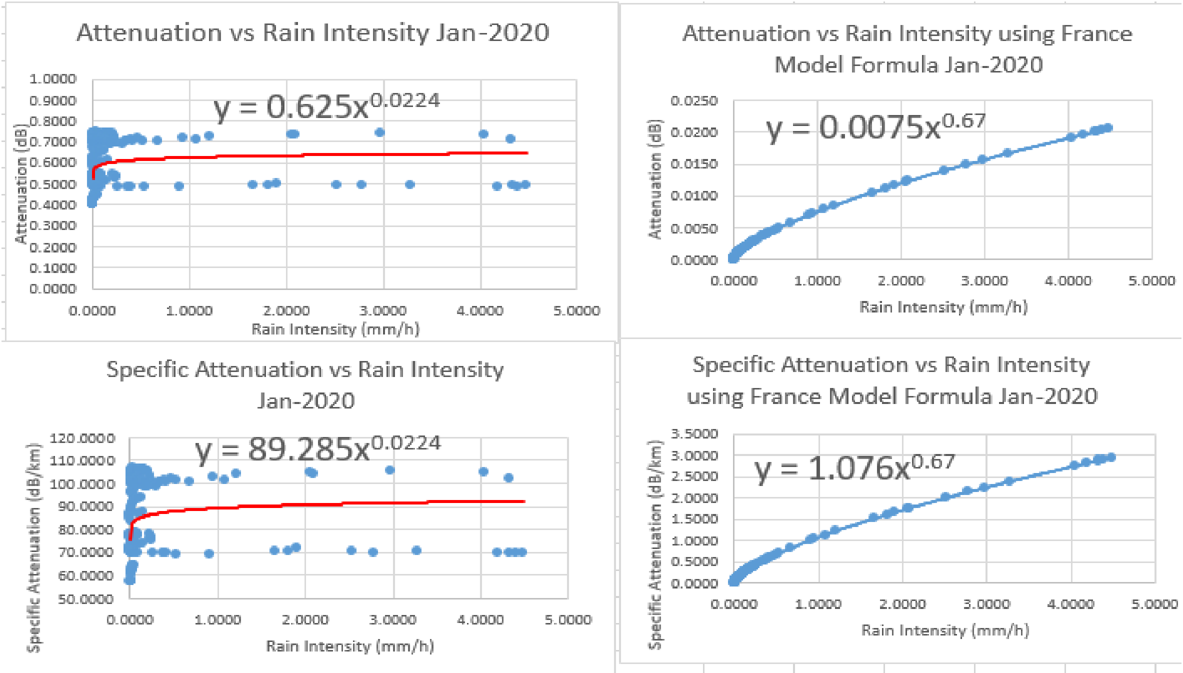

Figure 61: Specific Attenuation & Attenuation vs. Rain Intensity plots with French Model for January 2020

5.7 Summary

The different climate variations of South Africa were elaborated, which are based on four seasonal cycles: spring, summer, autumn, and winter. The samples utilized for this measurement period were also broken down into numbers and divided into categories. The rain intensity time series and the equivalent optical received signal time series of days that went through various rainfall kinds, demonstrating the transition from drizzle to thunderstorm, were also examined and discussed. The relationship between rain intensity and raindrop diameter was also analysed. It was shown that the rain intensity is not the only factor that has an effect on rain attenuation, other factors as well such as fog, scintillation, the raindrop diameter and the alignment, they have an impact on the attenuation of rain. From the measured attenuation in all the figures, one sees a constant value of about 0.62 dB over the link. The measured attenuation is seen to be practically independent of the rain rate. This implies that there is a high possibility of the presence of fog alongside the rain/drizzle. Indeed, from the work of Mohale et al [84], it is shown that of all the cities in South Africa, Durban has the lowest visibility, a parameter which is closely related to the fogginess.

The specific attenuation was calculated in this chapter. Then the relationship between attenuation and specific rain attenuation due to rain intensity. Using the French model, a comparison was made between the obtained results and results from other nations to see if they were in agreement with other existing models. The modelled and predicted attenuation for Durban were shown (for drizzle range). It was also mentioned that the French FSO attenuation model is only applicable to drizzle rain. While the obtained results when using the power law follow the same rising trend as the French models, the attenuation values plotted for Durban are significantly higher than those plotted for France. The distance between the transceivers may also contribute to the significant attenuation loss. The transceivers are too closely together, which might increase the effect. Due to a lack of material or cables to link the transceivers to the computer for data monitoring and logging, the distance between the transceivers was limited to 7 meters throughout the experiment. This calls for further investigation, as there seems to be an additional underlying attenuation factor in the Durban case alongside the rain attenuation for FSO links. This is thus the subject of further work.

CHAPTER 6

CONCLUSION AND FUTURE WORKS

6.1 Conclusions

An in-depth performance investigation of the OWCS, as well as rain attenuation modelling and prediction for OWC link performance for Durban, South Africa, was carried out in this thesis. To accomplish all of this, a thorough understanding of OWCS was required, including application areas, eye safety, and standards. An overview of Optical power meter was also done, because the power meter was used to get the attenuation of rain, for the report analysis.

With the transceivers separated by a fixed distance of 7 meters, suitable mathematics had to be used to determine the system's link margin. The power meter was used to record the signal power level in dBm. The power meter was quite helpful in determining the impact of rain on the received signal. It was also established that the highest power received value was obtained during clear weather, while the lowest value was reported during heavy rain.

The rain intensity was also recorded using the disdrometer, and the relationship between the rain intensity and the optical signal received was investigated using the synchronized time series, as seen in Figure 32-42. The relationship between Specific attenuation in dB/km and rain intensity in mm/h, as well as the relationship between Attenuation in dB and rain intensity, was investigated. As seen in some of the plotted graphs in Figures 32 to 42, the received signal is inversely proportional to the intensity of the rain. The attenuation and specific attenuation due to rain increases when the signal received decreases, as shown in equations (46) and (47), and the rain intensity increases, as seen in Figures 46-51. Rain intensity data from the disdrometer was recorded and plotted against attenuation values from the power meter at the same time. It was also discovered that there is a linear relationship between raindrop diameter and rain intensity, with an increase in raindrop diameter resulting in a linear rise in rain intensity.

The empirical method was used to investigate the relationship between attenuation and specific attenuation due to rain intensity, with all data done at an optical wavelength of 850nm. A trend-line was drawn from the plotted data to highlight the relationship between attenuation and rain intensity. This helped to show that as the rain intensity increases, there is also an increase in specific attenuation. The $k\ and\ \alpha$ coefficients for Durban (Glenwood area) were also found. The obtained results were also compared to models from other countries, which revealed that the obtained results were in correlation with those of other models.

The received optical signal time series and rain intensity time series plots show that there is practically constant attenuation in the FSO link under drizzle rainfall regime in Durban, according to a study. The attenuation due to rain is almost two orders of magnitude higher than the French model prediction. This shows that during a drizzle rain event, attenuation is not solely dependent on rain intensity, implying that other parameters such as fog and scintillation, play an active role during a rain event in Durban. This therefore calls for further analysis of these meteorological influences.

6.2 Future Works

The thesis's major goal, as mentioned in the first chapter, has been accomplished. However, further research is needed to determine the impact of other weather variables, such as fog and snow, on the received optical signal, which leads to it being attenuated. However, because snow is uncommon in Durban, the study might be conducted in other parts of South Africa where snow is feasible.

With rain having such an influence on attenuation, it's logical to assume that fog has a higher impact, especially because research indicates that the study location gets a lot of fog, but this has to be confirmed. Fog might be the topic of future research to test the assumptions expressed in the thesis. Also, the distance between the transceivers may be expanded by moving the experiment to other buildings that are hundreds of meters apart. This will need extra funds in order to obtain the necessary equipment in order to achieve better outcomes. The use of a weather station can also be very useful in validating the above-mentioned wind conclusion.

6.3 Summary of Study

Table 11: Summary of key findings

Authors and Supervisors	Study Aim	Study Type/Information	Main Findings and Conclusions	Study Strength/Limitations
Mr Sabelo Qiniso Buthelezi; Prof. Thomas J.O Afullo; Dr. Modisa Mosalaosi	Theoretically determine rain attenuation parameters for optical signals based on various rainfall measurements for the city of Durban, in South Africa. Evaluate the analytical performance of the proposed model, which in this case is the power law model, under rainy conditions, alongside other established models. Establish a suitable link budget analysis for OWC links to be deployed in Durban using the results and the equipment available.	Lab research work using a disdrometer to obtain the rain intensity, and a power meter to log the received signal power level every 30 seconds to evaluate the influence of rain on the signal transmitted.	Rain does influence attenuating the received signal; however, the results reveal that it does not have a significant effect. The measured attenuation shows that the attenuation was constant all over the link. This then leads to an assumption that the observed attenuation is less affected by rain intensity, which means there's a high possibility of fog along with the rainfall. Indeed, according to the research, Durban has the lowest visibility of all the cities in South Africa, a factor that is closely linked to fogginess. The thesis's major goal has been accomplished; however, further research is needed to determine the impact of other weather variables on the received optical signal, which leads to it being attenuated. Rain proved to have a big influence on attenuation, the assumption that fog has a higher impact is reasonable, especially because research indicates that the study location gets a lot of fog, but this	The transceivers were just 7 meters apart due to a lack of funding for better equipment and longer cables to link the transceivers to the computer for data monitoring and logging, yet this allowed for accurate alignment because the transceivers were closer to each other, and there was a technique to anticipate for longer distances.

			has to be confirmed. Also, for better outcomes, the distance between the transceivers may be expanded by moving the experiment to other buildings that are hundreds of meters apart. There are extremely high attenuation values for Durban compared to the French model, which thus calls for further investigation to provide the optimum model that can accurately predict these effects.	

References

[1] Z. Ghassemlooy, W. Popoola, and S. Rajbhandari, Optical wireless communications: system and channel modelling with Matlab, CRC press, 2017.

[2] A. Basahel, W.i Al-Khateeb, Md. R. Islam, K. Al-Khateeb, A.Z. Suriza, "Availability Analysis of Terrestrial Free Space Optical Link Under the Impact of Rain Condition," *5th International Conference on Computer & Communication Engineering,* pp. 169-172, 2014.

[3] A. Basahel, M. R. Islam, A.Z. Suriza, and M. H.i Habebi, "Effect of Rain & Haze on Availability of Terrestrial Free Space Optical Link Under Tropical Weather Conditions," *2016 International Conference on Computer & Communication Engineering,* pp. 378-381, 2016.

[4] A. Basahel, M. R. Islam, A.Z. Suriza, M. H. Habaebi, "Availability analysis of free-space-optical links based on rain rate and visibility statistics from tropical a climate," *Optik,* vol. 127, pp. 10316-10321, 2016.

[5] S. A. Al-Gailan, A. Mohammad, U. U. Sheikh, R. Q. Shaddad, "Determination of rain attenuation parameters for free space optical link in tropical rain," *Optic,* vol. 125, pp. 1575-1578, 2014.

[6] V. Brazda, V.r Scheijbal, and O. Fiser, "Rain Impact on FSO Link Attenuation Based on Theory and Measurement," *6th European Conference on Antennas and Propagation (EUCAP),* pp. 1239-1243, 2012.

[7] U. A. Korai, L. Luini, and R. Nebuloni, "Model for the Prediction of Rain Attenuation Affecting Free Space Optical Links," *MDPI electronics,* vol. 7, no. 407, p. 3, 2018.

[8] A.A Alonge and T.J.O Afullo, "CORRELATION OF RAIN DROPSIZE DISTRIBUTION WITH RAIN RATE DERIVED FROM DISDROMETERS AND RAIN GAUGE NETWORKS IN SOUTHERN AFRICA," *MSc Thesis, UKZN,* 2011.

[9] "South African Government Geography and Climate," EXPLORE GOV.ZA, 2021. [Online]. Available: https://www.gov.za/about-sa/geography-and-climate#. [Accessed 12 March 2021].

[10] A. Z. Suriza, M. R. Islam, W. Al-Khatteb and A. W. Naji, "ANALYSIS OF RAIN EFFECTS ON TERRESTRIAL FREE SPACE OPTICS BASED ON DATA MEASURED IN TROPICAL CLIMATE," *IIUM Engineering Journal,* vol. 12, no. 5, pp. 45-51, 2011.

[11] I.-R. R. P838-3, "Specific Attenuation Model for Rain for use in Prediction Methods," in *International Telecommunication Union, Radiocommunication*, Geneva, 2005.

[12] T. Carbonneau, D. Wisley, "Opportunities and challenges for optical wireless; the competitive advantage of free space telecommunications links in today's crowded market place," in *SPIE Conference on Optical Wireless Communications*, 1998.

[13] M. A. Bakar, "Optimization of FSO System in Tropical Weather using Multiple Beams," *IEEE 5th International Conference on Photonics (ICP),*, pp. 109-112, 2014.

[14] M. Radhashyam, "THE WETTEST PLACE ON THE EARTH," in *106th Indian Science Congress*, Lovely Professional University Phagwara Punjab, March 2019.

[15] I.-R. R. P.838-3, "Specific attenuation model for rain for use in prediction methods," in *Radiocommunication Sector*, Geneva, 2005.

[16] S. P. Maswikaneng, P. A. Owolawi, S. O. Ojo, Z. Mahlobongwane, and M. I. Mphahlele, "Climatic Effects on Free Space Optics Link: South African Climate," *International Conference on Intelligent and Innovative Computing Applications (ICONIC),* 2018.

[17] T. Mohamed, B. Mahmoud, A. Adam, "Analysis of Rain Effects on Free Space Optics Based on Data Measured in the Libyan Climate," *nternational Journal of Information and Electronics Engineering*, vol. 4, 2014.

[18] O.e O. Kolawole, T. J.O. Afullo, and P A. Owolawi, "PERFORMANCE ANALYSIS OF OPTICAL WIRELESS COMMUNICATION SYSTEMS IN A WARM-SUMMER MEDITERRANEAN CLIMATIC REGION," *IEEE,* p. 6, 2017.

[19] A. Bekkali, C. B. Naila, K. Kazaura, K. Wakamori, and M. Matsumoto, ""Transmission analysis of OFDM-based wireless services over turbulent radio-on-FSO links modeled by gamma–gamma distribution," *IEEE Photonics Journal,* vol. 2, pp. 510-520, 2010.

[20] N. H. M. Noor, A. Naji, and W. Al-Khateeb, "Theoretical analysis of multiple transmitters/receivers on the performance of free space optics (FSO) link," *Space Science and Communication (IconSpace), 2011 IEEE International Conference,* pp. 291-295, 2011.

[21] X. Wu, P. Liu, and M. Matsumoto, "A study on atmospheric turbulence effects in full-optical free-space communication systems," *Wireless Communications Networking and Mobile Computing (WiCOM), 2010 6th International Conference,* pp. 1-5, 2010.

[22] S. A. Zabidi, M. R. Islam, W. Al Khateeb, and A. W. Naji, "Investigating of rain attenuation impact on free space optics propagation in tropical region," *Mechatronics (ICOM), 2011 4th International Conference,* pp. 1-6, 2011.

[23] W. O. Popoola, Subcarrier intensity modulated free-space optical communication systems, Northumbria University, 2009.

[24] M. Gregory and S. Badri-Hoeher, "Characterization of maritime RF/FSO channel," *Space Optical Systems and Applications (ICSOS), 2011 International Conference,* pp. 21-27, 2011.

[25] M. Niu, J. Cheng, and J. F. Holzman, "Diversity reception for coherent free-space optical communications over K-distributed atmospheric turbulence channels," *Wireless Communications and Networking Conference (WCNC), 2010 IEEE*, pp. 1-6, 2010.

[26] T. Yamashita, M. Morita, M. Shimizu, D. Eto, K. Shiratama, and S. Murata, "The new tracking control system for Free-Space Optical Communications," *Space Optical Systems and Applications (ICSOS), 2011 International Conference*, pp. 122-131, 2011.

[27] S. Bloom, E. Korevaar, J. Schuster, and H. Willebrand, ""Understanding the performance of free-space optics [Invited]," *Journal of optical Networking*, vol. 2, pp. 178-200, 2003.

[28] P. J. M. v. d. Slot, "IEC 60825-1 Safety of laser products - Part 1: Equipment classification, requirements and user's guide," *INTERNATIONAL STANDARDS*, 2001.

[29] O. Bouchet, H. Sizun, C. Boisrobert, and F. De Fornel, "Free-space optics: propagation and communication," *John Wiley & Sons*, vol. 91, 2010.

[30] I. E. Commission, "IEC 60825-1 Safety of laser products-part 1: equipment classification and, requirements," *Geneva, Switzerland: International Electrotechnical Commission*, 2007.

[31] Willebrand and B. S. Ghuman, Free space optics: enabling optical connectivity in today's networks, SAMS publishing, 2002.

[32] R. M. Gagliardi and S. Karp, Optical communications, New York: Wiley-Interscience, 1976.

[33] D. Killinger, "Free space optics for laser communication through the air," *Optics and Photonics News*, vol. 13, pp. 36-42, 2002.

[34] W. K.Pratt, "Laser Communication Systems," 1969.

[35] S. Betti, G. De Marchis, and E. Iannone, "Coherent optical communications systems," *Wiley-Interscience*, 1995.

[36] J. S. Seybold, "Handbook on Introduction to RF Propagation," New York, John Wiley and Sons, 2005, pp. 218-245.

[37] R. K. Crane, "Propagation Handbook for Wireless Communication System Design," New York, CRC Press, 2003, pp. 35-70.

[38] D. M. Pozar, in *Handbook on Microwave Engineering, Second Edition*, New York, John Wiley and Sons Inc., 1998, p. 6.

[39] G.O. Ajayi, S. Feng, S. M. Radicella, B. M. Reddy, in *Handbook on Radiopropagation Related to Satellite Communications in Tropical and Subtropical Countries*, Trieste, ICTP, 1996, pp. 7-14.

[40] C. Salema, in *Microwave Radio Links*, New York, John Wiley and Sons, 2003, pp. 66-67.

[41] V. Pastoriza, A. Núñec, P. Mariño, F. P. Fontán and U. C. Fiebi, "Raincell identification and Modeling for propagation studies from weather radar images," *IEEE Antennas Propagations,* vol. 52, no. 5, 2010.

[42] J. S. Mandeep, and J. E. Allnut, "Rain attenuation predictions at Ku-band in South East Asia countries," *Progress in Electromagnetic Research,* pp. 65-74, 2007.

[43] V. Ramachandran And V. Kumar, "Modified rain attenuation model for tropical regions for KU band signals," *Int. J. Satell. Commun. Network,* vol. 25, pp. 53-67, 2007.

[44] C. Capsoni, F. Fedi, C. Magstroni, A. Paraboni and A. Pawlina, "Data and theory for a new model of the horizontal structure of rain cells for propagation applications," *Raido Sci.*, vol. 22, no. 3, pp. 395-404, 1987.

[45] M. Sadiku, in *Numerical Techniques in Electromagnetics, 2nd edition*, CRC press, 2000, pp. 96-103.

[46] P. Owalawi, "Characteristics of Rain at Microwave and Millimetric Bands for Terrestrial and Satellite Links Attenuation in South Africa and Surrounding Islands," *Ph.D thesis University of KwaZulu-Natal,* 2010.

[47] L. D. Emiliani, L. Luini and C. Capsoni, "Analysis and parameterization of methodologies for the conversion of rain-rate cumulative distributions from various integration times to one minute," *IEEE Antennas Propagat. Mag.*, vol. 51, no. 3, pp. 70-84, 2009.

[48] M. J. Bartholomew, Disdrometer and tipping bucket raingauge handbook, DOE/SC-ARM/TR-079, ARM Climate Research Facility.

[49] M. Saikia, M. Devi, A. K. Barbara and H. K. Sarmah, "Raindrop size distribution profile by laser disdrometer and rain attenuation of centimeter radio waves," *Indian Journal of radio and space physics,* vol. 38, pp. 80-85, 2009.

[50] G. Zhang, Q. Cao, M. Xue, P. Chilson, M. Morris and R. Palmer, in *A field experiment to study rain microphysics using video disdrometers, profiler, and polarimetric S- and X-band radars*, New Orleans, Symp. on Recent Developments in Atmos. Application of Radar and Lidar, 2008.

[51] J. O. Laws and D. A. Parsons, "The Relation of raindrop-size to intensity," *Trans. Amer. Geophys. Union,* vol. 24, pp. 452-460, 1943.

[52] R. L. Olsen, D. V. Rogers, D. B. Hodge, "The aR^b Relation in the calculation of rain attenuation," *IEEE Trans. Antennas Propag.*, vol. 26, no. 2, pp. 547-556, 1978.

[53] F. Moupfouma, "Improvement of a Rain Attenuation Prediction Method for Terrestrial Microwave Links," *IEEE Trans. Antennas Propag.*, vol. 32, pp. 1368-1372, 1984.

[54] A. Maitra, "Rain Attenuation Modelling From Measurements of Rain Drop Size Distribution in the Indian Region," *IEEE Antennas Wireless Propag. Lett*, vol. 3, pp. 180-181, 2004.

[55] R. K. Crane, "Prediction of Attenuation by Rain," *IEEE Trans. On Comm.*, vol. 28, no. 9, pp. 1717-1733, 1980.

[56] G. O. Ajayiand E. B. C. Ofoche, "Some Tropical Rainfall Rate Characteristics at Ile-Ife for Microwave and Millimeter Wave Application," *J. of Climate and Applied Meteor.*, vol. 23, pp. 562-567, 1983.

[57] I.-R. R. P.530-13, "Propagation data and prediction methods for the design of terrestrial line-of-sight systems," in *Radiocommunication sector*, Geneva, 2009.

[58] R. K. Crane, in *Electromagnetic Wave Propagation Through Rain*, New York, John Wiley and Sons Inc., 1996, pp. 1-4, 39-40.

[59] 2. ITU-R Recommendation P.837-1, "Characteristics of Precipitation for Propagation Modelling," in *International Telecommunication Union, Radiocommunication Sector*, Geneva, 2008.

[60] F. Moupfouma, "More about rainfall rates and their prediction for radio systems engineering," *IEE Proc.*, vol. 134, no. 6, pp. 527-537, 1987a December.

[61] J. S. Ojo, M. O. Ajewole and S. K. Sarkar, "Rain Rate and Rain Attenuation Prediction for Satellite Communication in Ku and Ka Bands over Nigeria," *Prog. in Electromagnetics Research (PIER)*, vol. 5, pp. 207-233, 2008.

[62] F. Moupfouma, "Empirical model for rainfall rate distribution," *Electron. Lett.*, vol. 18, pp. 460-461, 1982.

[63] H. J. Weber and G. B. Arfken, in *Essential Mathematical Methods for Physicists*, San Diego, Academic Press, 2003, pp. 523-544.

[64] T. T. Soong, in *Fundamentals of Probability and Statistics for Engineers*, Chichester, John Wiley, 2004, pp. 209-219, 235.

[65] P. A. Owolawi, "Rain rate probability density evaluation and mapping for the estimation of rain attenuation in South Africa and surrounding Islands," *Progress in Electromagnetic Research,* vol. 112, pp. 155-181, 2011.

[66] E. Kreyszig, in *Advanced Engineering Mathematics 9th Edition*, John Wiley and Sons, 2006, pp. 1046-1047.

[67] H. C. van der Hulst, Light scattering by small particles, New York: John Wiley and Sons Inc., 1957.

[68] N. H. H. Khamis, J. Din and T. A. Rahman, "Derivation of path reduction factor from the Malaysian meterological radar data," *IEEE Antennas Propag.*, pp. 207-210, 2005.

[69] P. Sharma, S. I. Hudiara and M. L. Singh, "Estimation of path length reduction factor by using one year attenuation statistics over a line of sight link operating at 28.75 GHz in Amristar INDIA," *J. Infrared Milli. Terahz. Waves,*, vol. 32, pp. 137-142, 2011.

[70] Garcia-Lopez, J. A. and J. Peiro, "Simple rain-attenuation prediction technique for terrestrial radio links," *Electronic Letters,* vol. 19, no. 21, pp. 444-448, 1983.

[71] Perez-Garcia, N. A. and L. A. R. da Silva Mello, "Improved method for prediction of rain attenuation in terrestrial links," *Electronic Letters*, vol. 40, no. 11, pp. 683-684, 2004.

[72] E. Britannica, "Map of South Africa," Student and Home Edition: software, 2009.

[73] November 2011. [Online]. Available: www. proseo.co.za.

[74] M. O. Fashuyi, P. A. Owolawi and T. J. O. Afullo, "Rainfall rate modelling for LoS radio systems in South Africa," *Trans. of South African Inst. of Elect. Engineers (SAIEE),* vol. 97, pp. 74-81, 2006.

[75] M. O. Odedina and T. J. O. Afullo, "Characteristics of seasonal attenuation and fading for line-of-sight links in South Africa," *Proc. of SATNAC,* pp. 203-208, 2008.

[76] Haln, "Optical Power Monitor Operational Manual, 2018," [Online]. Available: https://www.thorlabs.com/software/MUC/OPM/v1.1/TL_OPM_V1.1_web-secured.pdf . [Accessed 15 October 2020].

[77] "DISDROMETER RD-80, User Guide for DISDRODATA 4.0," Distromet ltd, 15 January 2018. [Online]. Available: http://www.ictinternational.com/content/uploads/2018/07/Disdrodata-User-Guide-4.0-January-2018.pdf. [Accessed 18 April 2021].

[78] D. Sumbiri, "Microwave and Millimetre Radio Wave Propagation Modelling for Terrestrial Line-of-Sight Links in Central," *In fulfilment of the Degree of Doctor of Philosophy in Electronic Engineering, College of Agriculture, Engineering and Science, University of KwaZulu-Natal, Durban,* June 2018.

[79] [Online]. Available: https://weather-and-climate.com/average-monthly-Rainfall-Temperature-Sunshine,durban,South-Africa. [Accessed 25 October 2020].

[80] M. O. Fashuyi, P. A. Owolawi and T. J. O. Afullo, "Rainfall rate modelling for LoS radio," *Trans. of South African Institution of Electrical Engineers (SAIEE)*, vol. 97, pp. 74-84.

[81] A. T. G. & C. KG,, "Laser Precipitation Monitor 5.4110.xx.x00 V2.5x STD," *Gottingen: Thies CLIMA,* 2011.

[82] A. Zabidi, Suriza, M. R. Islam, Wajdi, A.K. Naji, "Effects of rain intensity variation on rain attenuation prediction for Free Space Optics (FSO) links," *2012 International Conference on Computer and Communication Engineering, ICCCE 2012*, 2012.

[83] M. J. Leitao and P. A. Watson , "Method for prediction of attenuation on earth-space links based on radar measurements of the physical structure of rainfall," *IEEE Proceedings F (Communications, Radar and Signal Processing),* vol. 133, no. 4, pp. 429-440, 1986.

[84] U. Korai, L. Luini and R. Nebuloni, "Model for the Prediction of Rain Attenuation Affecting Free Space Optical Link," *Electronics*, vol. 7, p. 407, 2018.

[85] [Online]. Available: https://en.wikipedia.org/wiki/Weather_station. [Accessed 30 January 2019].

[86] Ahmad Zabidi, Suriza & Islam, Md & Wajdi, A.K. & Naji, A.W, "Proposed parameters of specific rain attenuation prediction for Free Space Optics link operating in tropical region," *ournal of Atmospheric and Solar-Terrestrial Physics*, vol. 94, pp. 93-99, 2013.

[87] V. d. Hulst, Light Scattering by Small particles, New York: J.Wiley pub, 1957.

[88] P. Owolawi, "Rainfall rate and rain drop size distribution models for line-of-sight millimetric systems in South Africa," *MSc Dissertation, University of KwaZulu-Natal*, 2006.

[89] Moupfouma, F. and L. Martin, "Point Rainfall Rate Cumulative Distribution Function valid at various Locations," *Electron. Letters*, vol. 29, pp. 1503-1505, 1993.

APPENDICES

APPENDIX A-1

The International Telecommunication Union (ITU) defines frequency bands for terrestrial, satellite, and personal area networks, some of which are part of a larger spectrum. The following are the possible frequency bands and their corresponding designations:

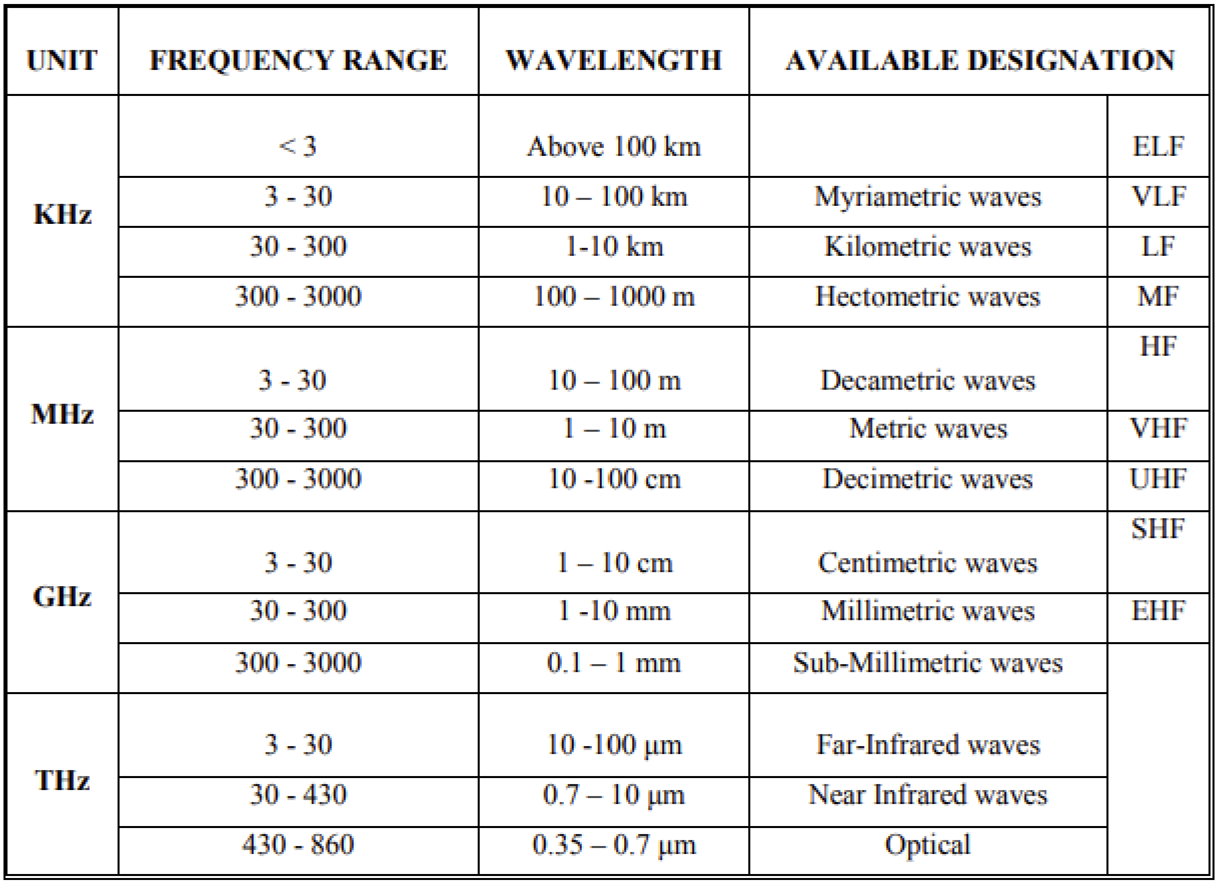

UNIT	FREQUENCY RANGE	WAVELENGTH	AVAILABLE DESIGNATION	
KHz	< 3	Above 100 km		ELF
	3 - 30	10 – 100 km	Myriametric waves	VLF
	30 - 300	1-10 km	Kilometric waves	LF
	300 - 3000	100 – 1000 m	Hectometric waves	MF
MHz	3 - 30	10 – 100 m	Decametric waves	HF
	30 - 300	1 – 10 m	Metric waves	VHF
	300 - 3000	10 -100 cm	Decimetric waves	UHF
GHz	3 - 30	1 – 10 cm	Centimetric waves	SHF
	30 - 300	1 -10 mm	Millimetric waves	EHF
	300 - 3000	0.1 – 1 mm	Sub-Millimetric waves	
THz	3 - 30	10 -100 µm	Far-Infrared waves	
	30 - 430	0.7 – 10 µm	Near Infrared waves	
	430 - 860	0.35 – 0.7 µm	Optical	

APPENDIX A-2

The specific attenuation at various frequencies may be predicted using the values of k and, as well as the R0.01 of a locale, according to ITU-R Guideline P. 838-3. As a result, the particular attenuation is denoted by:

$$A_s = kR^{\alpha}{}_{0.01}$$

For horizontal and vertical polarization modes, the suggested values of k and are listed below:

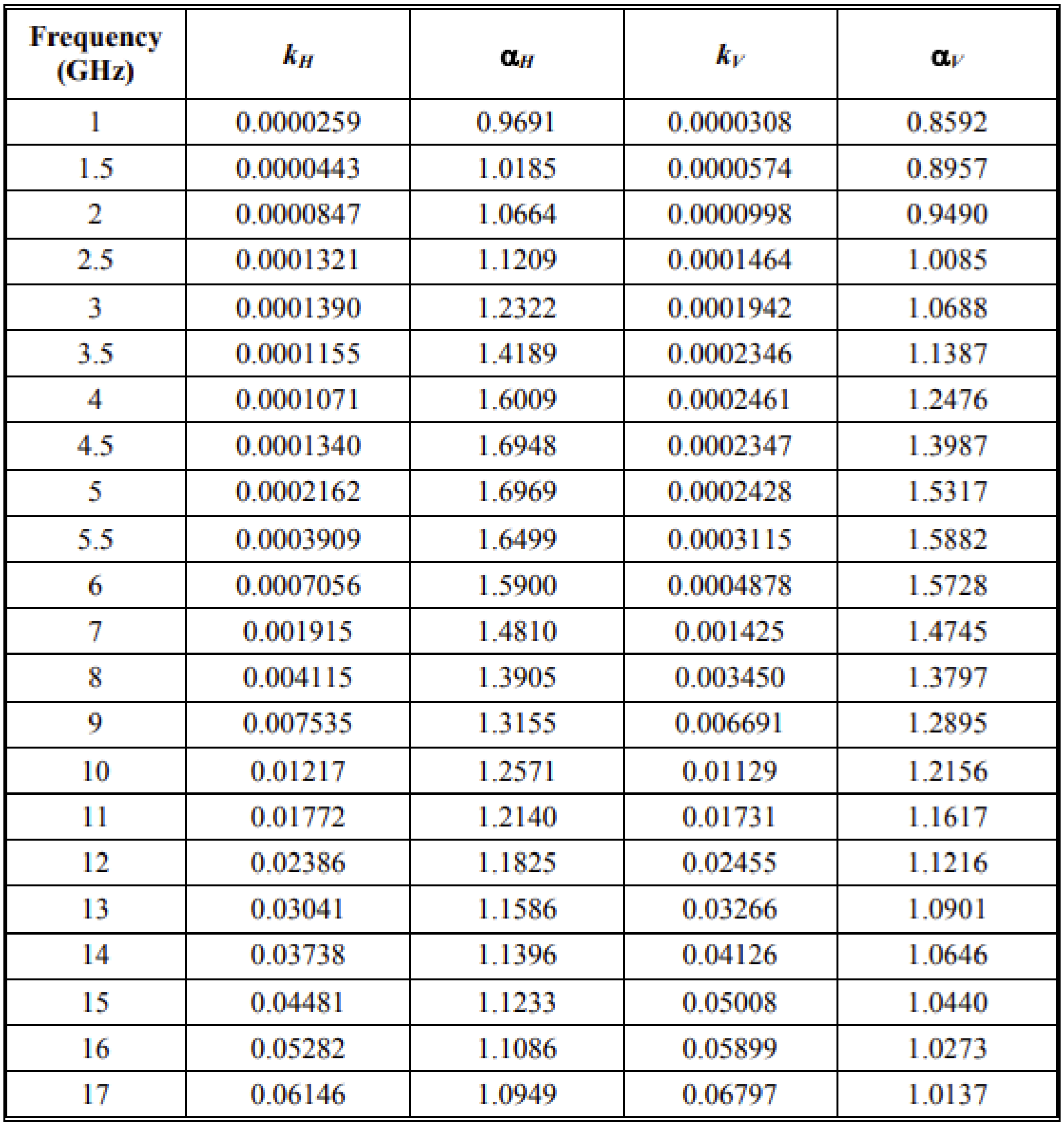

Frequency (GHz)	k_H	α_H	k_V	α_V
1	0.0000259	0.9691	0.0000308	0.8592
1.5	0.0000443	1.0185	0.0000574	0.8957
2	0.0000847	1.0664	0.0000998	0.9490
2.5	0.0001321	1.1209	0.0001464	1.0085
3	0.0001390	1.2322	0.0001942	1.0688
3.5	0.0001155	1.4189	0.0002346	1.1387
4	0.0001071	1.6009	0.0002461	1.2476
4.5	0.0001340	1.6948	0.0002347	1.3987
5	0.0002162	1.6969	0.0002428	1.5317
5.5	0.0003909	1.6499	0.0003115	1.5882
6	0.0007056	1.5900	0.0004878	1.5728
7	0.001915	1.4810	0.001425	1.4745
8	0.004115	1.3905	0.003450	1.3797
9	0.007535	1.3155	0.006691	1.2895
10	0.01217	1.2571	0.01129	1.2156
11	0.01772	1.2140	0.01731	1.1617
12	0.02386	1.1825	0.02455	1.1216
13	0.03041	1.1586	0.03266	1.0901
14	0.03738	1.1396	0.04126	1.0646
15	0.04481	1.1233	0.05008	1.0440
16	0.05282	1.1086	0.05899	1.0273
17	0.06146	1.0949	0.06797	1.0137

Frequency (GHz)	k_H	α_H	k_V	α_V
18	0.07078	1.0818	0.07708	1.0025
19	0.08084	1.0691	0.08642	0.9930
20	0.09164	1.0568	0.09611	0.9847
21	0.1032	1.0447	0.1063	0.9771
22	0.1155	1.0329	0.1170	0.9700
23	0.1286	1.0214	0.1284	0.9630
24	0.1425	1.0101	0.1404	0.9561
25	0.1571	0.9991	0.1533	0.9491
26	0.1724	0.9884	0.1669	0.9421
27	0.1884	0.9780	0.1813	0.9349
28	0.2051	0.9679	0.1964	0.9277
29	0.2224	0.9580	0.2124	0.9203
30	0.2403	0.9485	0.2291	0.9129
31	0.2588	0.9392	0.2465	0.9055
32	0.2778	0.9302	0.2646	0.8981
33	0.2972	0.9214	0.2833	0.8907
34	0.3171	0.9129	0.3026	0.8834
35	0.3374	0.9047	0.3224	0.8761
36	0.3580	0.8967	0.3427	0.8690
37	0.3789	0.8890	0.3633	0.8621
38	0.4001	0.8816	0.3844	0.8552
39	0.4215	0.8743	0.4058	0.8486
40	0.4431	0.8673	0.4274	0.8421
41	0.4647	0.8605	0.4492	0.8357
42	0.4865	0.8539	0.4712	0.8296
43	0.5084	0.8476	0.4932	0.8236
44	0.5302	0.8414	0.5153	0.8179
45	0.5521	0.8355	0.5375	0.8123
46	0.5738	0.8297	0.5596	0.8069
47	0.5956	0.8241	0.5817	0.8017
48	0.6172	0.8187	0.6037	0.7967
49	0.6386	0.8134	0.6255	0.7918
50	0.6600	0.8084	0.6472	0.7871
51	0.6811	0.8034	0.6687	0.7826
52	0.7020	0.7987	0.6901	0.7783

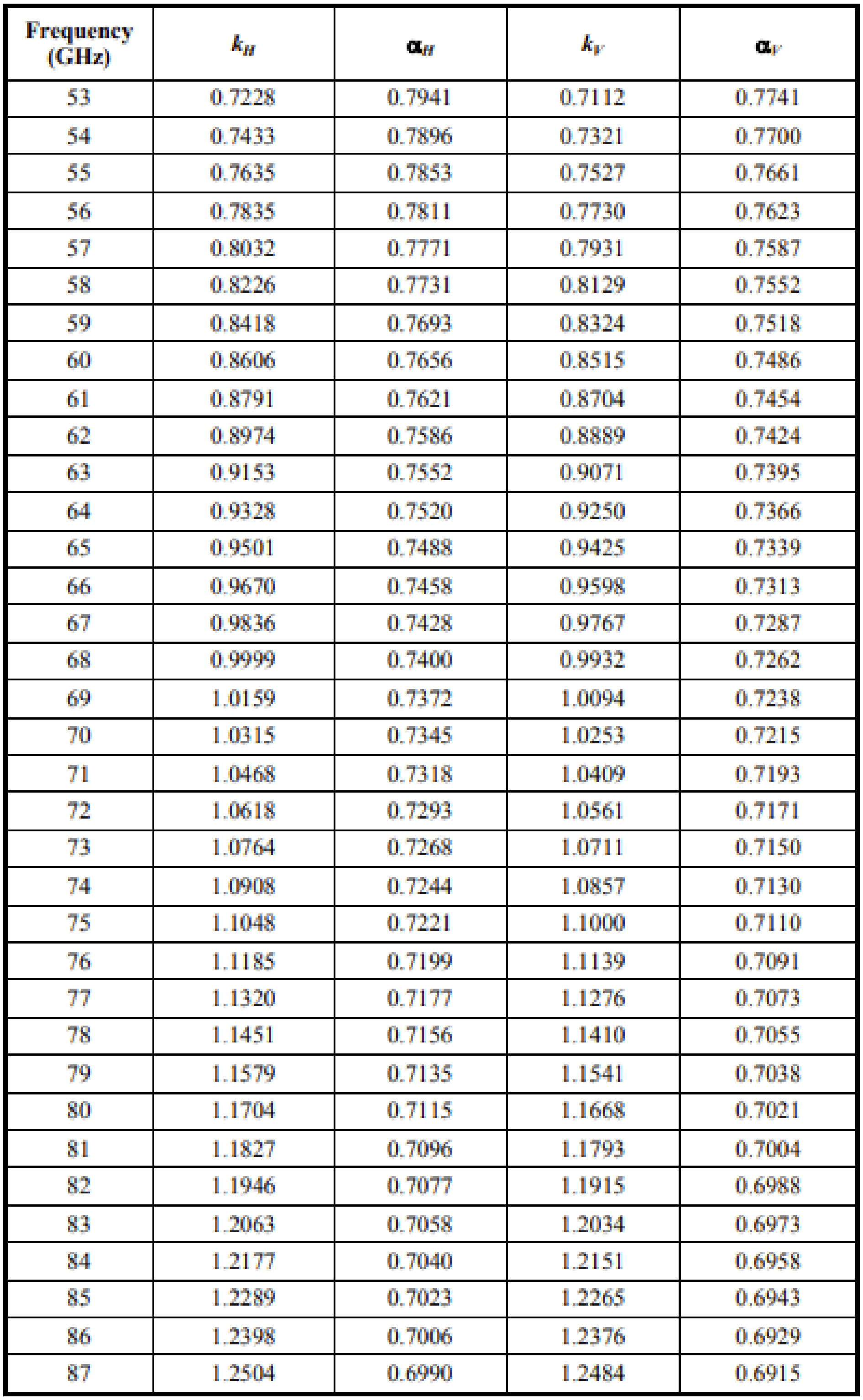

Frequency (GHz)	k_H	α_H	k_V	α_V
53	0.7228	0.7941	0.7112	0.7741
54	0.7433	0.7896	0.7321	0.7700
55	0.7635	0.7853	0.7527	0.7661
56	0.7835	0.7811	0.7730	0.7623
57	0.8032	0.7771	0.7931	0.7587
58	0.8226	0.7731	0.8129	0.7552
59	0.8418	0.7693	0.8324	0.7518
60	0.8606	0.7656	0.8515	0.7486
61	0.8791	0.7621	0.8704	0.7454
62	0.8974	0.7586	0.8889	0.7424
63	0.9153	0.7552	0.9071	0.7395
64	0.9328	0.7520	0.9250	0.7366
65	0.9501	0.7488	0.9425	0.7339
66	0.9670	0.7458	0.9598	0.7313
67	0.9836	0.7428	0.9767	0.7287
68	0.9999	0.7400	0.9932	0.7262
69	1.0159	0.7372	1.0094	0.7238
70	1.0315	0.7345	1.0253	0.7215
71	1.0468	0.7318	1.0409	0.7193
72	1.0618	0.7293	1.0561	0.7171
73	1.0764	0.7268	1.0711	0.7150
74	1.0908	0.7244	1.0857	0.7130
75	1.1048	0.7221	1.1000	0.7110
76	1.1185	0.7199	1.1139	0.7091
77	1.1320	0.7177	1.1276	0.7073
78	1.1451	0.7156	1.1410	0.7055
79	1.1579	0.7135	1.1541	0.7038
80	1.1704	0.7115	1.1668	0.7021
81	1.1827	0.7096	1.1793	0.7004
82	1.1946	0.7077	1.1915	0.6988
83	1.2063	0.7058	1.2034	0.6973
84	1.2177	0.7040	1.2151	0.6958
85	1.2289	0.7023	1.2265	0.6943
86	1.2398	0.7006	1.2376	0.6929
87	1.2504	0.6990	1.2484	0.6915

Frequency (GHz)	k_H	α_H	k_V	α_V
88	1.2607	0.6974	1.2590	0.6902
89	1.2708	0.6959	1.2694	0.6889
90	1.2807	0.6944	1.2795	0.6876
91	1.2903	0.6929	1.2893	0.6864
92	1.2997	0.6915	1.2989	0.6852
93	1.3089	0.6901	1.3083	0.6840
94	1.3179	0.6888	1.3175	0.6828
95	1.3266	0.6875	1.3265	0.6817
96	1.3351	0.6862	1.3352	0.6806
97	1.3434	0.6850	1.3437	0.6796
98	1.3515	0.6838	1.3520	0.6785
99	1.3594	0.6826	1.3601	0.6775
100	1.3671	0.6815	1.3680	0.6765
120	1.4866	0.6640	1.4911	0.6609
150	1.5823	0.6494	1.5896	0.6466
200	1.6378	0.6382	1.6443	0.6343
300	1.6286	0.6296	1.6286	0.6262
400	1.5860	0.6262	1.5820	0.6256
500	1.5418	0.6253	1.5366	0.6272
600	1.5013	0.6262	1.4967	0.6293
700	1.4654	0.6284	1.4622	0.6315
800	1.4335	0.6315	1.4321	0.6334
900	1.4050	0.6353	1.4056	0.6351
1 000	1.3795	0.6396	1.3822	0.6365

APPENDIX A-3

Disdrodata Program Structure Overview

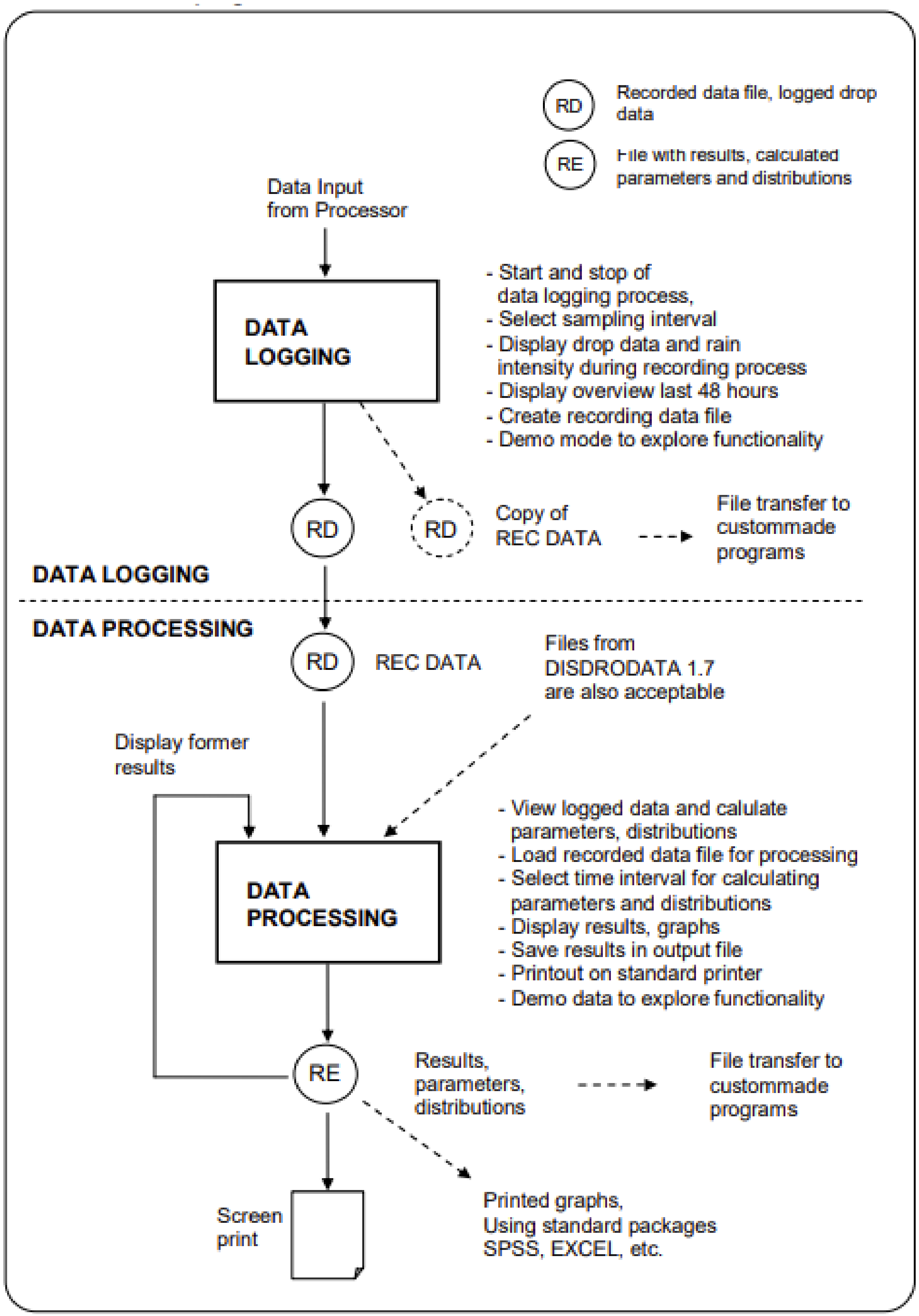

APPENDIX A-4

Table A-4: Subdivision of the 127 drop sizes measured by the disdrometer RD-80 into 20 drop size classes of the DISDRODATA program.

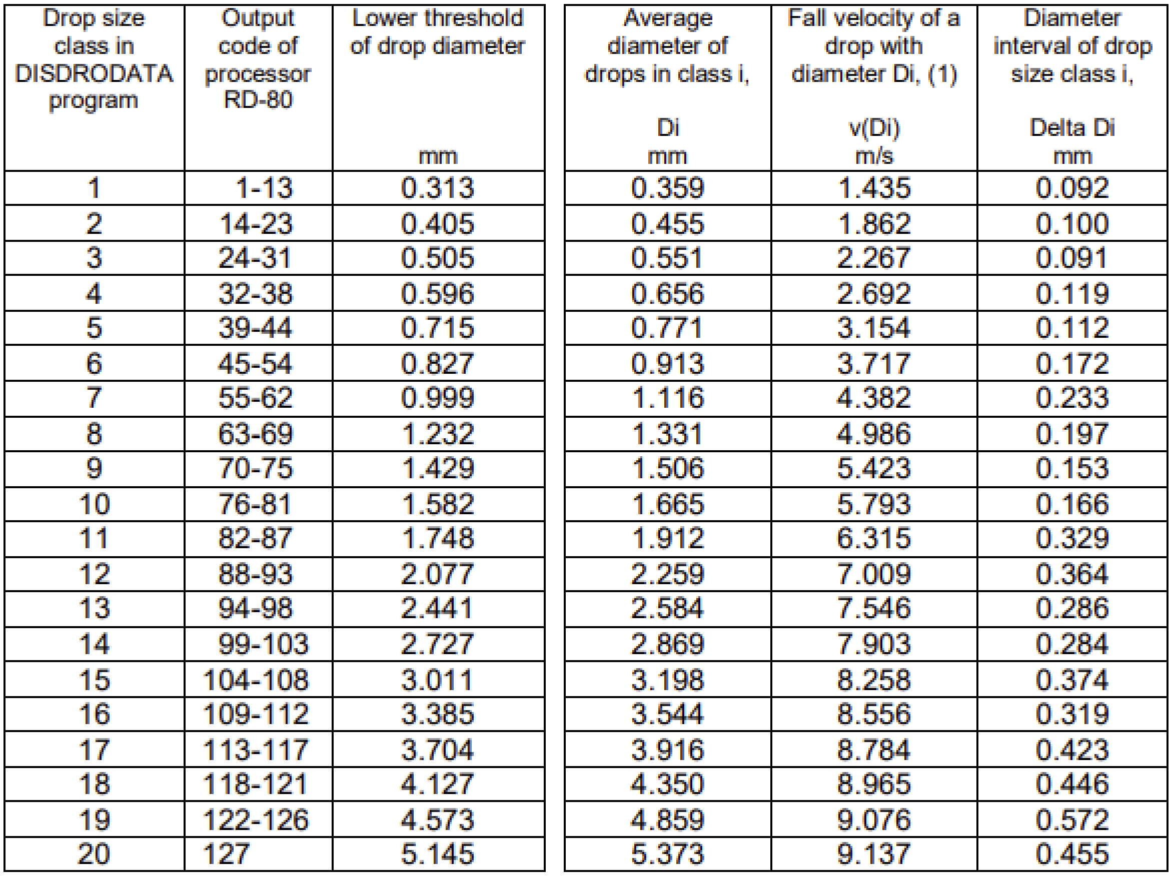

Drop size class in DISDRODATA program	Output code of processor RD-80	Lower threshold of drop diameter mm	Average diameter of drops in class i, Di mm	Fall velocity of a drop with diameter Di, (1) v(Di) m/s	Diameter interval of drop size class i, Delta Di mm
1	1-13	0.313	0.359	1.435	0.092
2	14-23	0.405	0.455	1.862	0.100
3	24-31	0.505	0.551	2.267	0.091
4	32-38	0.596	0.656	2.692	0.119
5	39-44	0.715	0.771	3.154	0.112
6	45-54	0.827	0.913	3.717	0.172
7	55-62	0.999	1.116	4.382	0.233
8	63-69	1.232	1.331	4.986	0.197
9	70-75	1.429	1.506	5.423	0.153
10	76-81	1.582	1.665	5.793	0.166
11	82-87	1.748	1.912	6.315	0.329
12	88-93	2.077	2.259	7.009	0.364
13	94-98	2.441	2.584	7.546	0.286
14	99-103	2.727	2.869	7.903	0.284
15	104-108	3.011	3.198	8.258	0.374
16	109-112	3.385	3.544	8.556	0.319
17	113-117	3.704	3.916	8.784	0.423
18	118-121	4.127	4.350	8.965	0.446
19	122-126	4.573	4.859	9.076	0.572
20	127	5.145	5.373	9.137	0.455

APPENDIX A-5

Input data for formulas

	Input data	**Dimensions**
n_i	Number of drops measured in drop size class i during time interval t	---
t	Time interval T1 for data logging, or Time interval T2 for calculations	s
F	Size of the sensitive surface of the sensor	m^2
D_i	Average diameter of drops in class i	mm
$v(D_i)$	Fall velocity of drop with diameter D_i	m/s
ΔD_i	Diameter interval of drop size class i	mm

APPENDIX A-6

Formulas

These parameters are calculated for each time interval.

	Parameters and formulas
RI	Rain intensity (= rainfall rate), [mm/h] $RI = \frac{\pi}{6} \cdot \frac{3.6}{10^3} \cdot \frac{1}{F \cdot t} \cdot \sum_{i=1}^{20} (n_i \cdot D_i^3)$
RA	Rain amount, [mm] $RA = RI \cdot t/3600$
RAT	Total rain amount since start of measurement, [mm] $RAT = \sum RA$